Non - Isothermal Film Blowing Process Stability Analysis for Non - Newtonian Fluids by using Variational Principles

Bc. Roman Kolařík

Master thesis
2008

Tomas Bata University in Zlín
Faculty of Technology

Univerzita Tomáše Bati ve Zlíně
Fakulta technologická
Ústav výrobního inženýrství
akademický rok: 2007/2008

ZADÁNÍ DIPLOMOVÉ PRÁCE

(PROJEKTU, UMĚLECKÉHO DÍLA, UMĚLECKÉHO VÝKONU)

Jméno a příjmení:	**Bc. Roman KOLAŘÍK**
Studijní program:	**N 3909 Procesní inženýrství**
Studijní obor:	**Konstrukce technologických zařízení**
Téma práce:	**Stabilitní analýza neizotermálního procesu vyfukování pro nenewtonské kapaliny s využitím variačního počtu**

Zásady pro vypracování:

1. Vypracujte literární studii na dané téma.
2. Proveďte teoretickou analýzu stability procesu vyfukování s využitím variačních principů pro nenewtonské polymerní taveniny a neizotermální zpracovatelské podmínky.
3. S využitím programovacího jazyka C++ sestavte vhodný algoritmus pro numerické řešení řídících rovnic procesu vyfukování.
4. Na základě odvozených stabilitních diagramů ohodnoťte vliv tokového chování nenewtonských polymerních tavenin, molekulární struktury polymerů a procesních podmínek na stabilitu procesu vyfukování.
5. Teoretické závěry ověřte s experimentálními daty.

Rozsah práce:

Rozsah příloh:

Forma zpracování diplomové práce: **tištěná/elektronická**

Seznam odborné literatury:

CANTOR, K. Blown Film Extrusion. Munich : Cark Hanser Verlag, 2006. 165 s. ISBN 1-56990-396-4.
BUTLER, T.I. Film extrusion Manual : Process, materials, properties. Atlanta : Tappi press, 2005. 616 s. ISBN 1-59510-075-X.
WALLER, P. What to do when the bubble won't behave. Plastic Technology, p. 36, 2002.
BUTLER, T.I. Blown film bubble instability induced by fabrication conditions. SPE ANTEC Tech. Papers 1, p. 1120, 2000.
ZATLOUKAL, M., VLCEK, J. Modeling of the film blowing process by using variational principles. Journal of Non-Newtonian Fluid Mechanics, 123(2-3), p. 201-213, 2004.
ZATLOUKAL, M., VLCEK, J. Application of variational principles in modeling of the film blowing process for high stalk bubbles. Journal of Non-Newtonian Fluid Mechanics 133(1), p. 63-72, 2006.
ZATLOUKAL, M., MAVRIDIS, H., VLCEK, J., SAHA, P. Modeling of Non-isothermal high stalk film blowing process by using variational principles for non-Newtonian Fluids. SPE ANTEC, Cincinnati, USA, 2007.
HAN, Ch.D. Rheology in Polymer Processing. New York : Academic Press, 1976. 366 s. ISBN 0-12-322450-0.
BAIRD, D.G., COLLIAS, D.I. Polymer Processing - Principles and Design. New York : Wiley, 1998.
KANAI, T., CAMPBELL, G.A. Film Processing. Munich : Hanser Publishers, 1999. 446 s. ISBN 3-446-17882-1.

Vedoucí diplomové práce: **prof. Ing. Martin Zatloukal, Ph.D.**
Centrum polymerních materiálů

Datum zadání diplomové práce: **19. února 2008**

Termín odevzdání diplomové práce: **23. května 2008**

Ve Zlíně dne 29. ledna 2008

doc. Ing. Petr Hlaváček, CSc.
děkan

L.S.

UNIVERZITA TOMÁŠE BATI VE ZLÍNĚ
Fakulta technologická

doc. Ing. Miroslav Maňas, CSc.
ředitel ústavu

ABSTRAKT

Tato práce se zabývá problematikou vzniku nestabilního rukávu při výrobě fólií vyfukováním, a to s cílem stanovit stabilitní diagramy hodnotící vliv procesních podmínek, designu vytlačovací hlavy a tokových charakteristik polymerů za předpokladu neizotermálních podmínek. Za tímto účelem byl použit model, který pohlíží na existenci stabilního procesu vyfukování jako na stav, který odpovídá minimálním energetickým nárokům. Teoretické závěry byly následně porovnány s odpovídajícími experimentálními daty pro lineární a různě rozvětvené polyolefiny a bylo zjištěno, že predikce použitého modelu jsou v dobré shodě s experimentální realitou pro různé procesní podmínky. Nejdůležitějším závěrem celé práce je zjištění, že vztah mezi stabilitou procesu vyfukování a větvením polymeru má nemonotónní charakter.

Klíčová slova: Vyfukování, vytlačování, polymer, modelování polymerních procesů, stabilitní analýza.

ABSTRACT

In this work, film blowing stability analysis has been performed theoretically by using minimum energy approach for non-Newtonian polymer melts considering non-isothermal processing conditions with the aim to understand the complicated link between processing conditions, machinery design and material properties. Specific attention has been paid to the investigation of the complicated links between polymer melt rheology (extensional strain hardening/thinning, shear thinning, flow activation energy, Newtonian viscosity, melt strength), processing conditions (heat transfer coefficient, mass flow rate, die exit temperature, cooling air temperature) and film blowing stability. It has been found that the theoretical conclusions are in very god agreement with the experimental reality supporting the validity of the used numerical approach and film blowing model. The most important conclusion from this work is theoretically and experimentally supported finding that dependence between long chain branching and bubble stability is non-monotonic.

Keywords: Blown film, extrusion, polymer, modeling of polymer processing, stability analysis.

ACKNOWLEDGEMENTS

Here, I would like to take the opportunity to say: “Thank you very much, all of you who helped me with my Master thesis.”

I would like to express my gratitude to prof. Ing. Martin Zatloukal, Ph.D. for his advice, support and patience all the time of the work on my thesis.

My acknowledgement also belongs to doc. Ing. Anežka Lengálová, Ph.D., who helped me significantly during the creation of my theoretical part.

And last but not least, I am indebted to my beloved family for their interest in my work, and all the friends, especially Jan Musil, for their support.

I agree that the results of my Master thesis can be used by my supervisor’s decision. I will be mentioned as a co-author in case of any publication.

I declare I worked on this Master thesis by myself and I have mentioned all the used literature.

Zlín, May 22, 2008 ….…….

Roman Kolařík

CONTENTS

INTRODUCTION

Although the tubular film blowing process belongs to the oldest polymer processing technologies, the process is still the most widely and frequently used technology to produce thin thermoplastic films, mostly polyethylene. The first commercial film blowing line was constructed in the late 1930´s in the USA and since then the technology has been developing continuously [1, 2].

Film blowing lines produce biaxially oriented films of small thickness, which are used in commodity applications. Thus, the film can be used in food processing industry, e.g. for carrier bags and food wrapping, in the waste industry such as garbage bags or waste land fill liners. Other applications are medical films or scientific balloons [1-3].

The film blowing process has been researched experimentally and theoretically during a long history. However, clear relationships between the machine design, processing parameters, material and stresses have not been fully explained yet. Moreover, the film blowing process is affected by the creation of the bubble instabilities at particular processing conditions, which is one of the limiting factors for the process. To understand these instabilities in more detail, modeling of the film blowing process is usually used.

For this purpose the Pearson and Petrie formulation [1], as a classical method, is usually employed. However, the use of the formulation leads to variety of the numerical instabilities [4] and the experimental reality is not described very well, mainly in the case of the bubble with neck [5]. These difficulties can be overcome by the utilization of recently proposed Zatloukal-Vlcek film blowing model [6-9] derived through variational principles which is capable to predict bubble shape (and corresponding processing conditions) which satisfies the minimum energy requirements. Recently, it has been demonstrated for isothermal conditions and Newtonian fluids that the stable film blowing process can be viewed as the state which, firstly, satisfies minimum requirements and secondly, does not yields the bubble machine and circumference stresses higher than the rupture stress [2].

In order to extend the knowledge about the film blowing instabilities, non-isothermal Zatloukal-Vlcek model for non-Newtonian polymer melts will be utilized to understand the effect of heat transfer coefficients, melt/air temperature, flow activation energy, MWD, shear thinning, extensional strain hardening/thinning on the film blowing stability. Special

attention will be paid to understand the complicated link between long chain branching and film blowing stability from both, theoretical and experimental point of view.

I. THEORETICAL BACKGROUND

1 THE FILM BLOWING PROCESS

The film blowing process is predominantly used for the production of thin biaxially-oriented thermoplastic films, especially from polyolefines on the film blowing line, which is described here in more detail.

1.1 Description of the film blowing line

The most often used film blowing line type consist of the nip rollers which are situated on the top of the line, as depicted in Fig. 1 [1,2, 10].

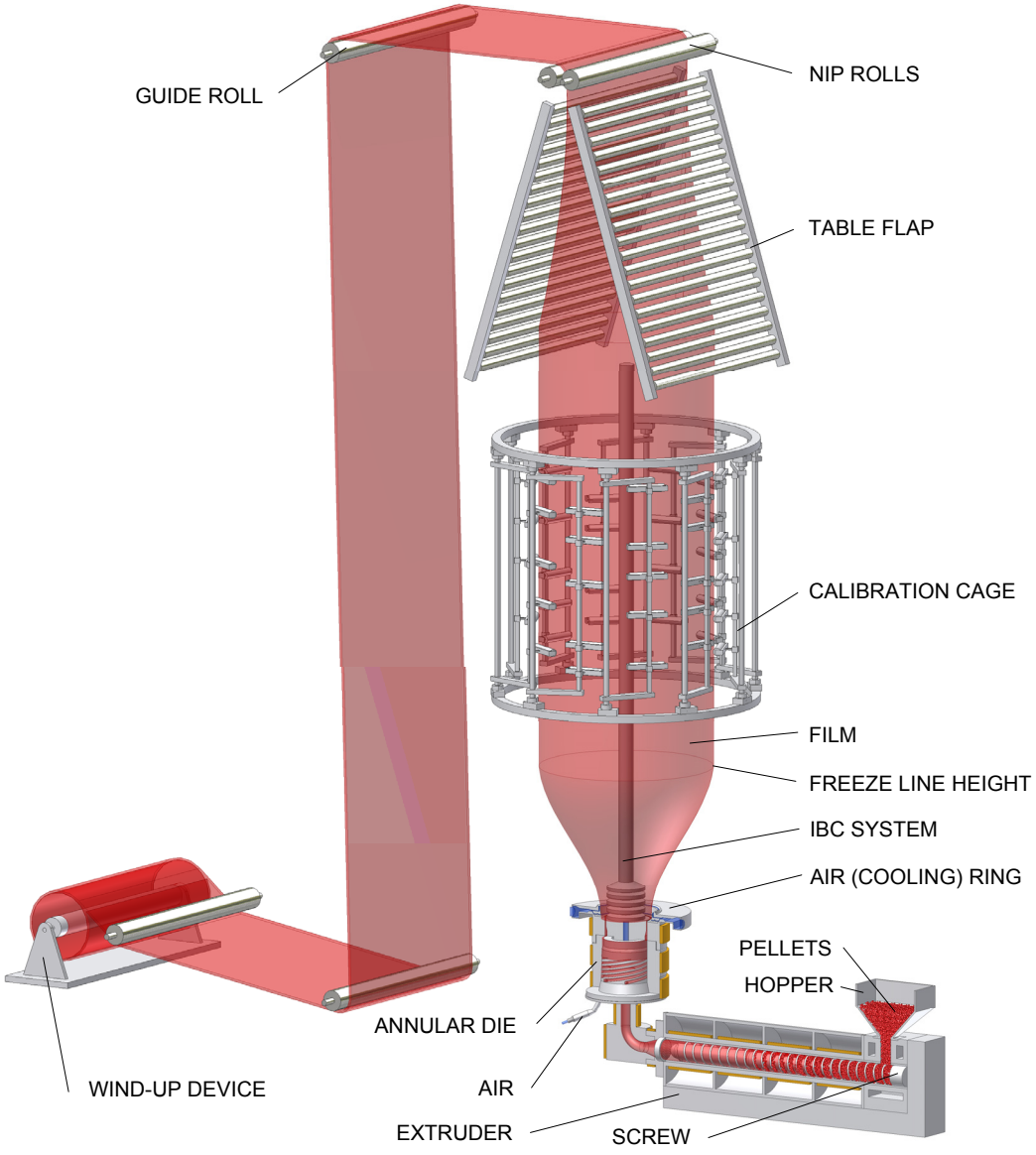

Fig. 1. Film blowing line

The film blowing process description is provided in the next section in more detail.

1.2 The process description

At the beginning of the film blowing process, when the film is first extruded, film cylindrical-tube is necessary to close. Thus, from the annular die, the tube end is capped and tied to a rope. Then, it is drawn upward towards the nip rollers. This action must be provided very carefully to prevent the tube from tearing. When the tube achieves the nip rollers, it is sealed by the pinching action of the rollers. Then, it is fluently moved towards to the wind up device. During the action, pressurized air is blown into the tube to inflate it into a bubble, as can be seen in Fig. 2 [11]. The amount of air and the nip roller speed are adjustable parameters which are important from the bubble stability point of view [11].

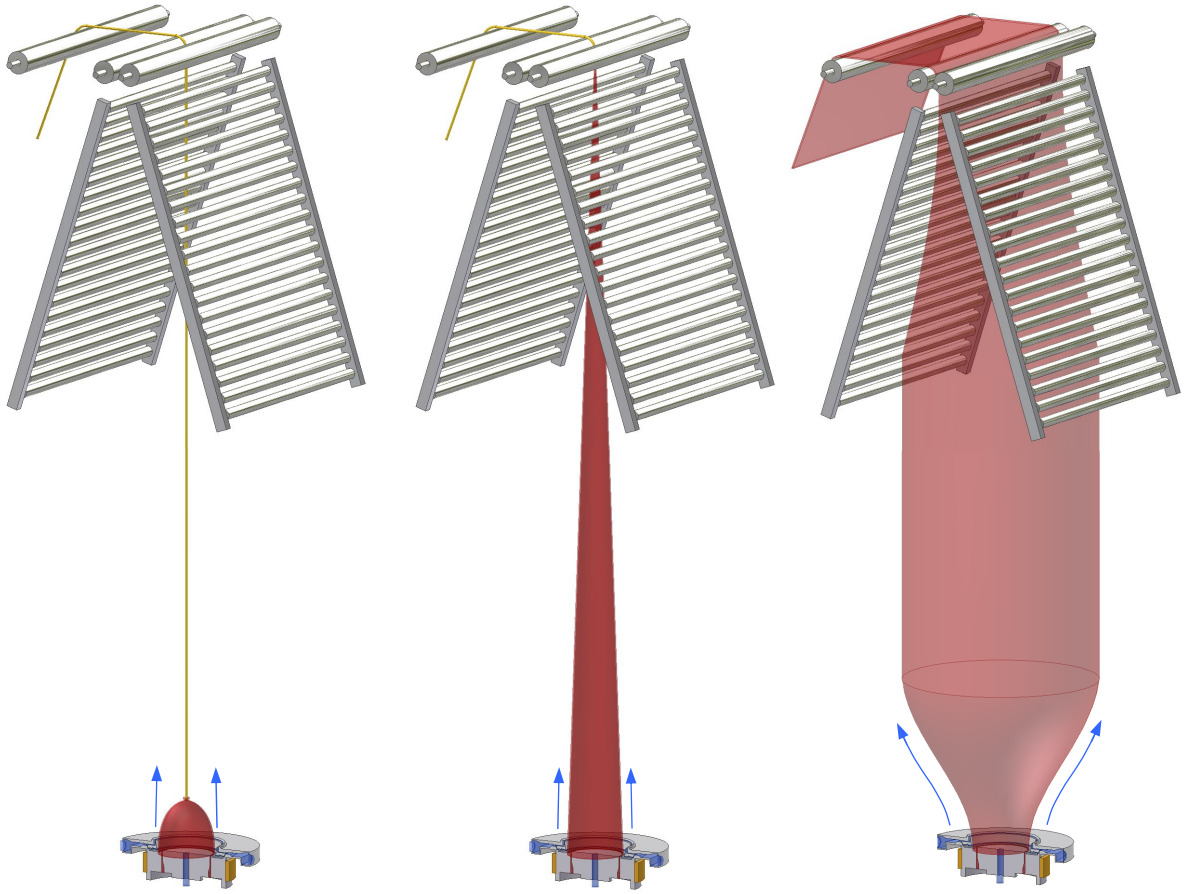

Fig. 2. Procedure used to start the film blowing process

The tubular film blowing process belongs to continual methods of the film production. In this regard, the chamber of the solid polymer pellets is set on the start of the film blowing line. Thus, continuous material feed to a hopper of the extruder is established

by a material handling system, such as silo and pneumatic loader. The hopper holds the solid material and is cooled for the following two reasons. First, the friction between the pellets is bigger if they are colder, i.e. more rigid. This ensures higher extruder output. Second, hopper cooling limits creation of the pellets dome, which can cause shut-down of the film blowing process. Then, pellets go through the hopper to the thread of the screw. There, with the help of the barrel, pellets are transported, homogenized, compressed and melted. The energy necessary for heating the pellets is obtained by dissipation and from the heating elements along the barrel. During the process the required constant temperature of every zone is kept by cooling fans along the barrel.

At the end of the barrel, the polymer pellets are molten and the melt is extruded through an annular die. Hence, the film is created to shape continuous cylinder by the internal air pressure. The cylinder moves in the vertical direction upwards. In the area between the annular die (die exit) and the freeze line the polymer is in a molten state. With the help of a cooling ring (with/without internal bubble cooling system IBC) the bubble is cooled to solid film. Air is uniformly blown along the bubble surface. A constant diameter of the created film bubble is kept by a calibration bubble cage. This cooling bubble is folded between two table flaps and then two nip rollers close it. In the next step control of film dimensions is performed, i.e. thickness and width of the layflat film is measured. Film thickness is determined by the nip roll speed and also by the internal air pressure. After the dimensions control the final film can be one-side or two-side split (see Appendix PI for more detailed process description). The product is thin film. In the other cases (when a cutting mechanism is not used), the final film can be used as a bag. Finally, the film is spooled on the cylinder of a wind-up device where it is cut on a required length by a radial cutting mechanism [3, 11-17].

The most frequently used polymers for the film blowing process are polyolefins, such as LDPE, LLDPE and HDPE. Sometimes, also other materials are used, for example ethylene copolymers, polypropylene copolymers, nylon, elastomers, nitriles or polycarbonate [11].

The film blowing process is characterized by the below stated important parameters and equations which describe bubble geometry during the process [3, 11, 13, 15]. The parameters influence the area between the die exit and nip rollers, as shown in Fig. 3 [13].

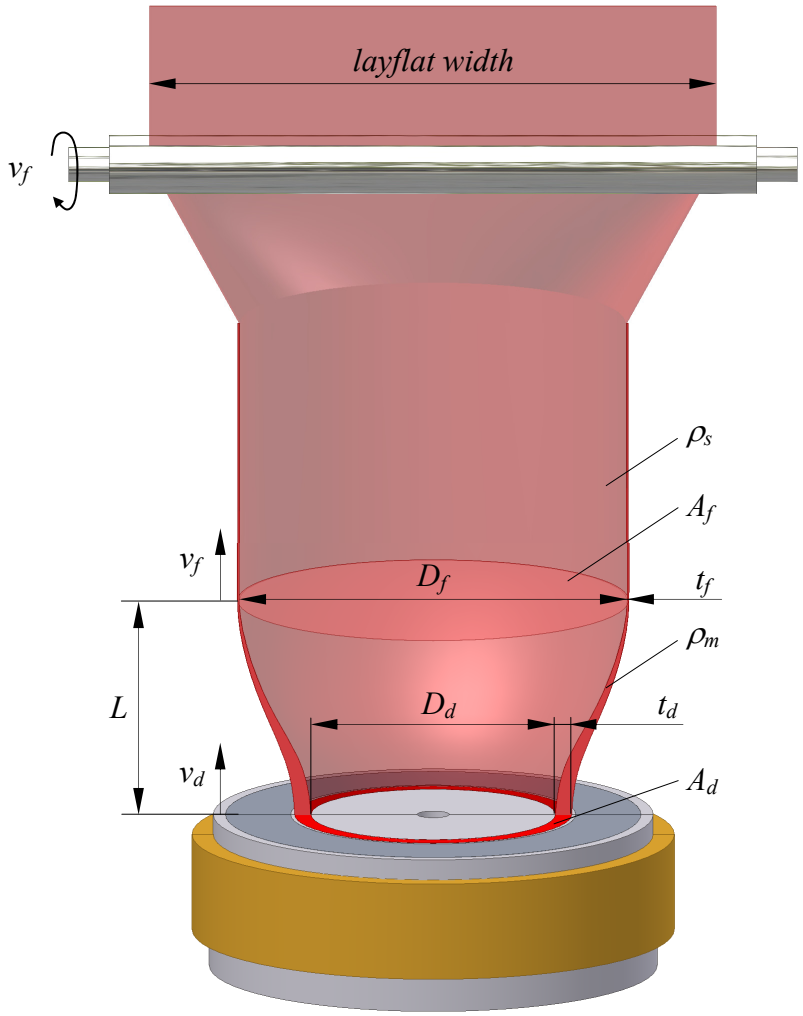

Fig. 3. Elements of blown film

The most important film blowing process parameters are described below in more detail.

Blow up ratio

Blow up ratio, *BUR*, shows the size of the melt stretching in the transverse direction. Blow-up ratio is expressed as the ratio of the final bubble diameter at the freeze line height, D_f, to the bubble diameter at the die exit, D_d, so it has the following form:

$$BUR = \frac{D_f}{D_d} \tag{1}$$

In the case when the line is running, the final bubble diameter is difficult to measure. Hence, the blow-up ratio is rewritten as

$$BUR = \frac{2 \cdot layflat\ width}{\pi D_d} \tag{2}$$

Die diameter is fixed and it is identified by the producer of the die. The most frequent blow-up ratio is in the range of 2 to 10.

Take-up ratio

The take-up ratio, *TUR*, is calculated as the ratio of the film velocity above the freeze line (nip velocity), v_f, to melt velocity through die exit, v_d. This is a parameter determining melt stretching in the machine direction. It can be written in the following form:

$$TUR = \frac{v_f}{v_d} \tag{3}$$

During the film blowing process, the melt velocity is difficult to measure. Then, it is possible to use the equation of conservation of mass with the condition that the mass flow rate is constant along the bubble. Thus, the take-up ratio is

$$TUR = \frac{\rho_m A_d}{\rho_s A_f} \tag{4}$$

where ρ_m is the polymer melt density, ρ_s means the solid polymer density, and A_d and A_f represent the die gap area and bubble cross-sectional area, respectively.

Draw-down ratio

Draw-down ratio, *DDR*, shows stretching in the machine direction. It is possible to express the total degree of film stretching because the thickness reduction occurs in the transverse and machine direction at the same time. *DDR* describes the thickness reduction from the die gap thickness, t_d, to the final film thickness, t_f.

$$DDR = \frac{t_d}{t_f BUR} \tag{5}$$

Draw-down ratio is more preferred than take-up ratio because it is easier to measure. The value of *DDR*, as well as *TUR*, is from 5 to 20.

Forming ratio

Forming ratio, *FR*, expresses the relation between the take-up ratio and the blow-up ratio. Thus, it gives a balance of process stretching.

$$FR = \frac{TUR}{BUR} \tag{6}$$

In the case when the forming ratio is equal to one, the mechanical properties in the machine and transverse directions are the same, i.e. the film is isotropic. *FR* is only used for general information about the molecular orientation and balance because the relationship between them is not precise.

The blow-up ratio together with the draw-down ratio describe two directions of the bubble extension in the area where the bubble is in a molten state. Thus, above the freeze line the biaxial orientation is insignificant. The film is oriented in the axial direction by the nip rollers with adjustable velocity. Then, this is one of the possibilities to change the film thickness. The second extension direction is circumferential, and is generated by the air pressure inside the bubble. So, the axial and circumferential extensions produce the final shape and thickness of the bubble. The bubble geometry is then affected by the change of the process conditions, as shown in Tab. 1 [3]. The table describes what will happen with the film thickness, bubble diameter and the freeze line height if one of the process variables increases. Here, the bigger and bold symbols represents a significant change in the bubble geometry during the increase of the given process parameter.

Tab. 1. The effect of major process variables on bubble geometry.

Variable to increase	Film thickness	Bubble diameter	Freeze line height
Nip speed	↓	↑	↑
Screw speed	↑	↑	↑
Cooling speed	↑	↓	↓
Bubble volume	↓	↑	↓

As can be seen, the bubble geometry is possible to vary only by the machine setting. This happens manually or automatically during the film blowing process.

If the nip speed increases, the film is getting thinner because the melt is stretched more in the machine direction. Although the thinner film is cooled faster, the freeze line height increases because the nip speed is more significant than cooling. In the area below the freeze line the bubble diameter and bubble volume are small. If the freeze line height increases, the volume increases. As the air volume inside the bubble is the same, the bubble diameter has to grow up.

In the case of the screw speed increase all the presented bubble geometry characteristics go up. Film thickness increases because the effect of the greater output is prevailing over the slight thinning effect from an increase in bubble diameter. The amount of the melt is greater, which also means more heat and longer time needed to cool the bubble. Then, the freeze line is higher and the bubble diameter is larger.

When the bubble is intensively cooled, the freeze line height decreases. Consequently, the bubble diameter decreases too because the area between the nip rollers and the freeze line is greater and the amount of air inside the bubble is constant. In such a case, when the bubble diameter is lower, the film thickness increases because in the transverse direction the film is not stretched so much.

Expansion of the bubble volume is affected by more air inside the bubble. Then, bubble diameter increases due to larger stretching in the transverse direction. On this account, the final film is thinner, the bubble is cooled faster and the freeze line is lower.

For a fluent film blowing process, the above presented interrelationships [3] are done for the stability of the process. In the case when measures are not effective, the bubble instabilities are created, as can be seen in the following part.

1.3 Bubble instabilities

One type of instabilities which can occur during the film blowing process is caused by wrong die design; among these are sharkskin, fish eye or port lines. Another sort of instabilities is called “thickness variation”. Here, the shape of the bubble is changing with time. It is created in the area between the die exit and freeze line. Bubble instability occurs when the film-production velocity is higher than a critical velocity of the film blowing process. It can cause: reduction of the film production-rate, worse-quality product

(mechanical and optical properties), formation of failures and large amounts of film scrap. It can even lead to interruption of the process [3].

More information about bubble instabilities can be found in studies [2, 10, 18-24]. During this research the following conditions supporting more stable bubble were stated:

- lower melt temperature (researched in detail by Han [19, 20])
- broad molecular weight distribution and long chain branching (details in Kanai and White [22])
- LLDPE mixed with blends of LDPE (further developed by Obijeski [21]).

The film blowing process is significantly affected by the thickness variation instabilities. Thickness variation can be of seven types: draw resonance, helical instability, instability of the freeze line height, heavy-bubble instability, bubble flutter, bubble breathing and bubble tear [2, 3, 18, 25].

1.3.1 Draw resonance

Draw resonance is also called “periodic diameter oscillation” or “hourglassing”, and can be seen in Fig. 4 [2]. Draw resonance occurs when the draw-down ratio achieves a critical value. Thus, especially strain hardening causes the instability in the area of high strain rates (i.e. high take-up ratio). Draw resonance also occurs due to high strain rates in the case of linear polymers where strain hardening does not exist. In this type of instability, film width is changed (increases and consequently decreases) at 2 to 10-second intervals by the internal bubble air. It can also happen if the bubble is perforated or air ring is not properly adjusted.

This instability can be eliminated by increasing the freeze line height, which can be controlled by increasing extruder output, higher screw velocity (reduction of the take-up ratio) and nip rolls speed, or by slower bubble cooling (i.e. modification of the air ring). Other solutions include increasing melt temperature or using polymer with higher Melt Index (MI) without strain hardening. Last but not least, stabilization can be done through narrowing the die gap and take-up ratio reduction.

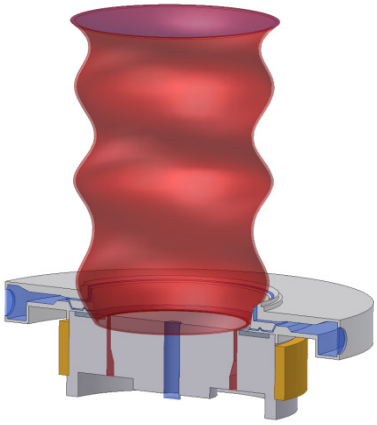

Fig. 4. Draw resonance

1.3.2 Helical instability

Helical instability, or "snaking", occurs when the configuration of air ring is unsuitable. It means, the freeze line is too low. As can be seen in Fig. 5 [2], the right side of the bubble is cooled more than the left side, which causes helical instability. Another reason for instability creation is air rotation inside the air ring. Then, the bubble undulants at intervals of 5 up to 10 seconds.

Increasing of the freeze line height is the most common stabilization way. This type of instability can be stabilized in the same way as in the case of draw resonance, i.e. by increasing extruder output or by the modification of the air ring to provide constant airflow on the bubble surface. Further, it is also possible to eliminate the instability by reduction of the melt temperature, polymer change to a lower-MI material, or, if possible, to use a wider die gap for better protection against turbulence inside the air ring.

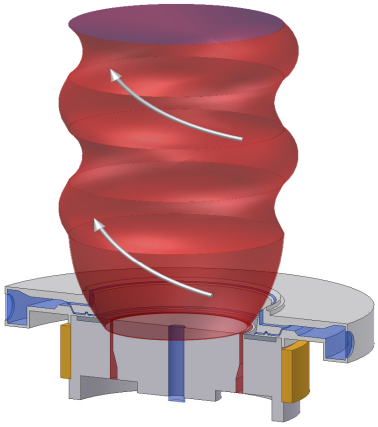

Fig. 5. Helical instability

1.3.3 Instability of the freeze line height (FLH instability)

Another type of instability presents as changing the freeze line height, that is why it is also called “periodic oscillation of the freeze line height”. The oscillations appear in 30-second to 5-minute intervals. This can be caused by surging, flow of surrounding air, or relatively slow changes in ambient temperature. Oscillations are in the range of several centimeters. For the long oscillation times the bubble seems to be stable at first sight (Fig. 6) [2]. However, in more detail, in the area of freeze line there is a little thickness variation in the machine direction. It is caused by high internal pressure in the bubble or changes of the bubble temperature.

As presented above, surging is one of the reasons of the instability creation. Surging is the result of extruder motor amps and back pressure - the freeze line height rises and falls. The problem can be solved by lowering the temperature of the extruder feed and second barrel zones (better feeding and melting). In this context, it is important to avoid blending polymers with very different melt flow indexes that do not mix well. Then, an appropriate air ring, haul off speed or unworn screws are necessary for good mixing. Thus, especially when the freeze line height changes during the film blowing process and it cannot be eliminated, the bubble is shielded by e.g. a bubble calibration cage.

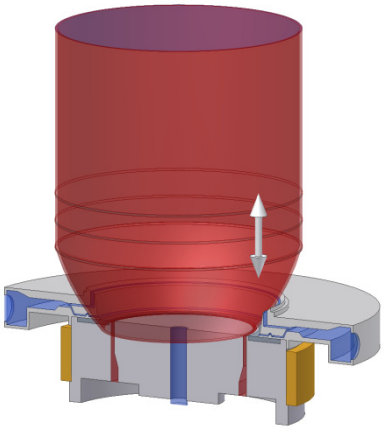

Fig. 6. FLH instability

1.3.4 Heavy-bubble instability

Poor cooling of the bubble creates instability that is called “bubble sag” or “sleeping bubble” and also “heavy bubble”. In such a case, the bubble can touch the air ring, as shown in Fig. 7 [2]. This happens when the force of the cooling air is higher than the tensile strength of the processed material. Then, bubble diameter is bigger than it should be

and consequently, the layflat width of the final film is wider too. As in other bubble instabilities, this type is created in the area where the polymer is in a molten state. It means that during the contact with the air ring flow marks or wrinkles appear on the film surface.

To the prevention the creation of this instability, the extruder output should be decreased (lower screw and nip speeds), the same as melt temperature, the chosen material should has a lower-MI and greater melt strength, or narrower die gap should be used for better cooling.

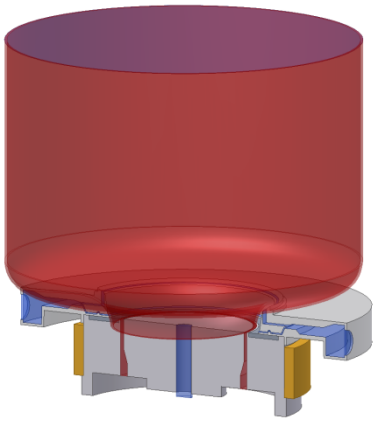

Fig. 7. Bubble sag

1.3.5 Bubble flutter

Bubble flutter instability generally occurs below the freeze line. In transverse direction it evokes “chatter marks” on the film in the molten state. The reason for the instability is a high velocity of cooling air impinging on the bubble surface. Then the bubble surface flutters in the area between the die and the freeze line, as shown in Fig. 8 [2]. If the deformation is intensive, it causes the thickness variation in the molten state. This bubble instability can be limited by reducing the output rate from the die. Another possible remedy is, to lower melt temperature, or use higher-MI resin; also a narrower die gap can contribute to better bubble cooling.

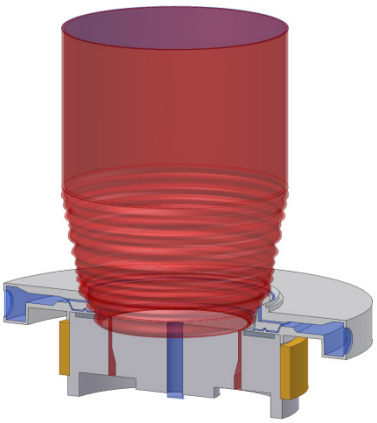

Fig. 8. Bubble flutter

1.3.6 Bubble breathing

When the internal cooling air changes the bubble volume, the bubble increases and decreases periodically – the bubble "breathes" (Fig. 9) [3]. In this case, there are fluctuations in layflat width and machine direction film thickness. The breathing cycles can be shorter or longer, which depends on the amount of variation or speed of the cycle. This problem can be solved by reducing melt temperature, using higher-MI resin or decreasing extruder output. The machinery can be controlled by internal bubble cooling valves, blowers and sensors. Thus, the internal bubble cooling system plays a very important role from process stability point of view.

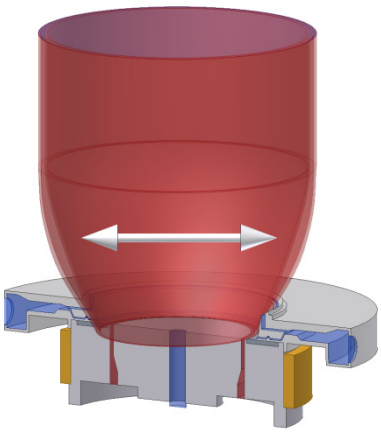

Fig. 9. Bubble breathing

1.3.7 Bubble tear

The "snap off", which is another term for the bubble tear instability, is created when the tensile stress at the film blowing exceeds the material strength. It means that the

take-off force, *F*, needed to draw up the bubble is higher than the tensile strength of the molten film. In such a case, the created bubble is torn in the direction of the acting force (machine direction) and the bubble tears off from the die exit (Fig. 10) [2]. This happens in high-molecular-weight polymers that experience high degree of strain hardening at high draw-down rates. To eliminate the problem, the cooling rate has to be reduced by suitable adjustment of the air ring. Other solutions are in reduction of extruder output, increase of the die and melt temperature, using a polymer with a higher melt index (without strain hardening) or by a narrower die gap, which should reduce the draw-down rate.

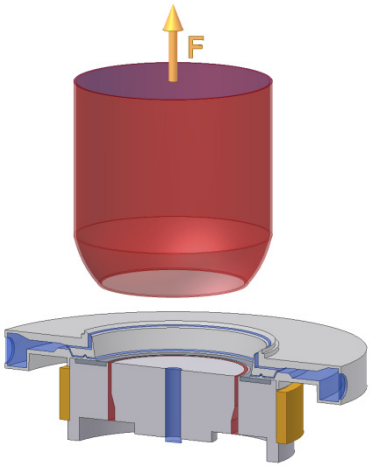

Fig. 10. Bubble tear

The above presented bubble instabilities include various problems: from variation of film thickness and width to scratches and tears. In the process with bubble instabilities it is very difficult to predict the exit velocity of an individual polymer. Stability of the film blowing process is influenced by the properties and structure of the polymer, process variables and design of the air ring [2, 23, 26]. Particularly the design of the air ring is very important for the determination of maximum exit velocity, i.e. for the definition of bubble instability. Therefore the study of the bubble stabilization is crucial.

1.3.8 The area of stable and unstable bubbles

The correct setting of the film blowing process parameters decides about the bubble instabilities. The below presented set of graphs, experimentally determined in [27], can be a useful tool for a technologist with respect to better determination of film blowing stability region. The graphs show the influence of the mass flow rate, melt temperature and heat transfer coefficient on the bubble stability under constant other processing conditions.

The effect of mass flow rate (keeping the melt equal to $185^{o}C$) on the film blowing stability is provided in Fig. 11. It is clearly visible that the mass flow rate increase leads to narrowing of the processing window. Interestingly, this experimental work suggests that at higher flow rates, the bubble is stable only for $BUR > 1$ even if the maximum cooling rate is applied.

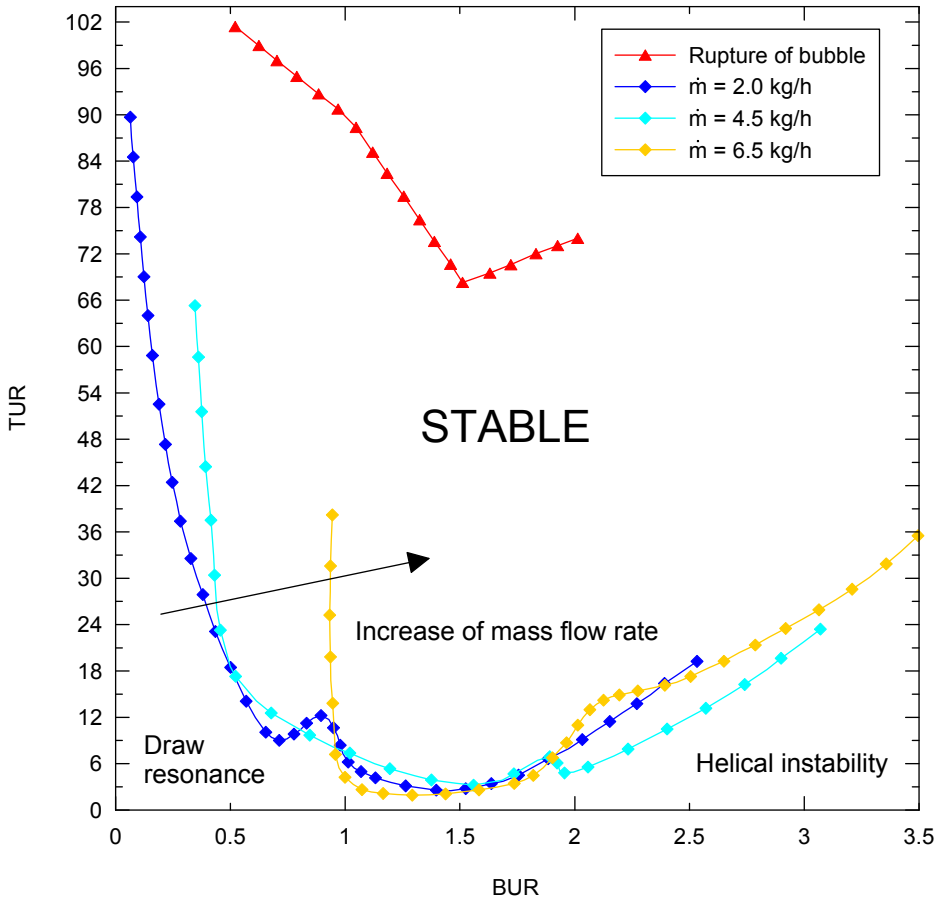

Fig. 11. Effect of mass flow rate on the film blowing stability (LDPE material, FLH = 250mm, T_{melt} = 185°C) [27]. Note that unstable area occurs below the stability contours.

The effect of air cooling efficiency (heat transfer coefficient) on the film blowing stability based on [27] is depicted in Fig. 12. It is nicely visible that a more efficient cooling strongly stabilizes the bubble.

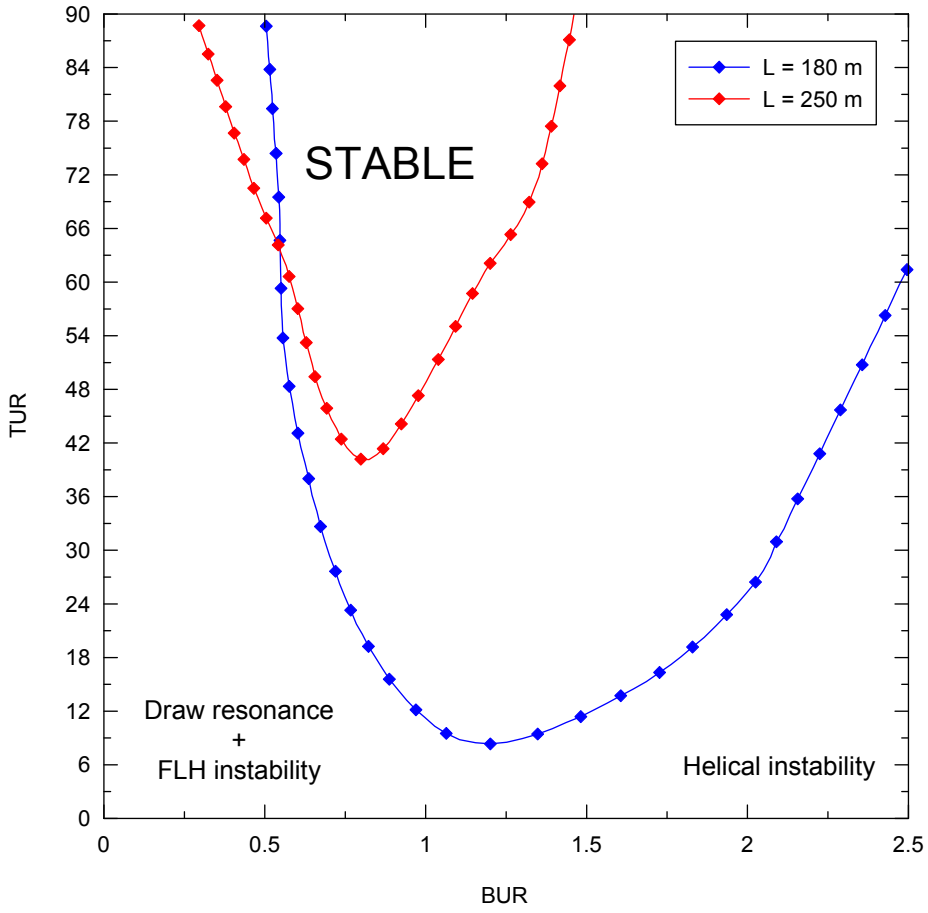

Fig. 12. The effect of FLH on the film blowing stability (LLDPE material, mass flow rate is 2kg/h, T_{melt} = 187°C) [27]. Note that unstable area occurs below the stability contours and vice versa.

Finally, the effect of melt temperature on the film blowing instability is depicted in Fig. 13. Clearly, the melt temperature increase leads to decrease in the film blowing stability and vice versa, which is also in agreement with the observations of Han et al. [28, 29].

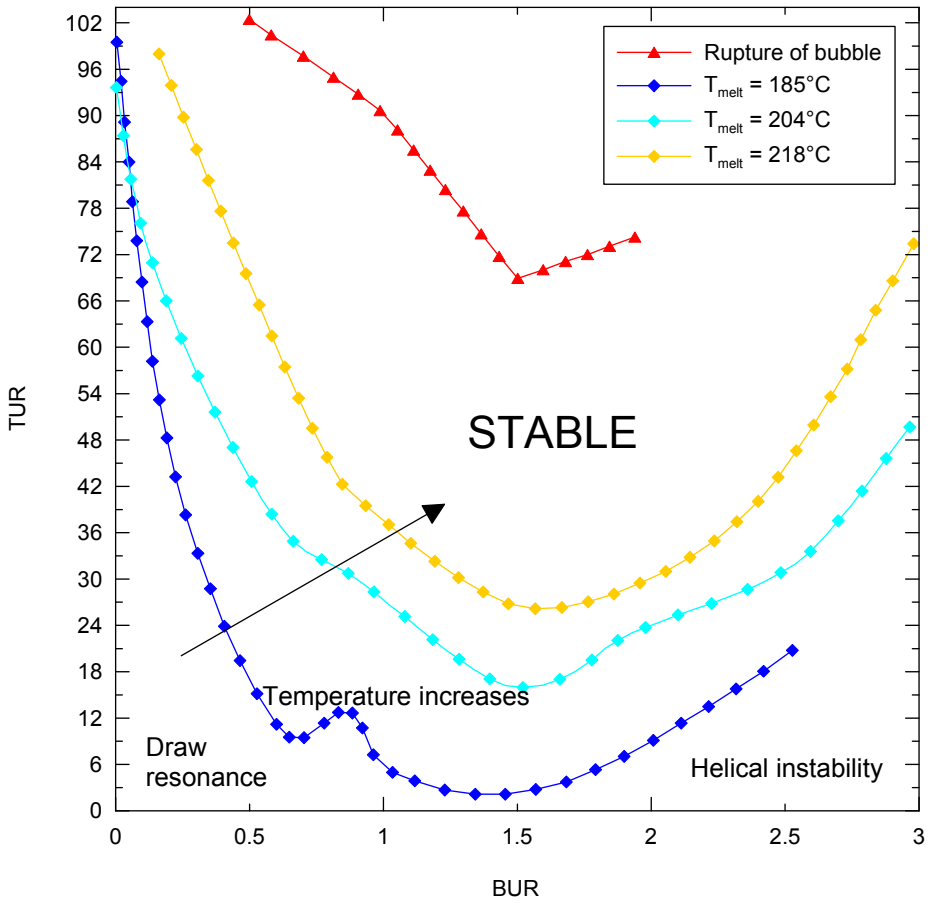

Fig. 13. Effect of melt temperature on the film blowing instability (LLDPE material, FLH = 250mm, mass flow rate = 2kg/h) [27]. Note that unstable area occurs below the stability contours.

The above presented graphs clearly demonstrates that the processing conditions, mainly mass flow rate, melt temperature and heat transfer coefficients plays an important role in the film blowing stability. These experimentally determined data will be followed by the non-isothermal Zatloukal-Vlcek model to evaluate its predictive power.

2 STABILIZATION OF THE FILM BLOWING PROCESS

During the film blowing process the bubble stability is influenced first of all by cooling of the bubble. For this purpose, an air ring or internal bubble cooling (IBC) system can be used. The bubble stability is also affected by the mechanical parts, such as iris, bubble guides and bubble calibration cage. The stabilization methods are presented below in more detail.

2.1 Bubble stabilization by cooling system (melt area)

The air cooling system (Fig. 14) [30] is a very important part of the film blowing line. It can be arranged both inside and outside of the bubble, or only outside. Internal bubble cooling is done with the help of an exhaust pipe. The outside bubble cooling is affected by an air ring. These types of cooling are used for the following reasons: First, cooling of the creating bubble is provided to heat removal from the molten polymer film. Generally, polyethylene has a higher specific heat than other polymers. Then, the material needs longer distance to cool. Second, it affects the stability of the film blowing process. Third, bubble cooling has an influence on the bubble forming. Last but not least, bubble cooling has a fundamental importance for the polymer mass throughput and final film properties. If the cooling system is not used during the process, the film blowing process will not work well. [3, 30-32]

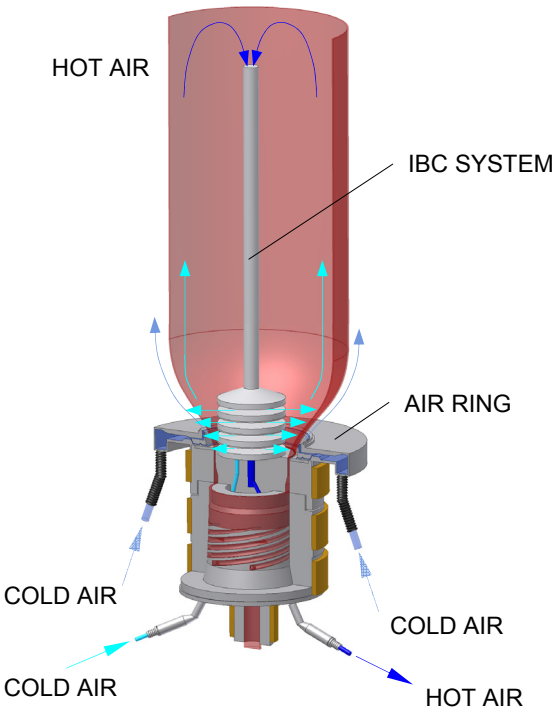

Fig. 14. Cooling system

During the bubble cooling, air stream properties are very important for the cooling effectivity. First, air speed determines the rate of heat removal from the film. The higher the air speed, the faster the film cooling. However, too fast stream of air causes bubble instability and the final film has poor properties. Second, air temperature has an influence on cooling speed. The colder air, the faster the film blowing process can be. On the other hand, if the cooling air should have a low temperature, the film processing will be too expensive. In such a case it is necessary to use insulation on the air hoses and air rings due to moisture condensation. Air temperature around the film blowing line is also very important. It must be taken into account because the freeze line height changes during the day and night. In this case, there is a requirement of air condition with the constant air temperature. Another aspect is air humidity, which affects the cooling effect; higher humidity leads to better cooling effect and vice versa [3, 31]. However, this opinion is not uniform, so further research is needed in this area.

As written above, bubble cooling can be realized by an air ring with/without internal bubble cooling system. This will be described in more detail [3, 31].

2.1.1 External cooling system – air ring

In this system the cooling part of the film blowing line is set on the top of the die, rather than on the insulating board, which presents insulation between the cool air ring and hot die. Cooling air is transported by the air ring directly onto the outer bubble surface. The air is blown through a number of hoses that are connected to the air ring around its circumference. Then, inside the ring, air flows into a series of baffles. Thus, air flow is balanced and ready for cooling of the creating bubble by flowing directly onto the outside of the bubble.

During the film blowing process, constant temperature of the surrounding air is very important as well as the temperature inside the die. For this purpose an insulating board is used to separate the two different environments. In an opposite case the film production efficiency will decrease.

In the film blowing process, it is possible to use two main types of the air ring. These are single and dual lips. The lip type is chosen first of all according to the bubble shape.

The single lip system, presented below in Fig. 15 [3], is used in the case of a stable bubble, for low-density polyethylene LDPE (low freeze line) or high-density polyethylene, HDPE (high freeze line). Thus, the single lip system is applicable first of all in the case of the higher freeze line and for high-melt-strength materials [3, 13, 30].

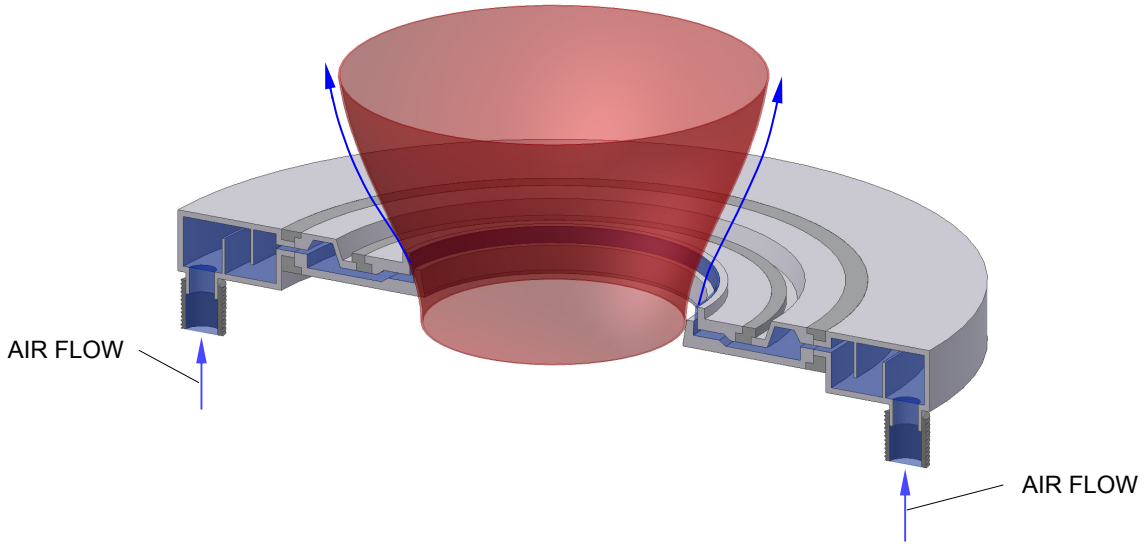

Fig. 15. Single lip design

A more expensive air ring type is the dual lip system. The basic design of the dual lip air ring is in the form of primary and secondary orifices which are separated by forming cone, as can be seen in Fig. 16 [3]. This cone sets the air flow, bubble shape and volume ratio in the two orifices. The primary orifice is lower and provides a small volume of air to the die exit with the view of increased melt strength and, also to prevent the bubble from touching the cone. Then, the bubble goes around the second orifice, which provides large volume of air to make solid film bubble. Thus, the length and shape of the cone determine the second orifice diameter.

The dual lip system is applied for the materials which tend to produce bubble instabilities, such as linear low-density polyethylene, LLDPE. This system provides not only cooling of the bubble, but also aerodynamical stabilization and film dimensional accuracy and is mainly used for low-melt-strength materials with lower freeze line height. [3, 18, 30].

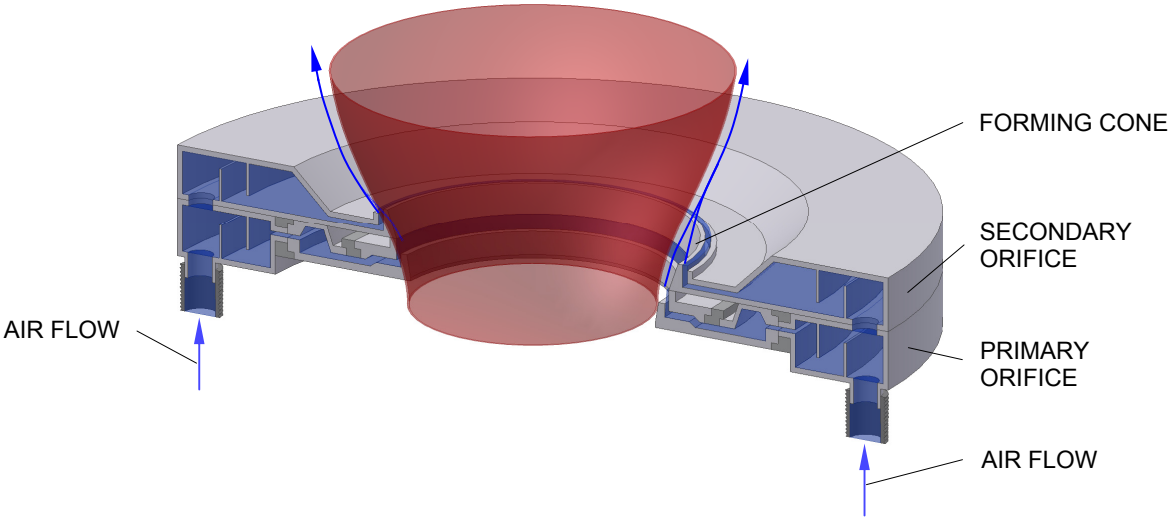

Fig. 16. Dual lip design

2.1.2 Internal bubble cooling system

In the case of a large film blowing line or higher line speed, an internal bubble cooling (IBC) system is used together with an air ring. This combination ensures better cooling; thus, better bubble stability and higher extrusion rates can be reached, namely 20% (small bubbles, below 203*mm* in diameter) to 80% (large bubbles) compared to other combinations of cooling [30]. The cooling system delivers cool air into the bubble and at the same time it removes heat from the inside of the bubble. As can be seen in Fig. 17 [30], the cool air is forced to pass through a stack of distributor disks where it is redirected and forced to impact normally to the internal bubble surface. Here, the heated air moves upwards and finally is redirected in the exhaust pipe. With the help of internal bubble cooling system there is a possibility to change the bubble diameter by the airflow rate adjustment. The shapes of internal bubble cooling systems are designed by various machinery manufactures on different ways. For better bubble cooling there is a possibility to chill the external air before it is blown inside the bubble [3, 13, 30].

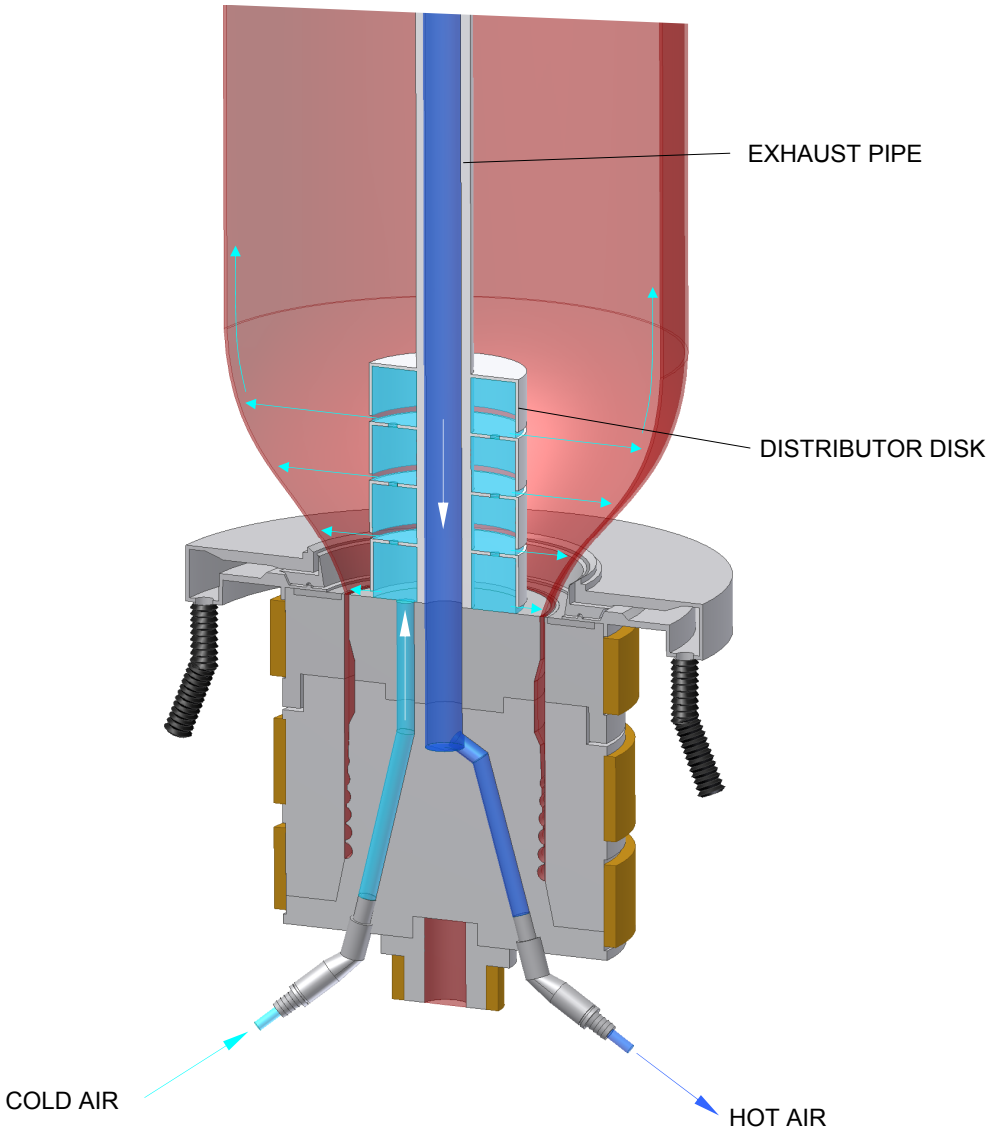

Fig. 17. IBC system

2.1.3 Venturi and Coanda effects

During external cooling of the bubble two important aerodynamic phenomena are observed - Venturi and Coanda effects. The Venturi effect occurs when air flows through narrow area where its speed increases and the pressure drops, as can be seen in Fig. 18 [33]. Then, a large vacuum is created near the air ring wall and the melt tube is drawn onto this wall. So it cools and stabilizes the bubble under the freeze line height and also enables increased output.

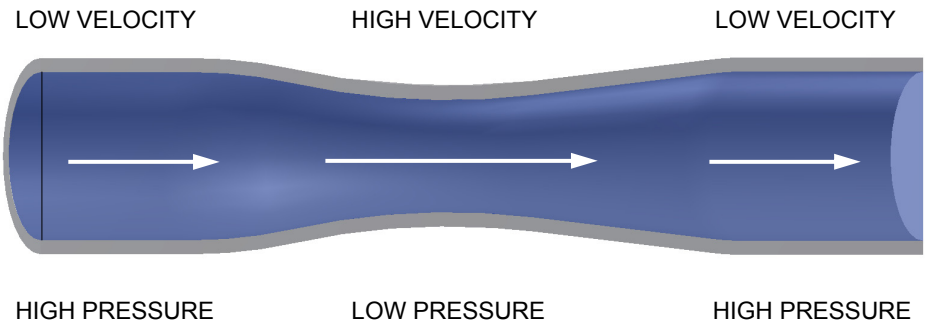

Fig. 18. Venturi effect

Less known is the Coanda effect (tendency of a air jet to stay attached to an adjacent curved surface), which is created in increased flow rates, as can be seen in Fig. 19 [33], where on the left side the medium cooling air flow rate is high (12*l/s*). On the other side the flow rate is only about 5*l/s*, it means the Coanda effect is not present here. Thus, it occurs when the air jet exiting from the upper lip suddenly turns towards the stabilization cone of the air ring, namely in the closed area [3, 31, 33].

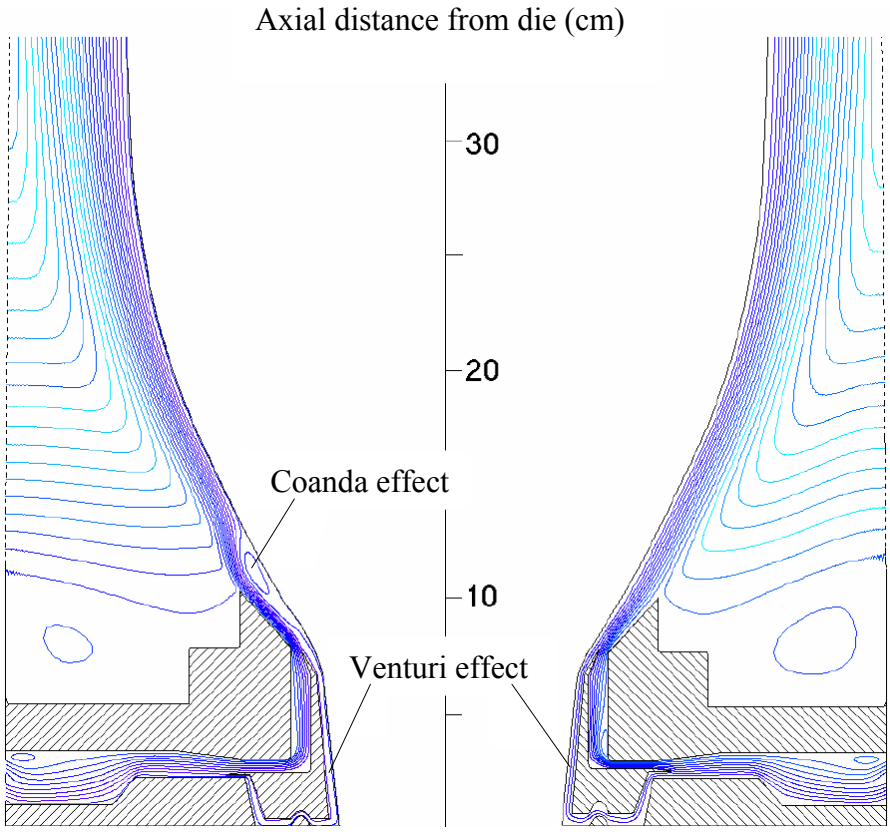

Fig. 19. Venturi and Coanda effects

Due to the fact that both phenomena may have significant effect on the air flow character/heat transfer coefficient, they also should be taken into account when film blowing stability analysis is performed.

2.2 Bubble stabilization by mechanical parts (solid area)

In the film blowing process the solid bubble (i.e. above the freezeline) is usually stabilized by external devices such, as irises, bubble guides and bubble calibration cages. The stabilization of the solid bubble is necessary because the bubble is sensitive to side movements from environmental effects, for example draft. This movement, called "dancing" is the cause of disunited wall thickness and it occurs in the case of bubbles with a small diameter and large height. With the use of bubble stabilization the film can be scratched. It happens when the below presented devices do not work properly [3, 13].

2.2.1 Iris

This stabilization device is set above the air ring, as presented in Fig. 20 [13]. The construction is very simple and it is very effective. The iris function consists in the change of the iris diameter according to the blow up ratio. Iris enables to hold the cooling air on the bubble surface in the area between the die exit and iris. Then the bubble cooling is more intensive. The problem about using of the iris is in the creation of the bubble rattling, which is affected by the cooling air volume [3, 13].

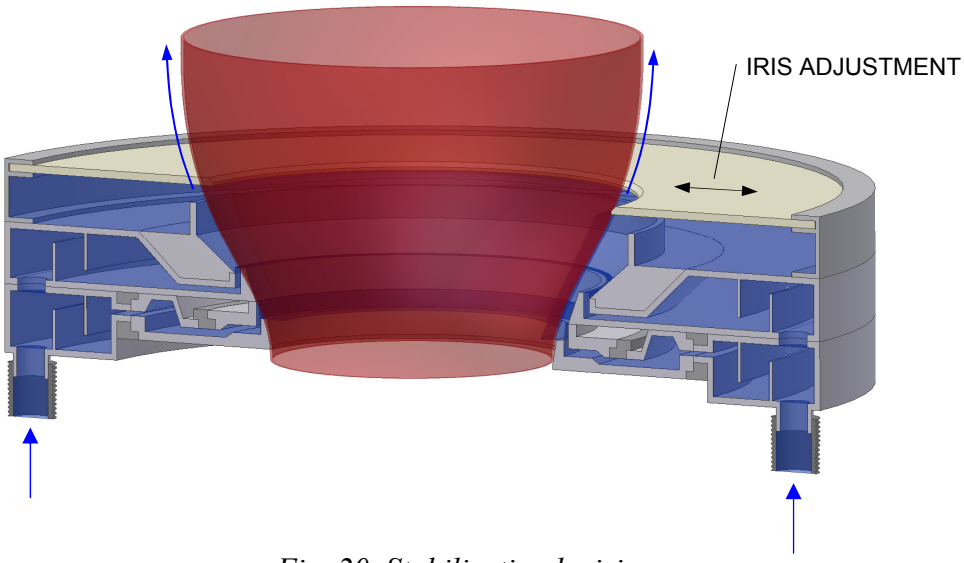

Fig. 20. Stabilization by iris

2.2.2 Bubble guides

Bubble guides are required between the freeze line and table flap to support and guide solid bubbles in processes with a higher output. Setting of the guides position has to guarantee concentricity of the bubble to the die. There are two modifications of the bubble guides (which are usually made from teflon). The first (Fig. 21) [13] is in the form of four bars which are closed with spur gears. They move towards the bubble with the help of the chain sheave until they touch it. Rotation around its axis is not allowed [13, 30].

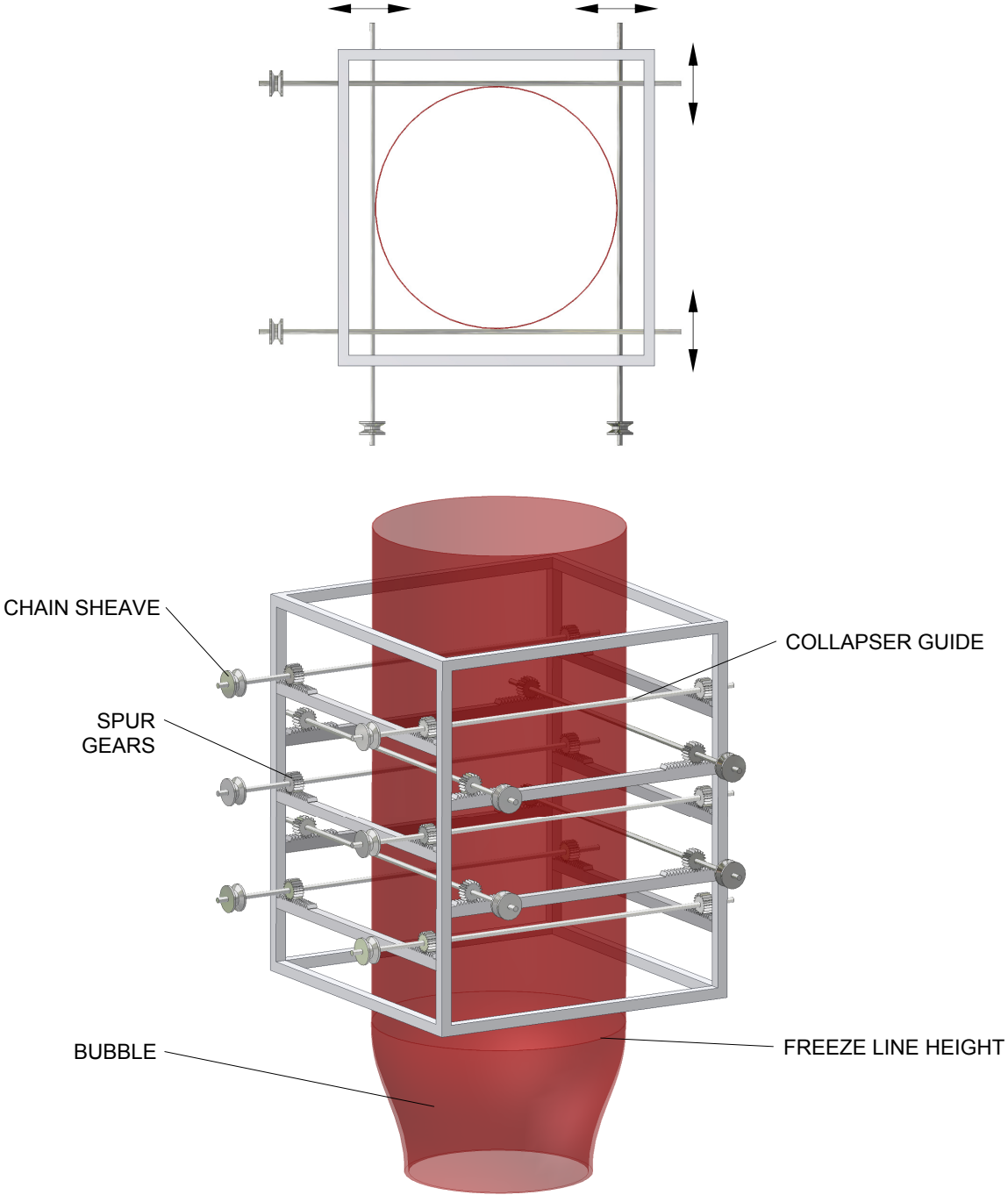

Fig. 21. Bubble guides – type A

The other type (Fig. 22) [13] has a better construction. There are four cylindrical arms, each of which can be adjusted. Then, they are in a good contact with the bubble surface and rotation around its axis is allowed.

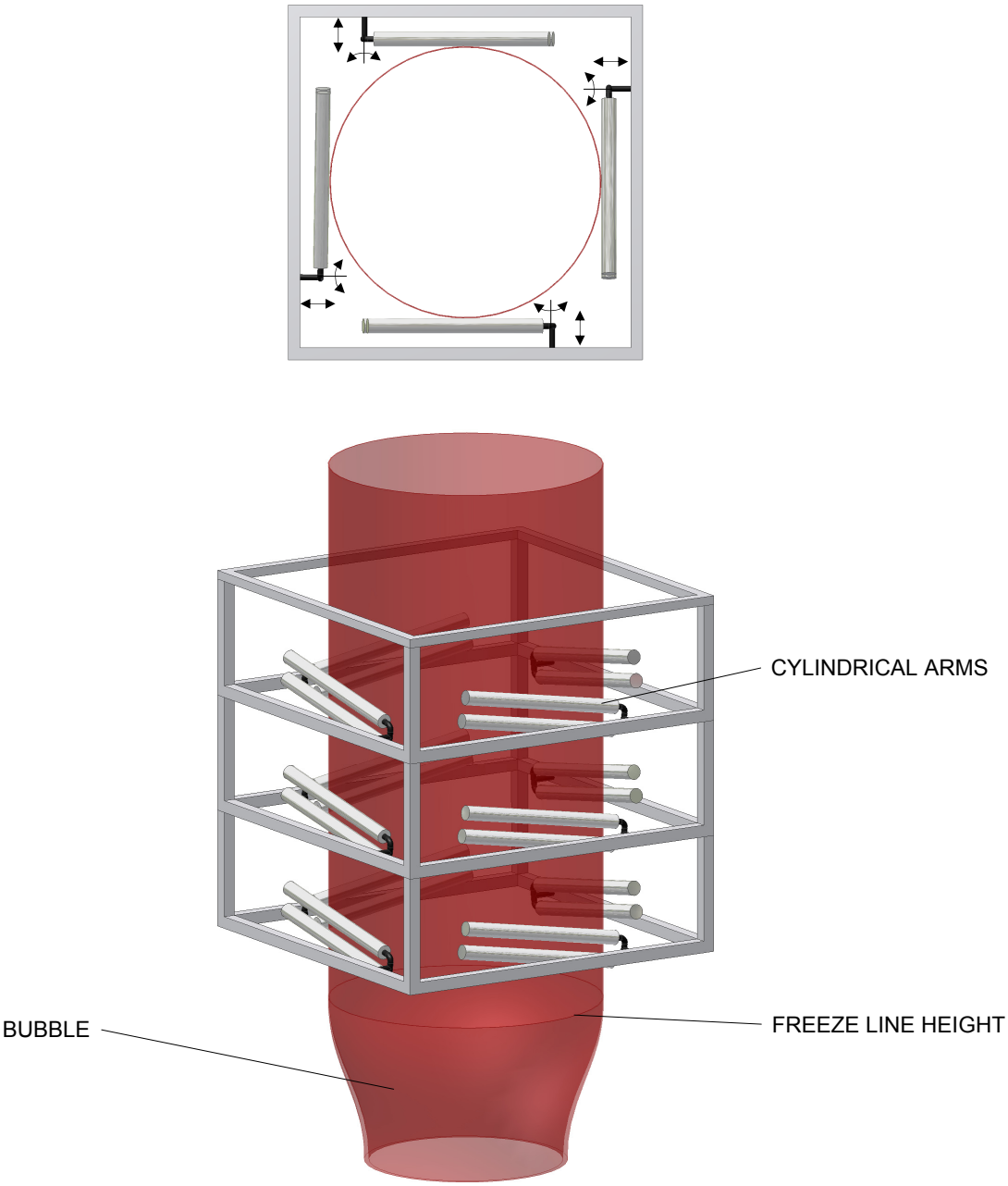

Fig. 22. Bubble guides – type B

2.2.3 Bubble calibration cage

Another method to stabilize solid bubble is a bubble cage (Fig. 23) [13]. This device limits the lateral movement of the bubble and it lowers the bubble tension. The cage,

surrounding the film bubble, consists of a frame, arms and segmented rollers. The frame holds the cage and it provides a possibility to attach IBC sensors, and it also provides setting of the cage height with regard to variable freeze line height. The bubble cage is concentric to minimize friction. Then, the dimensions uniformity is better. A bubble cage is part of every film blowing line [13].

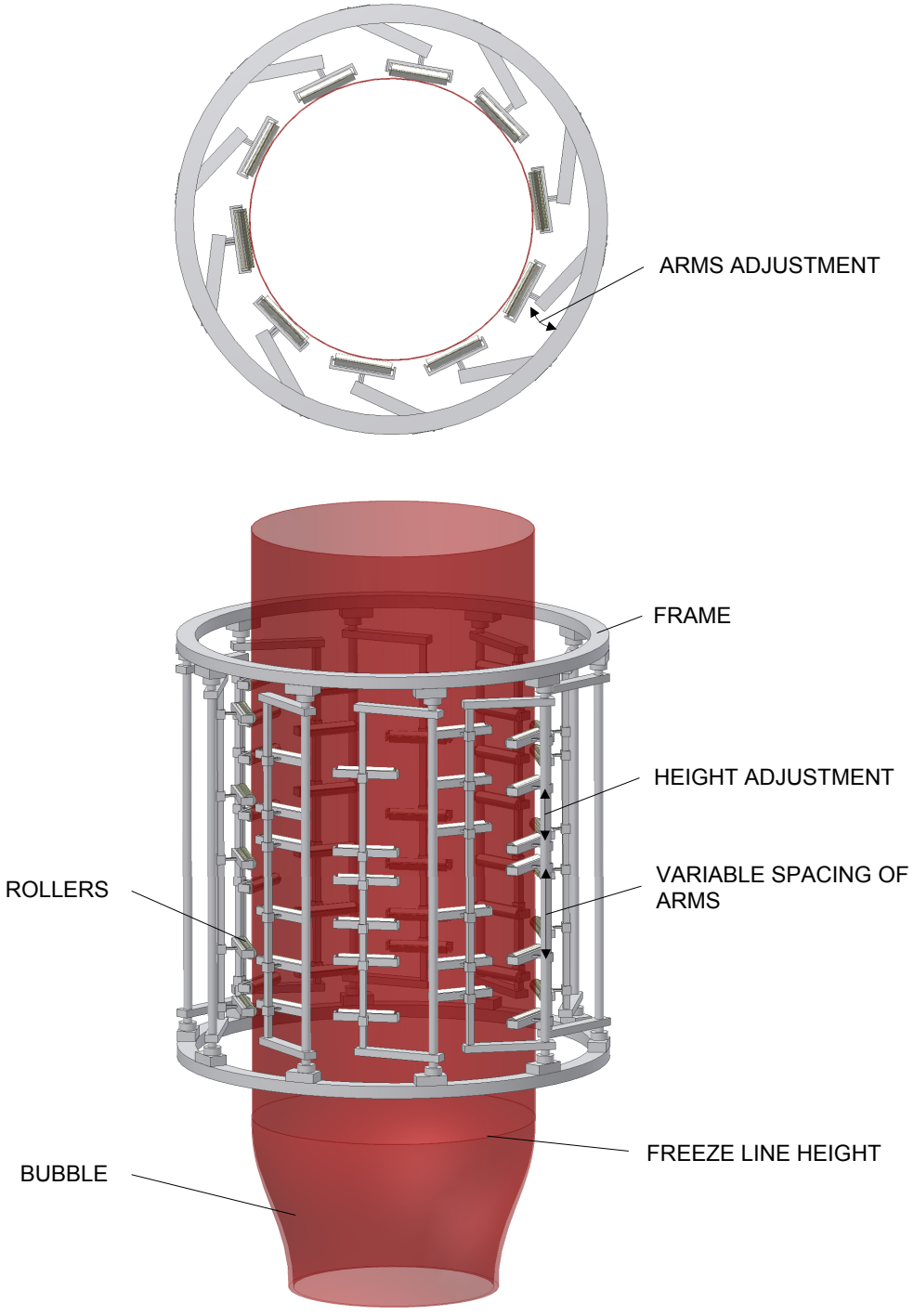

Fig. 23. Bubble calibration cage

3 MODELING OF THE FILM BLOWING PROCESS

Due to the fact, that film blowing instabilities described above represents the main limiting factor for this technology, any knowledge leading to their deeper understanding with respect to material property, die design and processing conditions are very welcome. Parametric study performed by the use of the film blowing modeling is widely used for such purpose. In the next section, the film blowing models are summarized and some of them are discussed in more detail.

3.1 Review of the current models

Tab. 2 summarized different film blowing models in chronological order based on the open research literature.

Tab. 2. Summary and description of the constitution equations for the solution of the film blowing process (adapted from [34]).

Author	*Model description*	*Limitations*
Pearson and Petrie [16, 35]	Isothermal Newtonian	Does not incorporate the non-Newtonian flow behavior of polymer melts
Petrie [36]	Non-isothermal Newtonian and isothermal purely elastic model. Effects of gravity and inertia included	Does not allow for viscoelastic response of materials
Han and Park [37]	Isothermal power law	Does not account for cooling of bubble and viscoelasticity
Wagner [38]	Non-isothermal integral viscoelastic equation with Wagner damping function	Complex, does not accurately estimate stresses at the die exit
Pearson and Gutteridge [39]	Non-isothermal elastic model	Does not allow for the viscoelastic response of materials
Gupta [40]	General non-isothermal White – Metzner equation	Used only for film blowing of PS bubbles
Kanai and White [41]	Non-isothermal Newtonian with crystallisation	Does not allow for non-Newtonian behavior of fluids

Author	*Model description*	*Limitations*
Luo and Tanner [4]	Non-isothermal Maxwell model and Leonov models joined together	Solutions highly unstable, the model does not account for non-linear viscoelasticity
Cain and Denn [42]	Marruci model	Does not account for multiple relaxation time spectrum
Seo and Wissler [43]	Isothermal Newtonian	Does not attempt non-Newtonian due to the high Weisenberg effect
Cao and Campbell [44, 45]	Non-isothermal Maxwell model extended above the freeze line with Hookean elastic model	Highly unstable, does not predict creep flow very well
Ashok and Campbell [5]	Maxwell model with a single relaxation time and the Oldroy	Does not allow extrudate swell and temperature gradient across the film
Alaie and Papanastasiou [46]	Non-isothermal integral viscoelastic equation with PSM damping function	Complex, difficult to estimate previous shear history of polymer melt, particularly at the die exit
Liu et al. [47]	Quasi cylindrical bubble combined with non-isothermal power law with crystallization effects constitutive equation	Does not allow for axial curvature of bubble and viscoelastic properties of melt
Sidiropoulos et al. [48, 49]	Modified non-isothermal Newtonian	Does not allow for viscoelastic nature of polymer melt
Kuijk et al. [50]	Comprehensive model for film blowing	Used only for film blowing of PE bubbles
Zatloukal and Vlcek- *(variational principles 1)* ***[7]***	Isothermal elastic model (Hookean)	Does not account for the flow behavior and the bubble movement
Zatloukal and Vlcek- *(variational principles 2)* ***[6]***	Isothermal Newtonian	Does not incorporate the non-Newtonian flow behavior of polymer melts
Zatloukal and Vlcek- *(variational principles 3)* ***[8]***	Non-isothermal non-Newtonian	Membrane approximation. Does not account for flow memory

It is obvious that many film blowing models are based on the Pearson and Petrie formulation [1, 16, 35]. The recently proposed film blowing model based on minimum energy approach and variational principles [6-8] seems to be breakthrough in the film blowing modeling because it is numerically stable, gives realistic predictions and it can also be coupled with the Pearson and Petrie formulation, as shown in [6]. Hence, in the next section the specific attention will be paid only to these two formulations.

3.2 Pearson and Petrie formulation

The first and the most important contribution to modeling of the film blowing process were given by Pearson and Petrie [1, 2, 11] who developed basic and simple kinematic frame of the film blowing process. In their pioneering work, they have employed Newtonian model as the constitutive equation and the process has been assumed to be isothermal. Pearson and Petrie formulation [1, 2] is based on the following assumptions: (see Fig. 24 for more details):

- Membrane theory: the bubble is described as a thin shell where the film thickness, h, is much smaller than the bubble radius, r ($h << r$).
- The bubble movement is time steady and symmetrical around the bubble axis.
- The surface and inertial stresses are neglected due to their low values.

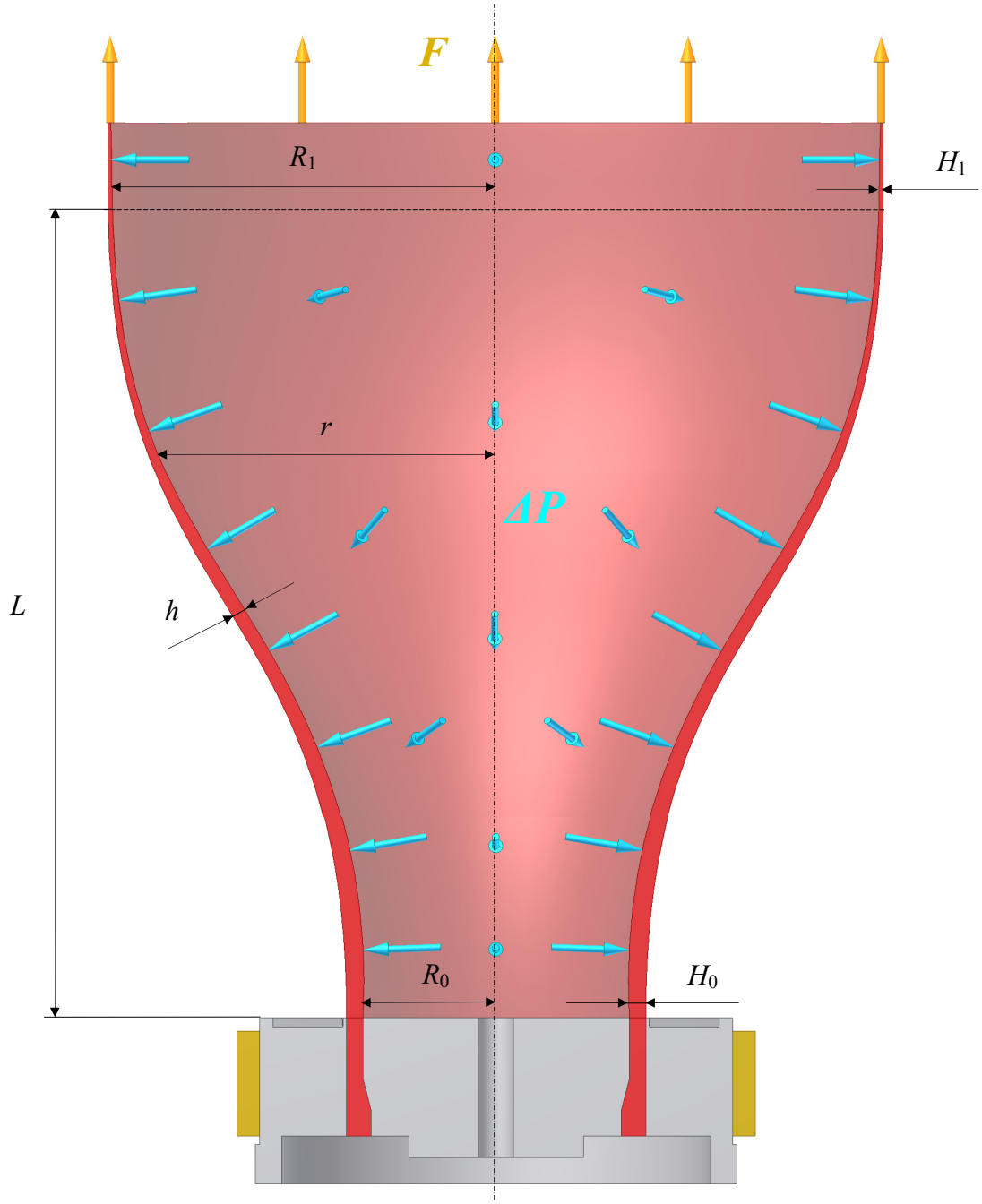

Fig. 24. Film blowing variables

The Pearson and Petrie have used a local Cartesian coordinate system where x_1 represents the tangential direction, x_2 is the thickness direction, and x_3 means the circumferential direction (Fig. 25).

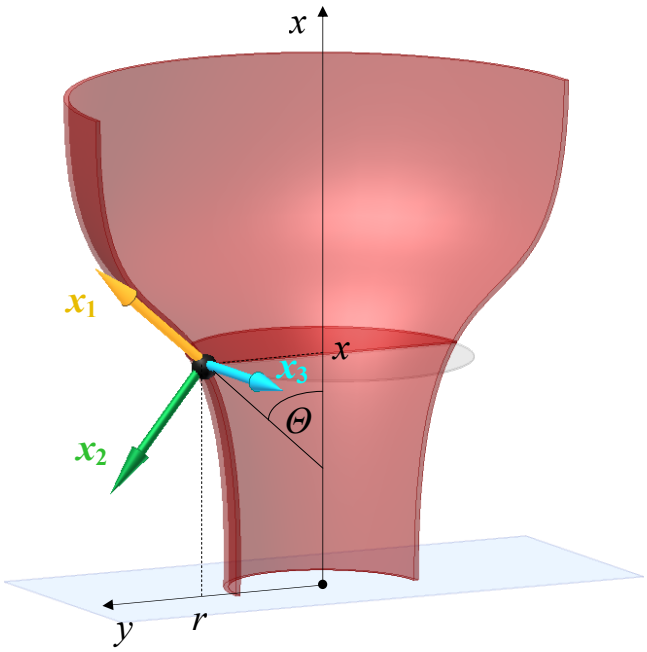

Fig. 25. Cartesian coordinate system

The Mathematically, Pearson and Petrie formulation is given by the set of equations provided in Tab. 3.

Tab. 3. A full set of the Pearson and Petrie equations.

Equation type	***Equation form***	***Equation number***
Continuity equation	$\dot{m} = 2\pi r(x)h(x)v(x)\rho(T(x))$	(7)
Density	$\rho(T) = \dfrac{1}{\dfrac{R_g T}{P * w} + b'}$	(8)
Internal bubble pressure	$\Delta P = \dfrac{h\sigma_{11}}{R_m} + \dfrac{h\sigma_{33}}{R_t}$	(9)
Curvature radius - tangential	$R_t = \dfrac{r}{\cos(\theta)}$	(10)
Curvature radius - circumferential	$R_m = \dfrac{-1}{\dfrac{d^2 r}{dx^2}\cos^3(\theta)}$	(11)

Equation type	*Equation form*	*Equation number*
Term	$\cos(\theta) = \frac{1}{\sqrt{1+\left(\frac{dr}{dx}\right)^2}}$	(12)
Force balance	$2\pi r h \sigma_{11} \cos(\theta) = F - \pi \Delta P \left(r_f{}^2 - r^2\right)$	(13)
Stress σ_{11}	$\sigma_{11}(x) = \frac{F - \pi \Delta P \left(r_f{}^2 - r(x)^2\right)}{2\pi r(x) h(x) \cos(\theta(x))}$	(14)
Tangential stress $\sigma_{11}(L)$ ***at the freeze line height***	$\sigma_{11}(L) = \frac{F}{2\pi R_1 H_1}$	(15)
Stress in the circumferential direction	$\sigma_{33}(x) = \frac{R_t(x)}{h(x)}\left(\Delta P - \frac{h(x)}{R_m(x)}\sigma_{11}(x)\right)$	(16)
Circumferential stress at the freeze line height	$\sigma_{33}(L) = \frac{R_1}{H_1}\Delta P$	(17)
Proportion between the total stresses, σ ***, and the extra stresses,*** τ	$\sigma_{11} = \tau_{11} - \tau_{22}$ $\sigma_{22} = 0$ $\sigma_{33} = \tau_{33} - \tau_{22}$	(18)

The meaning of the used symbols is following: x represents particular location at the bubble, $\dot{m}$ is the mass flow rate, $r(x)$ the bubble radius, $h(x)$ the film thickness, $v(x)$ the film velocity, $T(x)$ the temperature and $\rho(T)$ is the density (which is described below in more detail), ΔP is the internal bubble pressure, σ_{11} is the tangential directions of the stress, R_m is radius curvature, σ_{33} is circumferential directions of the stress, R_t is radius curvature , r_f is the bubble radius at the freeze line height, F means the take-up force, G stands for the gravity, and H is the force created by the air flow. The bubble radius at the freeze line height is, $R_1 = BURR_0$, and H_1 is the bubble thickness at the same place.

It should be mentioned that Eq. (8) for temperature dependent density has been derived by Spencer and Gilmore [51] with following symbol meaning: *w is* the molecular weight, R_g represents the universal gas constant ($R_g = 8.314 J \cdot K^{-1} \cdot mol^{-1}$), P^* is the cohesion pressure, and b' means the specific volume. As has been shown by Hellwege et al. [52],

these parameters for PEs, takes the following forms: $w = 28 \cdot 10^{-3} kg \cdot mol^{-1}$, $b' = 8.75 \cdot 10^{-4} m^3 \cdot kg^{-1}$ and $P^* = 3.18 \cdot 10^8 Pa$. Putting all these numbers into the Eq. (8), the following equation for temperature dependent density raised:

$$\rho(T(x)) = \frac{10^3}{0.934 \cdot 10^{-3} T(x) + 0.875} \tag{19}$$

Main problem with the Pearson and Petrie formulation is the occurrence of numerical instabilities [2, 4, 7, 9] and impossibility to represents real bubble shapes realistically [2, 7, 9, 53].

Numerical instabilities

These types of instabilities are usually caused by inability of the numerical scheme to converge for certain polymer rheology, processing and boundary conditions or by existence of the multiple solutions. Moreover, the solution is very sensitive to the initial bubble angle at the die exit as well as to melt history which is related to the die flow. Due to that, the solution is available for only a small area of the operating conditions. This is discussed in more detail by Luo and Tanner [4].

Problems with the bubble-shape description

These problems are connected with high stalk bubbles, i.e. bubbles with a long neck. Here, the bubble shape with the original elongated neck is not described exactly - the predicted values are set in earlier than the elongated neck of the bubble in reality [2, 7, 9, 53].

The presented problems of Pearson and Petrie formulation can be eliminated by the application of Zatloukal and Vlcek´s formulation derived through variational principles, which is described in the following parts in more detail.

3.3 Zatloukal and Vlcek formulation

The Zatloukal and Vlcek formulation regards existence of the stable film blowing process as a situation which is accordant with minimum energy requirements. If the

condition is not fulfilled, the film bubble can be considered as unstable. This variational principle can be used to derive a model which describes the bubble creation. In more detail, it is well-known that bubble shape changes during the film blowing process. It happens due to the internal load, p, and the take-up force, F. The bubble can be thought as a static flexible membrane. Thus, the thickness is a neglected parameter because the membrane is very thin [2]. Two bubble shapes can be created. First, the bubble before deformation (Fig. 26) [2, 7, 9]; here the line element of the membrane is dx, and second, the bubble after deformation (Fig. 27), where the element length is given by the following equation [2, 7, 9]:

$$\sqrt{1+(y')^2}\,dx \approx \left[1+\frac{1}{2}(y')^2\right]dx \tag{20}$$

It has been shown in [7] that if the constant bubble compliance is assumed, one can derive the analytical equation for the bubble shape satisfying the minimum-energy requirements by using variational principles [2].

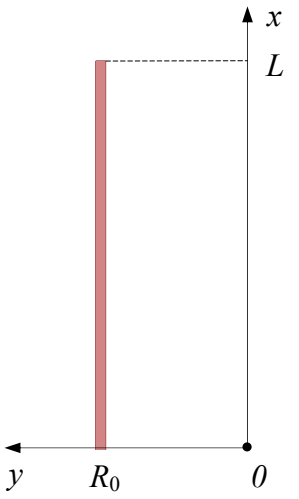

Fig. 26. Membrane before deformation

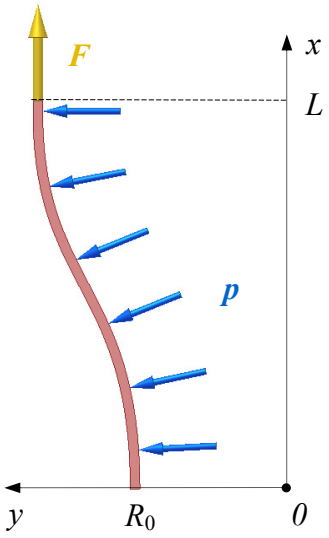

Fig. 27. Membrane after deformation

This model can be used for different processing conditions, which leads to different bubble types, as will be discussed bellow in more detail.

3.3.1 Bubble without neck

The bubble without the neck is typical for LLDPE and LDPE due to their higher melt strength [3]. Four parameters have to be known for the bubble shape description: freeze line height, L, bubble curvature pJ (which is given by membrane compliance, J, and the internal load, p), the blow up ratio, BUR, and the die radius, R_0 [2]. In this case, Zatloukal-Vlcek model is given by the set of equations, which are provided in Tab. 4 and Tab. 5. The comparison between experimentally measured and theoretically predicted bubble shapes for LLDPE is provided in Fig. 28. As reported in [7], the model has very good capability to describe this type of the bubble shape.

Tab. 4. Summary of the Zatloukal-Vlcek model for the bubble without neck.

Equation type	***Equation form***	***Equation number***
Differential equation	$Fy'' - \lambda_1 2\pi y + p = 0$	(21)
Bubble shape	$y = (R_0 - pJ)\cos\left(\frac{x\varphi}{L}\right) - \alpha'(pJ - BURR_0)\sin\left(\frac{x\varphi}{L}\right) + pJ$	(22)
Parameter	$x \in < 0; L >$	(23)
Parameter	$\alpha' = \sqrt{\frac{2pJ - R_0 - BURR_0}{pJ - BURR_0}\left\lvert\frac{R_0(BUR-1)}{pJ - BURR_0}\right\rvert}$	(24)
Parameter	$A = \frac{pJ - R_0}{pJ - BURR_0}$	(25)
Take-up force	$F = -\frac{L^2}{J\varphi^2}$	(26)

The symbol meaning is following: F is the take-up force, λ_1 stands for the Lagrange multiplier, p means the internal load. Parameter φ is given by a parameter (Eq. (25)) according to Tab. 5.

Tab. 5. Parameters A and φ for different bubble shapes (y). Parameters A′, A′′ are equal to A and parameters φ′, φ′′ are the same as φ [2].

Equation	***A***	***φ***	***y***
1.	1	0	R_0
2.	$0 < A < 1$	$arctg\left(\frac{\sqrt{1-A^2}}{A}\right)$	The form of Eq. (22)
3.	0	π/2	$R_0\left\{1-\sin\left(\frac{x\pi}{2L}\right)(1-BUR)\right\}$
4.	$-1 < A < 0$	$\pi + arctg\left(\frac{\sqrt{1-A^2}}{A}\right)$	The form of Eq. (22)
5.	-1	π	$\frac{R_0}{2}\left\{1+\cos\left(\frac{x\pi}{L}\right)(1-BUR)+BUR\right\}$

The Zatloukal-Vlcek model which is given by Eqs. (15), (17), (22, 24-26), (28-33), (35), (37) and Tab. 5 will be used in the theoretical part of the Master thesis.

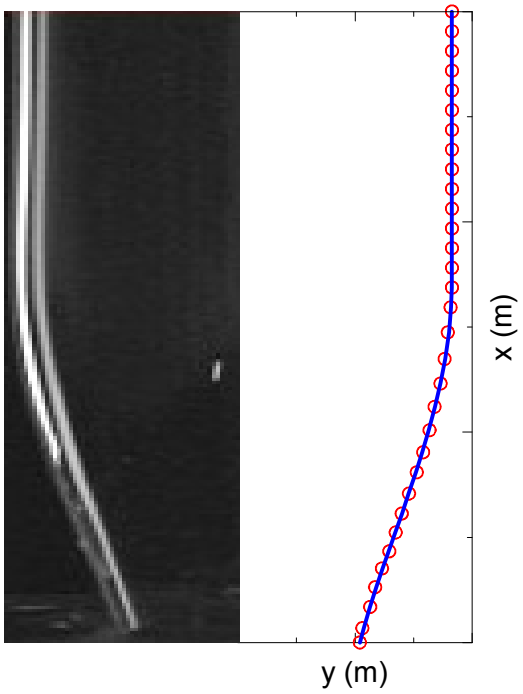

Fig. 28. Bubble without neck [2]. Left side represents measurements, right hand side represents prediction.

3.3.2 Bubble with neck

A typical material which creates bubbles with the neck is HDPE which is caused by its extensional strain thinning behavior.

This type of the bubble consist of two sections (Fig. 29) [2, 7]. The first part of the bubble is influenced by the uniaxial stretching (up to the distance L_1) where the radius of the bubble is changed from R_0 to BUR_0R_0. At the end of the second part of the bubble i.e. at the freeze line height region, the radius of the bubble is given as $BURR_0$ which is clearly visible in Fig. 29. In this case, the Zatloukal-Vlcek formulation is given by the set of equations provided in Tabs. 5-6. The Fig. 30 compares experimentally determined bubble shape for LLDPE, under processing conditions at which bubble with the neck is created, and Zatloukal-Vlcek model (see [7] for more detail). Also in this case, the agreement between model prediction and measured data is very good.

Tab. 6. Zatloukal-Vlcek model for the bubble with the neck.

Equation type	***Equation form***	***Equation number***
Differential equation	$Fy'' - \lambda_1 2\pi y + p = 0$	(27)
Bubble shape in section I	$y_1 = (R_0 - pJ)\cos\left(\frac{x\varphi''}{L_1}\right) + \alpha''(pJ - BUR_0R_0)\sin\left(\frac{x\varphi''}{L_1}\right) + pJ$	(28)
Blow up ratio in L_1	$BUR_0 = \frac{BURR_0}{2pJ - R_0}$	(29)
Parameter	$\alpha'' = \sqrt{\frac{2pJ - R_0 - BUR_0R_0}{pJ - BUR_0R_0}\left\lvert\frac{R_0(BUR_0 - 1)}{pJ - BUR_0R_0}\right\rvert}$	(30)
Parameter	$A'' = \frac{pJ - R_0}{pJ - BUR_0R_0}$	(31)
The neck height L_1	$L_1 = \frac{\varphi''\left(L\varphi'' - \pi\sqrt{-\xi}\right)}{\varphi''^2 - \pi^2}$	(32)

Equation type	*Equation form*	*Equation number*
Parameter	$\xi = pJR_0\left(2BUR_0 - 1 - BUR\right)\left(\pi^2 - \varphi''^2\right) - L^2$	(33)
Tensile force at the die exit	$F_I = -\frac{L_1^2}{\varphi''^2 J}$	(34)
Bubble shape in section II	$y_2 = BUR_0\left\{pJ + \cos\left[\frac{(x - L_1)\pi}{L - L_1}\right]\left(R_0 - pJ\right)\right\}$	(35)
Tensile force at the freeze line height	$F_{II} = -\frac{\left(L - L_1\right)^2}{\pi^2 J}$	(36)
Internal bubble pressure	$\Delta p = \frac{pL}{2\pi\int_0^L y\sqrt{1 + \left(y'\right)^2}\,dx}$	(37)
Surface of the bubble	$2\pi\int_0^L y\sqrt{1 + \left(y'\right)^2}\,dx$	(38)

Note, that parameter φ'' is identified with the aid of Tab. 5 according to value A''. Thus, parameters A' and A'' are equal to A. The same rule is valid for parameters φ', φ'', pL then represents the force acting at the bubble thickness in the perpendicular direction.

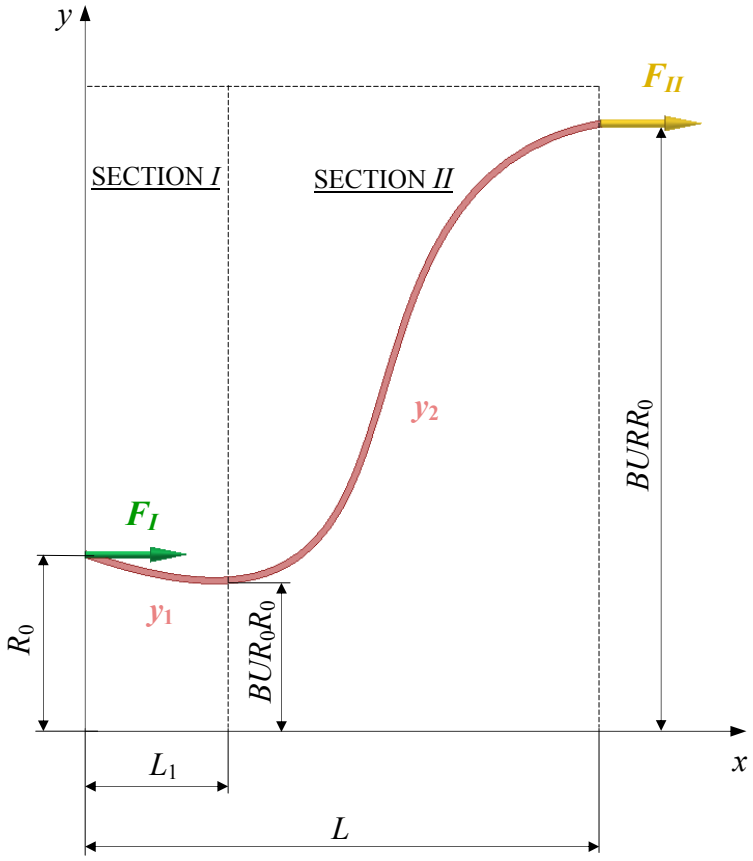

Fig. 29. Bubble with neck – shape and acting forces

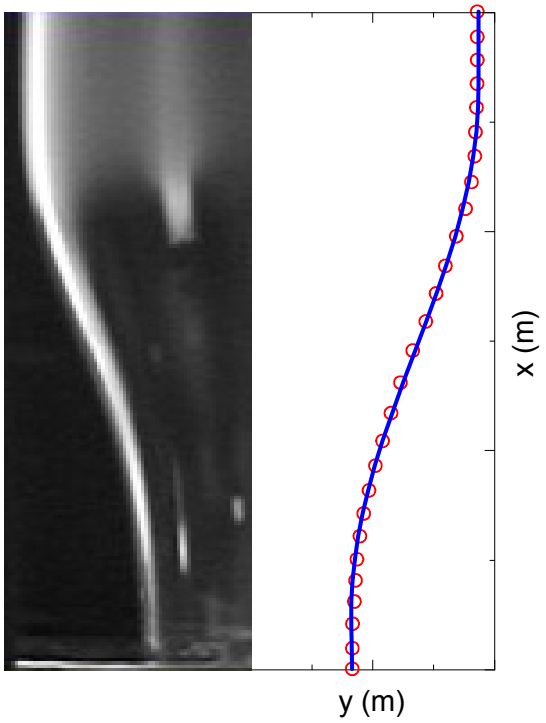

Fig. 30. Bubble with the neck [2]. Left side represents measurements, right hand side represents prediction.

3.3.3 High stalk bubble

The term high stalk bubble means that the bubble has an extremely long neck. The typical material which creates this kind of bubble shape is high molecular weight HDPE. The thin film which is created by bubble stabilizing equipment at high take-up ratio has high toughness [6].

This type of the bubble consists of two regions. In Region *I* the biaxial deformation is negligible, i.e. the bubble radius can be considered constant. On the other hand, in Region *II* the biaxial deformation is considerable due to bubble inflation (see Fig. 31 for more detail).

For this type of the bubble, Zatloukal-Vlcek model is given by the equations provided in Tab. 7.

Tab. 7. Zatloukal-Vlcek model for the high stalk bubble.

Equation type	***Equation form***	***Equation number***
Bubble shape in Region I	$y_1 = (R_0 - pJ_1)cos\left(\frac{x\varphi'}{L_1}\right) + \alpha'(pJ_1 - BUR_0R_0)sin\left(\frac{x\varphi'}{L_1}\right) + pJ_1$	(39)
Blow up ratio in L_1	$BUR_0 = \frac{BURR_0}{2p_2'J_2' - R_0} = \frac{2pJ_1}{R_0} - 1$	(40)
Parameter	$\alpha' = \sqrt{\frac{2pJ_1 - R_0 - BUR_0R_0}{pJ_1 - BUR_0R_0}\left\lvert\frac{R_0(BUR_0 - 1)}{pJ_1 - BUR_0R_0}\right\rvert}$	(41)
Parameter	$A' = \frac{pJ_1 - R_0}{pJ_1 - BUR_0R_0}$	(42)
The neck height L_1	$L_1 = \frac{\varphi'\left(J_1L\varphi' - \pi\sqrt{-\xi J_1J_2'}\right)}{\varphi'^2 J_1 - \pi^2 J_2'}$	(43)
Parameter	$\xi = R_0\left[pBUR_0 - p - p_2'(BUR - BUR_0)\right]\left(\pi^2J_2' - \varphi^2J_1\right) - L^2$	(44)
Load in Region II	$p_2' = p + 4E_2\pi^2E_0$	(45)

Equation type	Equation form	Equation number
Membrane compliance in Region II	$J_2 = \left[\frac{2p_2'}{R_0(1+BUR/BUR_0)} - 4E_2\pi^2 \right]^{-1}$	(46)
Membrane compliance in Region II	$J_2' = \frac{1}{1/J_2 + 4E_2\pi^2}$	(47)
Bubble shape in Region II	$y_2 = BUR_0 \left\{ p_2'J_2' + cos\left[\frac{(x-L_1)\pi}{L-L_1} \right] \left(R_0 - p_2'J_2' \right) \right\}$	(48)
Tensile forces	$F_I = -\frac{(L_1)^2}{\varphi'^2 J_1} + pR_0(1-BUR_0) \qquad F_{II} = -\frac{(L-L_1)^2}{\pi^2 J'_2} - p_2'R_0(BUR-BUR_0)$	(49)
Internal bubble pressure	$\Delta p = \frac{p_2'L}{2\pi \int_0^L y\sqrt{1+(y')^2}\,dx}$	(50)

Here, the J_1 is membrane compliance in Region *I*, and parameter E_2 is the Young´s modulus of the membrane. The total number of the input parameters is six: p, J_1, E_2, L, R_0 and BUR.

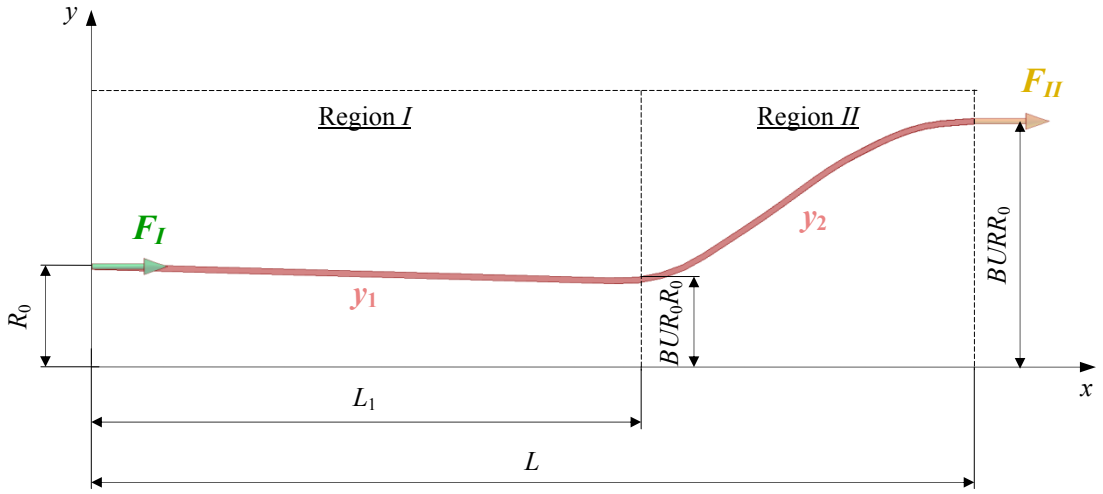

Fig. 31. High stalk bubble – shape and acting forces

The comparison between the model prediction and experimentally determined high stalk bubble shape is depicted in Fig. 32 [6]. Also in this case, the agreement between the model prediction and measured data is very good.

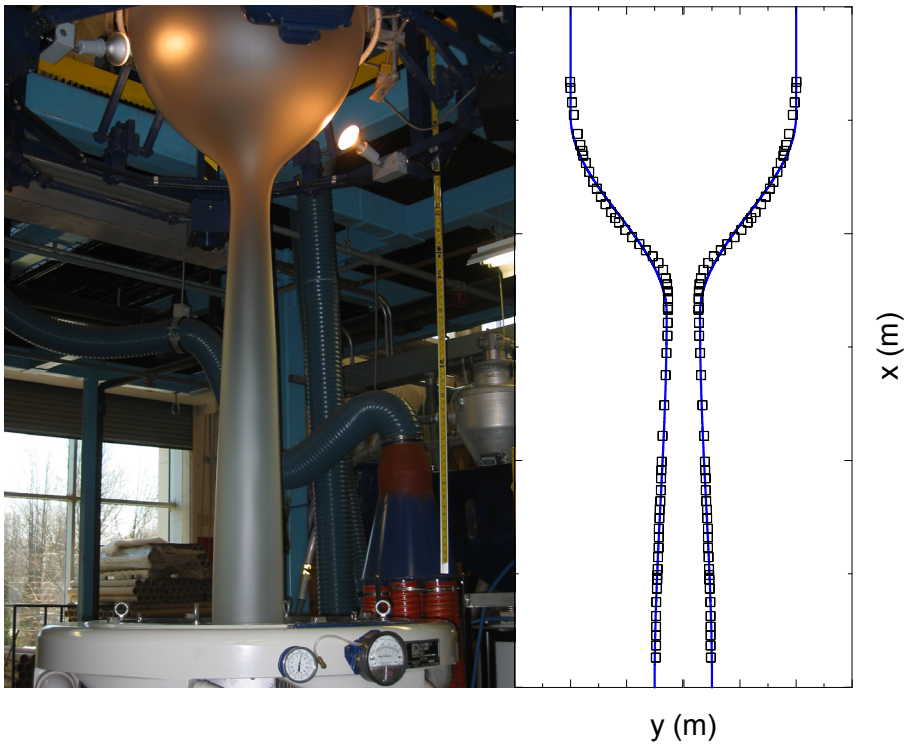

Fig. 32. High stalk bubble [6]. Left side represents measurements, right hand side represents prediction.

3.3.4 Stability diagram

In this work, it is considered that the stability diagram is given by three different stability contours: model contour (above this contour the film blowing process does not satisfy the minimum energy requirements), machine contour (bellow this contour the machine direction stress at the freezeline height achieves rupture stress, which leads to bubble tear) and circumference contour (bellow this contour the circumference direction stress at the freezeline height achieves rupture stress, which leads to bubble tear). The mathematical formulas for all three stability contours are summarized Tab. 8. Derivation of all these equations is provided in [54]. A stable processing window is defined as an area in the graph of relative final film thickness, H_1/H_0, vs. BUR. It should be mentioned that the film blowing process does not satisfy the minimum energy requirements if $A < -1$.

Tab. 8. The stability contour equations.

Stability contour	***Equation title***	***Equation form***	***Equation number***
Model stability contour	***The membrane compliance***	$J = \frac{R_0}{2p}(1+BUR)$	(51)
	The extensional rate	$\dot{\varepsilon}_1 = \frac{v_F - v_D}{L}$	(52)
	The film velocity at the freeze line height and die	$v_F = \frac{Q}{2\pi R_0 BURH_1} \quad v_D = \frac{Q}{2\pi R_0 H_0}$	(53)
	The film thickness at the freeze line height	$H_1 = H_0 \frac{R_0(1+BUR)Q\eta_0\pi^2 - pL^3}{\pi^2 R_0 \eta_0 QBUR(1+BUR)}$	(54)
Machine stress stability contour	***The total stress in machine direction***	$\sigma_{11} = 4\eta_0 \dot{\varepsilon}_{11}$	(55)
	The film thickness at the freeze line height	$H_1 = H_0 \frac{2Q\eta_0}{BUR(\sigma_{11} L\pi R_0 H_0 + 2\eta_0 Q)}$	(56)
Circumference stress stability contour	***The film thickness at the freeze line height***	$H_1 = \frac{R_0 BUR}{\sigma_{33}}\Delta p$	(57)
	Implicit equation for the BUR definition	$0 = \frac{pL^3\sigma_{33}(A-1)H_0}{2Q\varphi^2 R_0(R_0\Delta pBUR^2 - \sigma_{33}H_0)(1-ABUR)} - \eta_0$	(58)

The symbol description for all above mentioned equations is provided at the end of this thesis in the List of symbols chapter. It should be mentioned that above mentioned equations were derived under the assumption that the polymer melt behaves as the Newtonian fluid and that the film blowing process is isothermal, i.e. freezeline height, *L*, has been considered to be one adjustable processing parameter.

3.3.5 Energy equation

The assumption about the isothermal film blowing process is relaxed here by assuming the cross-sectionally average energy equation (the bubble is a quasicylinder at each point) taken from [55]:

$$\rho C_p \frac{dT}{dx} = -\frac{2\pi R\rho}{\dot{m}}\left[h\left(T - T_{air}\right) + \sigma_B \varepsilon\left(T^4 - T_{air}^4\right)\right] + \tau : \nabla v + \rho \Delta H_f \frac{d\phi}{dx} \tag{59}$$

where C_p stands for the specific heat capacity, ρ is the polymer density, R means the local bubble radius, h represents the heat transfer coefficient, T is the bubble temperature, T_{air} means the air temperature used for the bubble cooling , σ_B stands for the Stefan-Boltzmann constant, ε represents the emissivity, τ is the extra stress tensor, Δv means velocity gradient tensor, ΔH_f indicates the heat of crystallization per unit mass and ϕ is the average absolute degree of crystallinity of the system at the axial position, x.

In order to reduce the problem complexity, the axial conduction, dissipation, radiation effects and crystallization are neglected. For such simplifying assumptions, the Eq. (59) is reduced in the following, the simplest version of the cross-sectionally averaged energy equation:

$$\dot{m} C_p \frac{dT}{dx} = 2\pi y\left[h\left(T - T_{air}\right)\right] \tag{60}$$

where y is the bubble shape (given by Eq. (39) in Tab. 7), $\dot{m}$ represents the mass flow rate, h stands for the heat transfer coefficient, C_p is the specific heat capacity, T means the value of the bubble temperature and T_{air} represents the air temperature used for the bubble cooling. The Eq. (60) applied for the first part of the bubble takes the following form:

$$\int_{T_{die}}^{T_{solid}} \frac{\dot{m} C_p}{h\left(T - T_{air}\right)} dT = 2\pi \int_0^L y dx \tag{61}$$

where T_{die} and T_{solid} represents the temperature of the melt at the die exit and solidification temperature of the polymer, respectively. After integration from die temperature, T_{die}, up to freezeline temperature, T_{solid}, we can obtain equation defining the relationship between frezeline height, L, and heat transfer coefficient, h, which take the following simple analytical expression:

$$L = -\frac{1}{2}\dot{m} C_p \, ln\left(-\frac{\left(T_{die} - T_{air}\right)}{\left(-T_{solid} + T_{air}\right)}\right) \frac{\varphi}{\pi h\left(\alpha pJ - \alpha BURR_0 - sin(\varphi)R_0 - pJ\varphi + sin(\varphi)pJ - \alpha\, cos(\varphi)pJ + \alpha\, cos(\varphi)BURR_0\right)} \tag{62}$$

With the aim to get equations for the temperature profile along the bubble, it is necessary to apply the Eq. (60) for any arbitrary point at the bubble i.e. in the following way:

$$\int_{T_{die}}^{T} \frac{\dot{m}C_p}{h(T-T_{air})}dT = 2\pi \int_{0}^{x} y dx \tag{63}$$

After the integration of Eq. (14), the temperature profile takes the following analytical expression:

$$T = T_{air} + (T_{die} - T_{air}) exp\left\{ -\frac{2\pi Lh}{\dot{m}C_p \varphi}\left(-\alpha[R_0 BUR - pJ]\left[cos\left(\frac{x\varphi}{L}\right) - 1\right] + sin\left(\frac{x\varphi}{L}\right)[R_0 - pJ] + pJ\varphi\frac{x}{L}\right)\right\} \tag{64}$$

3.3.6 Constitutive equations

Constitutive equations represent mathematical relationships which are derived from constitutive models containing various assumptions and idealizations about the molecular or structural forces and motions producing stress. Constitutive equations enable computing polymer melt stress response on the given flow field. Polymers, which lie between Newtonian liquids and Hookean solids, contain relatively long macromolecules and thus they cannot be described by simple physical laws [26, 56, 57]

A summary of the various rheological constitutive equations utilized in the film blowing process modeling is presented above in Tab. 2. As can be seen, a number of constitutive equations having differential or integral form have already been utilized. In this work, the recently proposed generalized Newtonian model will be considered [56] with the aim to minimize the complexity of the problem. The main advantage behind this model is possibility to express all stress components as the analytical function of deformation rate even for complex flows where shear and extensional flows are mixed together. Moreover, specific form of the generalized Newtonian model, described bellow, allows taking both shear thinning as well as extensional viscosity strain hardening/thinning behavior properly into account [56]. The model takes the following form:

$$\tau = 2\eta D \tag{65}$$

where τ means the extra stress, D represents the deformation rate tensor and η stands for the viscosity, which is not constant (as in the case of standard Newtonian law), but it is

allowed to vary with second, II_D, and third, III_D, invariants of deformation rate tensor according to Eq. (66)

$$\eta\left(II_D, III_D\right) = \eta\left(II_D\right)^{f\left(III_D\right)} \tag{66}$$

where $\eta\left(II_D\right)$ and $f\left(T, III_D\right)$ are given by Eqs. (67-68)

$$\eta\left(T, II_D\right) = \frac{\eta_0 a_t}{\left[1 + \left(\lambda a_t \sqrt{2II_D}\right)^a\right]^{\left(\frac{1-n}{a}\right)}} \tag{67}$$

$$f\left(T, III_D\right) = \left[\frac{tanh\left(\alpha a_t \sqrt[3]{4\left|III_D\right|} + \beta\right)}{tanh(\beta)}\right]^{\xi} \tag{68}$$

where η_0, λ, a, n, β, α and ξ are adjustable parameters. Note that α is so called extensional strain hardening parameter. The uniaxial extensional viscosity, needed for model parameters identification process, is given by the following form:

$$\eta_E = \frac{\tau_{xx} - \tau_{yy}}{\dot{\varepsilon}} \tag{69}$$

where $\dot{\varepsilon}$ is extensional strain rate.

It should be mentioned that the temperature effect on the polymer melt rheology is taken into account through shift factor, a_t, defined through the following well known Arrhenius equation:

$$a_t = exp\left[\frac{E_a}{R}\left(\frac{1}{273.15 + \overline{T}} - \frac{1}{273.15 + T_r}\right)\right] \tag{70}$$

where E_a is the activation energy, R is the universal gas constant, T_r is the reference temperature and T is temperature.

3.3.7 Velocity profile

With the aim to calculate the velocity profile and the film thickness in the non-isothermal film blowing process, the force balance in vertical direction (gravity and upward force due to the airflow are neglected) proposed by Pearson and Petrie is considered in the following form:

$$\frac{2\pi yh\sigma_{11}}{\sqrt{1+(y')^2}} = F - \pi\Delta p\left(R_0^2 BUR^2 - y^2\right) \tag{71}$$

where σ_{11} is the total stress in the machine direction and F and Δp are defined by Eqs. (26) and (37) in Tab. 4 and Tab. 6. The deformation rate tensor in the bubble forming region takes the following form:

$$D = \begin{pmatrix} \dot{\varepsilon}_1 & 0 & 0 \\ 0 & \dot{\varepsilon}_2 & 0 \\ 0 & 0 & \dot{\varepsilon}_3 \end{pmatrix} \tag{72}$$

where the following deformation rate approximations have been used:

$$\dot{\varepsilon}_1 = \frac{dv}{dx} \approx \frac{v_f - v_d}{L} \tag{73}$$

$$\dot{\varepsilon}_2 = \frac{v}{h}\frac{dh}{dx} \approx \frac{\bar{v}}{\bar{h}}\frac{\bar{h} - H_0}{L} \tag{74}$$

$$\dot{\varepsilon}_3 = -\left(\dot{\varepsilon}_1 + \dot{\varepsilon}_2\right) \tag{75}$$

where v is velocity, v_f represents bubble velocity at the freezeline height, v_d is bubble velocity at the die, L is freezeline height, H_0 is bubble thickness at the die. Here, $\bar{v}$ and $\bar{h}$ is velocity mean value along the bubble and thickness mean value along the bubble, respectively, which are defines as follows:

$$\bar{v} = \frac{1}{L}\int_0^L v(x)dx \tag{76}$$

$$\bar{h} = \frac{1}{L}\int_0^L h(x)dx \tag{77}$$

Assuming that $h << y$, then

$$\sigma_{11} = \tau_{11} - \tau_{22} \tag{78}$$

By combination of Eqs. (59), (70), (78), the σ_{11} takes the following form:

$$\sigma_{11} = 2\eta\left(2\frac{dv}{dx} + \frac{v}{y}y'\right) \tag{79}$$

After substituting Eq. (79) into Eq. (70), the equation for the bubble velocity in the following form can be obtained.

$$v = v_{die}\, exp\left(\int_0^L \left\{ \frac{\sqrt{1+(y')^2}\left[F - \pi\Delta p\left(R_0^2 BUR^2 - y^2\right)\right]}{4Q\eta a_T} - \frac{1}{2y}y' \right\} dx \right) \tag{80}$$

Having the velocity profile, the deformation rates and the thickness can be properly calculated along the bubble.

3.3.8 Numerical scheme

In order to calculate stability contours for the film blowing process considering non-isothermal processing conditions and non-Newtonian polymer melt, it is necessary solved Eqs. (54), (56), (57) as well as implicit function Eq. (58) in Tab. 8. There are two important points which have to be carefully taken into account. First, the freezeline height is not adjustable parameter, which becomes constant during the calculation, but its value is determined by the processing, extrusion design and material parameters through Eq. (62). Second, the Newtonian viscosity η_0 has to be replaced by the representative 'bubble viscosity - $\bar{\eta}$' considering average bubble temperature, $(T_{die}+T_{solid})/2$, and components of the deformation rate tensor through second invariant of deformation rate tensor (see Eq. 81).

$$II_D = \sqrt{2\left(\dot{\varepsilon}_1^2 + \dot{\varepsilon}_2^2 + \dot{\varepsilon}_3^2\right)} \tag{81}$$

For particular processing conditions, iteration loop is needed to get for adjusted internal bubble pressure particular value of the take-up force which yields a priory known bubble velocity at the freezeline height. It is considered here, that the representative bubble viscosity is given by the bubble viscosity at the freezeline. It also has to be pointed out, that it is considered here that the bubble is characterized by one representative bubble viscosity value - $\bar{\eta}$' to get take-up force. However, to take the temperature profile correctly into account during velocity calculation, representative bubble viscosity is multiplied by the Arrhenius temperature shift factor in the Eq. (80). Finally, the following procedure has been used to solve Eq. (58) to obtain circumference stability contour: At the beginning, parameter A is adjusted to be equal to -1 and corresponding BUR is varied from 0 to 50. Then, consistent Δp is calculated. The step in BUR is adaptive to find out the BUR and

corresponding Δp satisfying Eq. (58) for A = -1. Then, the critical film thickness H_1 is calculated by using these two values and Eq. (57). This procedure is repeated for other values of A, which are varied between -1 and 1 with step 0.05. Of course, Newtonian viscosity has to be replaced by the representative bubble viscosity for particular processing/material/die design conditions calculated in the subroutine containing iteration scheme as described above.

4 AIMS OF THE WORK

The main aim of this work is to determine the stability contours (relative final film thickness vs. *BUR*) derived from the Zatloukal-Vlcek formulation for a non-isothermal conditions and non-Newtonian fluids. In more detail, the effect of material properties (Newtonian viscosity, rupture stress,, index of non-Newtonian behavior, extensional strain hardening, flow activation energy), process conditions (mass flow rate, heat transfer coefficient, internal bubble pressure, die exit temperature, cooling air temperature) and die design (die radius) on the bubble stability will be investigated. The predicted stability contours and trends will be compared and discussed with the real experimental data. Specific attention will be paid to the effect of the long chain branching on the stability of the film blowing process for linear, slightly branched and highly branched LLDPE.

II. EXPERIMENTAL

5 MATERIAL

In this work, three metallocene based LLDPEs (with chemically identical structure) having different level of the LCB were considered for the experiments on the film blowing line. The grades are referred to as mLLDPE low (virtually linear structure), mLLDPE middle (low level of LCB) and mLLDPE high (high level of LCB). Note, that the mLLDPE does not have as much LCB as a conventional LDPE. It should be pointed out that no additional information about these three materials are mentioned in this work because the institution providing these materials is wishing to keep this information as confidential.

6 FILM BLOWING EXPERIMENT

Pertinent film blowing processing parameters such as internal bubble pressure, Δp, volumetric flow rate, Q, die gap, H_0, bubble radius at the die exit, R_0, and freeze line height, L, were obtained from measurements on the film blowing line depicted in Fig. 33a, 33b in cooperation with Dr. Mike Martyn from Bradford University, UK.

33a

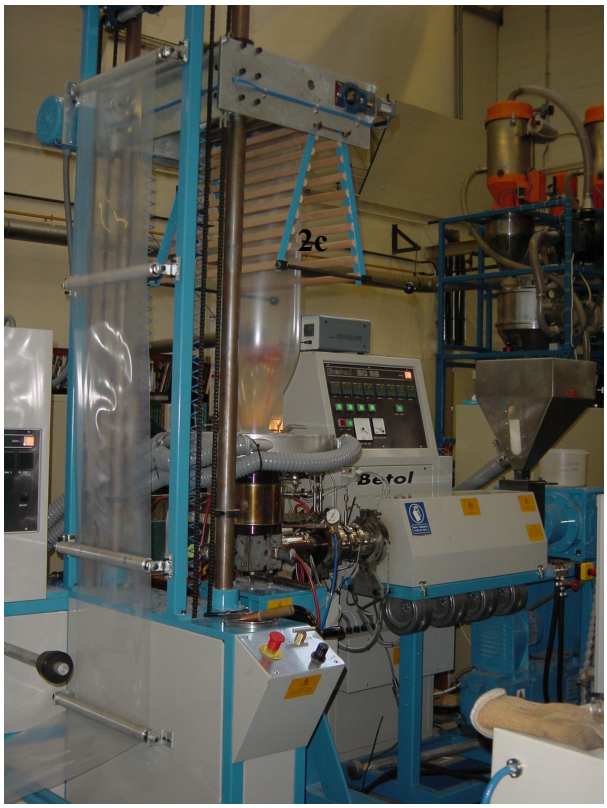

33b

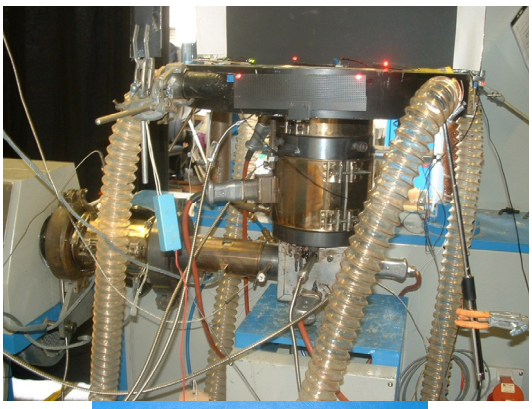

33c

Fig. 33. Film blowing experimental set-up. ***33a)*** *General view of the experimental film blowing line;* ***33b)*** *Closer view of the film blowing die;* ***33c)*** *Used spiral mandrel.*

The processing equipment comprised of a Betol BC 38*mm* single screw extruder equipped with a Davis Standard model DSBMT barrier screw and spiral mandrel die (Fig. 33c) having six feeding channels. The die annulus was 74*mm* in diameter and had a gap equal to 1.34*mm*. In-house software has been developed to measure the profile of the bubble. Bubble images taken with a Pulnix PEC 2010 CCD camera are captured using a bt878 based capture card. The edges of the bubble are determined by a simple thresholding technique. As no easily locatable features exist on the film to enable scaling, the

dimensions of the bubble are determined following a calibration stage that identifies the positions of four Light Emitting Diodes (LEDs). The basic point of the experimental work was the determination of the processing window for linear and branched mLLDPEs. The main experimental results are depicted in Fig. 34 where the experimentally determined stability diagrams (relative film thickness at the freeze line vs. *BUR*) for linear and branched mLLDPEs are provided.

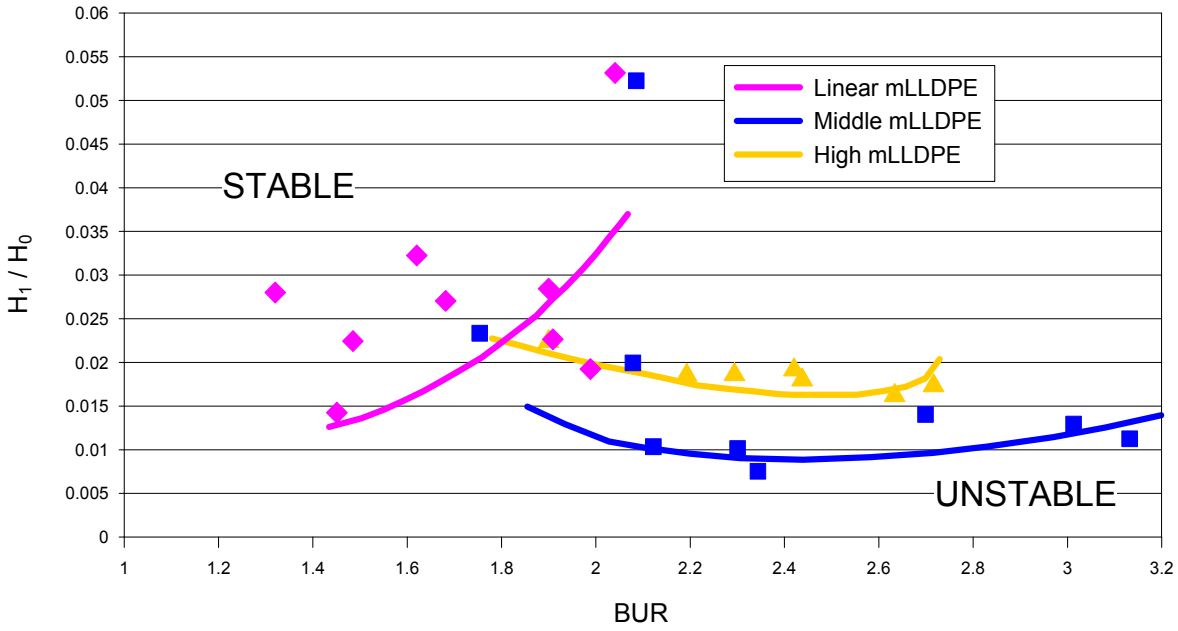

Fig. 34. The experimentally determined stability contours for both, linear and branched metallocene LLDPE samples (FLH 180mm and temperature 190°C).

The lines superimposed on Fig. 34 demark areas of stable and unstable bubble. The areas above the lines are stable, while those below the lines are regions of bubble instability. The experimental data clearly show that the branched mLLDPEs are much more stable compared to linear melts, i.e. branched mLLDPEs can be used to produce thinner film at a higher BUR. More importantly, these experimental results suggest that processibility of the mLLDPEs in film blowing process can be improved by increasing the content of LCB up to an optimum level. Increasing the LCB content beyond this level narrows the processing window for stable film production. These experimental data were taken as a basic for the testing of the recently proposed Zatloukal-Vlcek film blowing model. All three tested mLLDPEs were carefully characterized by Jan Musil Bachelor thesis [57] from the rheological point of view. In more detail, the frequency dependent

linear viscoleastic properties (storage modulus *G'*, loss modulus *G''*), of these three materials were measured with use of the Advanced Rheometric Expansion System (ARES 2000) Rheometrics rheometer. The transient uniaxial extensional viscosity of each melt was measured using the ARES 2000 rheometer equipped with the SER Universal Testing Platform (SER-HV-A01 model) from Xpansion Instruments [7]. The comparison between frequency dependent complex viscosity for all three samples is given in Fig. 35a. Clearly, the increase in the LCB slightly increases the Newtonian viscosity, however, at higher shear rates the viscosity for all three materials becomes almost identical. Finally, the extensional data in Fig. 35b clearly shows that increase in the LCB leads to strain hardening behavior leading to higher melt strength.

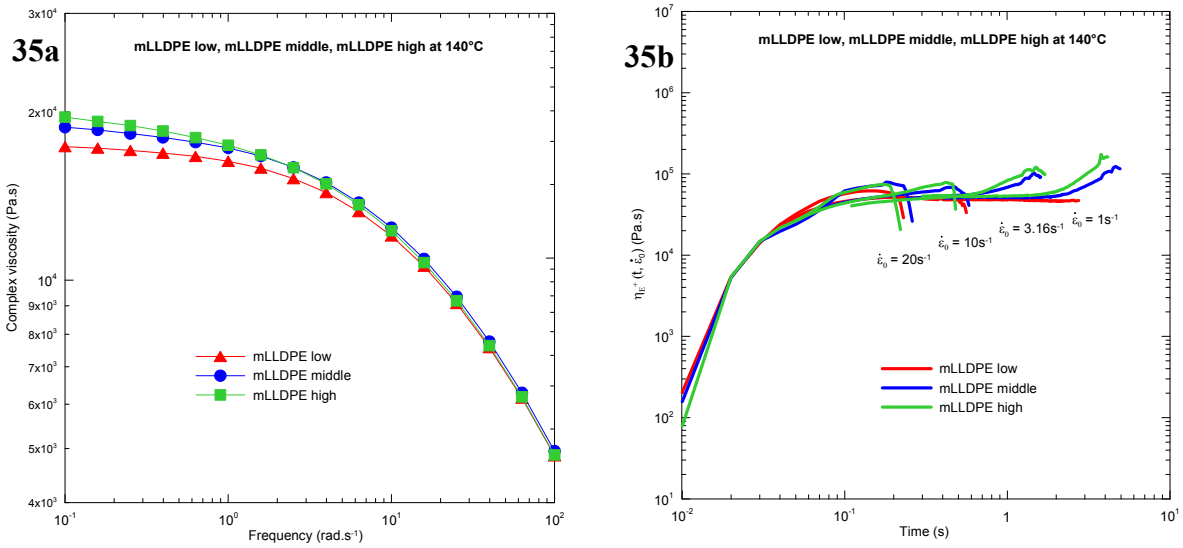

Fig. 35. Rheology data for tested resins taken from [57]; ***35a)*** *Complex viscosity data for three mLLDPEs having different levels of long chain branching obtained experimentally by ARES rotational rheometer at 140°C;* ***35b)*** *Time-dependent uniaxial extensional viscosity* $\eta_E^+(t)$ *data for three mLLDPEs having different levels of long chain branching obtained by SER at 140°C.*

RESULTS AND DISCUSSION

Theoretical film blowing stability analysis

The film blowing process stability has been theoretically analyzed by using above mentioned Zatloukal-Vlcek formulation considering particular processing and materials parameters summarized in Tab. 9. In more detail, all processing/material parameters were kept as constants whereas one chosen processing or material parameter was varied with the aim to reveal its impact on the film blowing stability window. In order to do theoretical analysis, it was crucially important to prepare suitable C++ program to apply both, iterative numerical schemes combined by the Regula Falsi method to achieve solution of particular stability contours.

Tab. 9. Zatloukal-Vlcek model parameters used in the model testing on the Tas's Ph.D. thesis data for LDPE.

Zatloukal-Vlcek film blowing model parameters					
η_0 (Pa·s)	$\dot{m}$ ($kg \cdot h^{-1}$)	Δp (Pa)	σ (MPa)	R_0 (m)	H_0 (m)
23809.6	4.20	108	0.800	0.0196	0.0008
Parameters of the generalized Newtonian constitutive equation					
a (-)	n (-)	α (s)	β (-)	λ (s)	ξ (-)
0.83	0.34	0.00001	$8.12409 \cdot 10^{-8}$	2.78	0.034289
Temperature parameters							
T_{AIR} (°C)	T_{SOLID} (°C)	T_{DIE} (°C)	T_R (°C)	h ($W \cdot m^{-2} \cdot K^{-1}$)	E_a ($J \cdot mol^{-1}$)	R ($J \cdot K^{-1} \cdot mol^{-1}$)	C_p ($J \cdot kg^{-1} \cdot K^{-1}$)
25	96	175	190	49.18	66000	8.314	2300

Zatloukal-Vlcek film blowing model test

At the beginning of the research, it is necessary to check, whether Zatloukal-Vlcek non-isothermal model for non-Newtonian polymer melts has capability to described

experimental reality with respect to bubble shape, velocity and temperature profiles. For the film blowing model test, experimental data for LDPE provided in the Tas's Ph.D. thesis [1] were used. As the first step, the rheological characteristic of the LDPE material taken from [1] were fitted by the generalized Newtonian model (Eq. 66). Fig. 36 clearly shows that the used generalized Newtonian model can describe extensional as well as shear viscosity data very well. All model, LDPE material and processing parameters for chosen processing conditions are summarized in Tab. 9.

Figs. 37-39 compare the calculated bubble shape, velocity and temperature profiles by using Zatloukal-Vlcek model. It is clearly visible that the bubble shape as well as velocity profile is in reasonable good agreement with the experimental data. The comparison between calculated and measured temperature profile reveals that even if the model predict proper trend, the discrepancy between theoretical and experimental data is high. This can be caused by the absence of the crystallization term in the energy equation. Moreover, by neglecting of temperature profile for the velocity profile calculation, may indeed leads to extremely high deviation between experimental reality and theoretical predictions as indicated in Fig 38. On the other hand by slight adjustment of the flow activation energy and die/solid temperature leads to much better agreement between measured and predicted velocity/temperature profile (see Fig. 38 and Fig. 39). Therefore, it can be concluded that the non-isothermal, non-Newtonian Zatloukal-Vlcek model may represent experimental reality reasonably and thus can be used for serious film blowing stability analysis.

It should be mentioned that the theoretical analysis of the film blowing model will be done with the processing/material parameters, which are summarized in Tab. 9 (except of Newtonian viscosity which will be equal to $200 kPa.s$ with the aim to emphasize particular stability contours details more properly).

Effect of Newtonian viscosity on the film blowing stability

Predicted effect of the Newtonian viscosity on the film blowing stability is depicted in Fig. 41. Clearly, increase in the Newtonian viscosity from $\eta_0 = 50 kPa \cdot s$ up to about $\eta_0 = 200 kPa \cdot s$ leads to the increase of the film blowing processing window. In more detail, if Newtonian viscosity increases in this range, the film blowing process becomes more stable at lower BUR (the minimum achievable film thickness is not influenced by the Newtonian viscosity in this case) and higher film thicknesses can be reached. On the other

hand, continues Newtonian viscosity increase above 200*kPa·s* does not seem to yield wider film blowing processing window. In this case, continues Newtonian viscosity increase above 200*kPa·s* causes higher film blowing process stability at low *BUR* for higher film thicknesses (which wider processing window at higher thicknesses similarly to low Newtonian viscosity range) but simultaneously blowing stability window is narrowing at small thicknesses. This interesting finding suggests that the relationship between Newtonian viscosity and film blowing stability has no monotonic character suggesting existence optimum value of Newtonian viscosity (or *Mw*) for needed *BUR* and particular final film thickness. All calculated parameters for this specific analysis are provided in Tab. 10.

Effect of heat transfer coefficient on the film blowing stability

Predicted effect of the heat transfer coefficient on the film blowing stability is visible in Fig. 42. In this case, low intensity bubble cooling (low heat transfer coefficient) leads to very narrow processing window whereas the increasing cooling intensity (heat transfer coefficient increases) causes wider processing window. This theoretical conclusion is in good agreement with open literature [27]. Interestingly, even if the cooling rate is small and processing window is very narrow in this case, it is possible to get much thinner final film thickness in comparison with high cooling rate condition at which so low final film thicknesses are not achievable. On the other hand, the obtained results suggest that for heavy-duty bags production (thick final film thickness is required) highly effective cooling system has to be utilized and thus one should take the cooling efficiency of the film blowing line properly into account. All calculated parameters for this specific analysis are provided in Tab. 11.

Effect of internal bubble pressure on the film blowing stability

Predicted effect of the internal bubble pressure on the film blowing stability is visible in Fig. 43. Clearly, internal bubble pressure increase leads to processing window narrowing and vice versa. In more detail, internal bubble decrease leads to higher stability especially at low *BUR* and high final film thicknesses. Interestingly, stability diagrams reported in this thesis are usually composed by two contours only (model and machine contours), which indicates machine stress dominance in comparison with circumference

stress. However, if the internal bubble pressure becomes high (above about 500*Pa*) the circumference stress can achieve rupture stress value much easily which limits minimum attainable final film thickness and maximum attainable *BUR*. All calculated parameters for this specific analysis are provided in Tab. 12.

Effect of melt strength on the film blowing stability

Predicted effect of the melt strength on the film blowing stability is visible in Fig. 44. Here it is nicely visible that melt strength (rupture stress) increase leads to processing window widening, especially from the minimum achievable final film thickness point of view. Interestingly, the model predict minimum value of the melt strength (slightly below 0.15*MPa* in this case), which is needed to realize stable film blowing process. Another important conclusion is that even if the melt strength increase leads to significant enhancement for thinner film at higher *BUR*, the capability to produce stable thicker films is not enhanced. All calculated parameters for this specific analysis are provided in Tab. 13.

Effect of die radius on the film blowing stability

Predicted effect of the die radius on the film blowing stability is visible in Fig. 45. Similarly to the Newtonian and isothermal film blowing stability analysis [2], the die radius has significant effect on the film blowing stability window (i.e. higher die radius, wider processing window and vice versa). Non-isothermal analysis has revealed that by using small film blowing lines (small die diameter), it is possible to achieve much thinner film at quite high *BUR* in comparison with film blowing dies with larger diameter. This can be explained by the fact that by keeping constant heat transfer coefficient it is much easier to cool down the bubble having small bubble surface (small bubble radius) than bubble having high bubble surface to be cooled down (high bubble radius). Therefore, during scale-up procedures the specific care should be done with respect to cooling rate conditions. All calculated parameters for this specific analysis are provided in Tab. 14.

Effect of mass flow rate, die exit temperature and cooling air temperature on the film blowing stability

Predicted effect of mass flow rate, die exit temperature and cooling air temperature on the film blowing stability is visible in Figs. 46-48. Here, increase in die exit temperature (melt temperature leaving the die) or mass flow rate or cooling air temperature always causes reduction of the film blowing stability window, which is in agreement with the open literature [27]. This theoretically obtained observation can be understood thought reduced cooling efficiency if all the above mentioned investigated variables are increased. Detailed analysis of these figures reveals that there are slight differences if one compares the processing window narrowing for cooling efficiency reduction. In all three cases, increase in these variables leads to reduction of maximum achievable final film thickness but only for die/melt/cooling air temperature increase, slight improvement in the minimum achievable final film thickness can be obtained at specific *BUR*, which can be attributed by complex melt rheology changes caused by complex thermal history. All calculated parameters for these specific analyses are provided in Tabs. 15-17.

Effect of power law index (index of non-Newtonian flow behavior) on the film blowing stability

Predicted effect of the power law index on the film blowing stability is visible in Fig. 49. Based on the data provided in this figure it can be concluded that decrease in the power law index causes widening of the film blowing stability window. Closer analysis of these data led us to the conclusion that the power index increase leads to thinner stable films and vice versa. This conclusion is in good agreement with the experimental work reported by Carreau [27] the order for bubble stability has been found to LDPE (*Mw/Mn* = 5.2 i.e. power law index is low) > LLDPE (*Mw/Mn* = 3.8 i.e. power law is medium) > mLLDPE (*Mw/Mn* = 2.4 i.e. power law is high - closed to 1). All calculated parameters for this specific analysis are provided in Tab. 18.

Effect of activation energy on the film blowing stability

Predicted effect of the power law index on the film blowing stability is visible in Fig. 50. It clearly visible that increase in the flow activation energy leads to slight widening of the film blowing stability window. This conclusion can be supported by the experimental work in [27] where it has been clearly demonstrated that film blowing process is more stable for high flow activation energy LDPE in comparison with low

activation energy LLDPE polymer. All calculated parameters for this specific analysis are provided in Tab. 18.

Effect of Mw on the film blowing stability

The effect of the Mw on the film blowing stability was investigated theoretically by using three virtual materials by using the generalized Newtonian model where model parameters were adjusted with the aim to have different level of η_0, λ (which corresponds with Mw increase) and specific flow viscosity curves as depicted in Fig. 51. The results of the theoretically predicted film blowing stability contours for the fixed processing conditions and all three virtual materials are summarized in Tabs. 20-21 and Fig. 52. It is nicely visible that bubble becomes more stable for Mw increase which is in good correspondence with experimental reality reported in open literature [58]. Note, that in this case, the freezeline height has been fixed and it has been assumed that all bubbles can efficiently cooled down (ideal cooling was assumed). Surprisingly, the non-monotonic trend between Mw increase and the bubble stability has not been found which suggest that cooling efficiency has strong impact on the film blowing stability.

Comparison between experimental and theoretical film blowing stability analysis

With the aim to minimize the problem complexity, ideal cooling efficiency was assumed i.e. it was possible to fix freezeline height for all experiments.

Effect of long chain branching on the film blowing stability

Different type and level of the long chain branching has been theoretically introduced into different virtual materials through the parameters α and ξ in the generalized Newtonian model which leads to the different shape of the strain hardening occurrence in the uniaxial viscosity curve (see Fig. 53 and Fig. 55). Clearly, by comparing the extensional viscosity curves (Fig. 53 and Fig. 55) and corresponding calculated film blowing stability contours (Fig. 54 and Fig. 56) the relationship between level of the strain

hardening (level of LCB) and bubble stability is non-monotonic which indicates that there exists optimum level of the LCB. With the aim to explore this point in more detail (with inclusion of the melt strength), the experimentally determined stability contour lines for linear as well as slightly and highly branched mLLDPEs (see experimental part for more detail) were treated numerically. In more detail, the Newtonian viscosity of the melt has been kept as a constant for all samples in the model whereas melt strength together with generalized Newtonian model parameters (λ, a, n, α, β, ξ) were varied to find out the agreement with the experimentally determined stability contours. Fig. 57 shows the obtained general Newtonian model predictions for linear as well as slightly and highly branched mLLDPEs. The comparison between the measured and fitted stability contours are depicted in Fig. 58. The theoretical results in this Figure shows that continued increase in the melt strength makes the processing window wider, however, the processing window becomes much narrower with increase in level of LCB in mLLDPE beyond the optimum LCB level. Clearly, LCB increases not only melt strength but also melt extensional strain hardening which causes easier stress rise in the film bubble during the processing i.e. at low LCB level the melt strength increase becomes more effective that extensional viscosity increase and the bubble may become more stable. However, if the LCB is increased too much, the strain hardening can become more effective than corresponding melt strength increase which can not longer compensate the corresponding stress rise and the bubble becomes more easily unstable

CONCLUSION

1. It has been shown that the use of the generalized Newtonian model in the non-isothermal modeling of the film blowing process together wit Zatloukal-Vlcek model can be used to investigate the role of processing conditions, machinery design parameters and polymer rheology from the film blowing stability point of view.

2. It has been theoretically revealed that relationship between Newtonian viscosity and film blowing stability has no monotonic character suggesting existence optimum value of Newtonian viscosity (or *Mw*) for needed *BUR* and particular final film thickness.

3. Based on the theoretical stability analysis it has been found that following processing/material changes have stabilizing effect on the film blowing process:

    - Cooling intensity increase
    - Internal bubble decrease
    - Melt strength increase
    - Decrease in the exit temperature (melt temperature leaving the die) or mass flow rate or cooling air temperature
    - Decrease in the index of non-Newtonian flow behavior
    - Flow activation increase

It should be mentioned that all above mentioned theoretical conclusion has been found to be in good agreement with the open literature.

4. It has been shown theoretically, that there is non-monotonic dependence between extensional strain hardening and bubble stability, which has been found to be in good correspondence with experimental data.

Tab. 10. Summarization of the calculated data in the Fig. 41 for Newtonian viscosity effect analysis ($Q = 15.09168 \cdot 10^{-7}\ m^3 \cdot s^{-1}$).

	Point	*BUR* (-)	H_1/H_0 (-)	*L* (m)	Δp (Pa)	*p* (Pa.m)	v_F ($m \cdot s^{-1}$)	*F* (N)	η (kPa·s)	σ_{11} (MPa)	σ_{33} (MPa)
$\eta_0 = 400$ kPa·s	A_1	0.840	0.26198	0.35244	108	12.30	0.06907	254.01	1312.509	11.715815	0.008484
	B_1	1.844	0.39714	0.22925	108	18.91	0.02090	74.51	1024.073	1.032718	0.012286
	C_1	4.130	0.10680	0.12783	108	33.91	0.03486	406.26	1309.566	9.348471	0.102318
		4.130	0.10685	0.12874	1600	498.85	0.05494	423.51	1314.422	9.740942	1.515176
$\eta_0 = 300$ kPa·s	A_2	1.015	0.18089	0.31042	108	13.96	0.08086	230.64	948.318	12.750244	0.014847
	B_2	1.994	0.35281	0.21775	108	19.90	0.02179	70.01	793.404	1.010089	0.014954
	C_2	4.700	0.07949	0.11436	108	37.90	0.04102	328.26	890.399	8.917394	0.156434
		4.700	0.07949	0.11562	1700	590.16	0.06103	360.01	897.443	9.779904	2.463171
$\eta_0 = 200$ kPa·s	A_3	1.400	0.09238	0.27162	108	15.95	0.11835	175.26	566.912	13.754395	0.040099
	B_3	2.253	0.29393	0.20039	108	21.63	0.02314	62.01	542.850	0.950450	0.020282
	C_3	5.400	0.04960	0.10185	108	42.56	0.05720	222.26	487.619	8.421339	0.288020
		5.400	0.04960	0.10233	1550	632.28	0.07652	272.35	515.256	10.319228	4.133625
$\eta_0 = 100$ kPa·s	A_4	2.423	0.07304	0.19173	108	22.61	0.03854	64.19	266.379	3.681370	0.087774
	B_4	2.873	0.19781	0.17268	108	24.83	0.02734	49.95	267.038	0.892116	0.038430
	C_4	5.400	0.04960	0.09853	108	45.35	0.03349	121.68	267.012	4.610405	0.288020
		5.400	0.04960	0.10065	570	241.25	0.03825	109.35	235.365	4.143226	1.520774
$\eta_0 = 50$ kPa·s	A_5	3.412	0.50851	0.14773	108	29.34	0.06765	41.16	94.949	0.240791	0.017754
	B_5	3.720	0.12956	0.13888	108	31.21	0.03223	33.26	116.384	0.700426	0.075970
	C_5	5.400	0.04960	0.07568	108	51.59	0.05059	58.65	110.896	2.222224	0.288020
		5.400	0.04960	0.07056	280	95.36	0.05389	51.23	100.380	1.941083	0.746853

Tab. 11. Summarization of the calculated data in the Fig. 42 for the heat transfer effect analysis ($Q = 15.09168 \cdot 10^{-7}\ m^3 \cdot s^{-1}$).

	Point	*BUR* (-)	H_1/H_0 (-)	*L* (m)	Δp (Pa)	*p* (Pa.m)	v_F ($m \cdot s^{-1}$)	*F* (N)	η (kPa·s)	σ_{11} (MPa)	σ_{33} (MPa)
$h = 70\ Wm^{-2}K^{-1}$	A_1	0.674	0.20206	0.27390	108	11.30	0.11113	191.01	571.949	14.235641	0.008826
	B_1	1.694	0.44831	0.17286	108	17.91	0.02015	41.51	488.648	0.554789	0.009998
	C_1	4.500	0.06882	0.08466	108	36.57	0.04946	255.26	496.773	8.365255	0.172996
		4.500	0.06882	0.08865	2350	643.25	0.09505	289.65	547.911	9.492543	3.765217
$h = 60\ Wm^{-2}K^{-1}$	A_2	0.969	0.13797	0.27593	108	13.09	0.11466	183.76	552.321	13.950553	0.018582
	B_2	1.953	0.36488	0.18395	108	19.63	0.02147	51.51	517.947	0.733683	0.014162
	C_2	5.000	0.05879	0.09054	108	39.90	0.05209	237.89	492.600	8.213719	0.225019
		5.000	0.05879	0.09156	1800	683.56	0.08189	284.56	520.734	9.825614	3.751677
$h = 50\ Wm^{-2}K^{-1}$	A_3	1.400	0.09238	0.27162	108	15.95	0.11835	175.26	566.912	13.754395	0.040099
	B_3	2.253	0.29393	0.20039	108	21.63	0.02314	62.01	542.850	0.950450	0.020282
	C_3	5.400	0.04960	0.10185	108	42.56	0.05720	222.26	487.619	8.421339	0.288020
		5.400	0.04960	0.10233	1550	632.28	0.07652	272.35	515.256	10.319228	4.133625
$h = 40\ Wm^{-2}K^{-1}$	A_4	2.010	0.06156	0.27219	108	19.90	0.12354	163.82	503.359	13.437707	0.086391
	B_4	2.694	0.21299	0.22060	108	24.56	0.02669	80.26	573.630	1.419732	0.033467
	C_4	5.930	0.04031	0.11758	108	46.08	0.06409	204.19	482.332	8.670008	0.389233
		5.930	0.04031	0.11256	988	395.45	0.07032	228.65	523.564	9.708592	3.561594
$h = 30\ Wm^{-2}K^{-1}$	A_5	3.100	0.04042	0.26499	108	27.26	0.12495	153.68	485.213	12.446199	0.202889
	B_5	3.675	0.13916	0.23232	108	31.09	0.02992	94.26	592.092	1.870756	0.069875
	C_5	6.500	0.03200	0.15812	108	53.56	0.06325	201.05	472.564	9.810728	0.537452
		6.500	0.03200	0.14923	680	286.55	0.06854	156.21	605.653	7.622650	3.387191

Tab. 12. Summarization of the calculated data in the Fig. 43 for the internal bubble pressure analysis ($Q = 15.09168 \cdot 10^{-7}\ m^3 \cdot s^{-1}$).

	Point	*BUR* (-)	H_1/H_0 (-)	*L* (m)	Δp (Pa)	*p* (Pa.m)	v_F ($m \cdot s^{-1}$)	*F* (N)	η (kPa·s)	σ_{11} (MPa)	σ_{33} (MPa)
$\Delta p = 50$ Pa	A_1	0.805	0.13000	0.36216	50	5.54	0.14720	159.26	549.711	15.446551	0.007585
	B_1	1.843	0.39843	0.22974	50	8.74	0.02089	34.76	479.320	0.480476	0.005666
	C_1	5.500	0.04922	0.10029	50	20.01	0.05653	219.26	487.649	8.221420	0.136891
		5.500	0.04922	0.09892	292	632.46	0.05985	281.45	502.245	10.553309	0.800402
$\Delta p = 100$ Pa	A_2	1.325	0.09492	0.28038	100	14.32	0.11629	172.07	535.515	13.886618	0.034199
	B_2	2.194	0.30372	0.20411	100	19.66	0.02300	59.26	537.665	0.902651	0.017698
	C_2	5.500	0.04922	0.09877	100	40.64	0.05655	220.89	487.702	8.282539	0.273782
		5.500	0.04922	0.09892	292	632.46	0.05985	281.45	502.245	10.553309	0.800402
$\Delta p = 200$ Pa	A_3	2.000	0.07656	0.21729	200	36.95	0.10262	191.48	508.861	12.692540	0.127999
	B_3	2.694	0.22302	0.17648	200	45.49	0.02551	94.26	580.454	1.592422	0.059190
	C_3	5.500	0.04922	0.10029	200	80.04	0.05642	223.91	488.293	8.395777	0.547564
		5.500	0.04922	0.09892	292	632.46	0.05985	281.45	502.245	10.553309	0.800402
$\Delta p = 300$ Pa	A_4	2.475	0.06880	0.18759	300	64.19	0.09115	203.32	502.222	12.120191	0.264419
	B_4	3.056	0.18240	0.16071	300	74.93	0.02750	121.01	593.673	2.203569	0.123147
	C_4	5.500	0.04922	0.10029	300	120.06	0.05641	227.14	488.539	8.516890	0.821346
		5.500	0.04922	0.09892	292	632.46	0.05985	281.45	502.245	10.553309	0.800402
$\Delta p = 400$ Pa	A_5	2.851	0.06456	0.16932	400	94.82	0.07821	210.19	509.362	11.591838	0.432799
	B_5	3.335	0.15500	0.15182	400	105.76	0.03037	146.01	595.461	2.866991	0.210857
	C_5	5.500	0.04922	0.10029	400	160.08	0.05653	230.26	488.929	8.633878	1.095128
		5.500	0.04922	0.09892	292	632.46	0.05985	281.45	502.245	10.553309	0.800402
$\Delta p = 500$ Pa	A_6	3.181	0.06158	0.15591	500	128.74	0.07661	219.14	499.524	11.354953	0.632780
	B_6	3.594	0.13662	0.14191	500	141.44	0.03120	160.51	592.527	3.318178	0.322267
	C_6	4.859	0.07430	0.09675	500	207.43	0.04180	212.14	497.495	5.964240	0.801103
		4.859	0.07430	0.11119	1200	433.20	0.04331	234.86	538.770	6.603004	1.922679
	D_6	3.750	0.05725	0.12328	500	162.81	0.06773	237.82	471.575	11.243867	0.802402
$\Delta p = 700$ Pa	A_7	3.768	0.08079	0.13671	700	205.52	0.05031	215.76	542.233	7.194457	0.799906
	B_7	4.044	0.11156	0.12924	700	217.41	0.03393	186.51	580.887	4.196316	0.621697
	C_7	4.358	0.09343	0.11328	700	248.04	0.03764	214.14	548.252	5.338014	0.799920
		4.358	0.09343	0.12152	901	296.532	0.05906	211.56	560.164	5.273701	1.029062

Tab. 13. Summarization of the calculated data in the Fig. 44 for the melt strength/melt rupture effect analysis ($Q = 15.09168 \cdot 10^{-7}\ m^3 \cdot s^{-1}$).

	Point	*BUR* (-)	H_1/H_0 (-)	*L* (m)	Δp (Pa)	*p* (Pa.m)	v_F ($m \cdot s^{-1}$)	*F* (N)	η (kPa·s)	σ_{11} (MPa)	σ_{33} (MPa)
σ = 1.00 MPa	A_1	1.430	0.06938	0.26075	108	18.47	0.12469	216.58	482.325	22.159165	0.054541
	B_1	2.253	0.29392	0.20039	108	21.63	0.02314	62.01	542.851	0.950479	0.020282
	C_1	5.600	0.03922	0.01002	108	44.24	0.06452	232.85	442.328	10.761600	0.377827
		5.600	0.03922	0.01054	1301	395.23	0.08561	290.89	499.356	13.444028	4.549906
σ = 0.80 MPa	A_2	1.400	0.09238	0.27162	108	15.96	0.11836	175.26	566.912	13.754395	0.040099
	B_2	2.253	0.29392	0.20039	108	21.63	0.02314	62.01	542.851	0.950479	0.020282
	C_2	5.400	0.04961	0.10185	108	42.56	0.05721	222.26	487.619	8.421339	0.288020
		5.400	0.04961	0.10165	1161	421.79	0.08164	310.54	560.412	11.766232	3.095045
σ = 0.60 MPa	A_3	1.380	0.12600	0.27162	108	15.96	0.08702	162.89	568.942	9.508801	0.028980
	B_3	2.253	0.29392	0.20039	108	21.63	0.02314	62.01	542.851	0.950479	0.020282
	C_3	5.048	0.06580	0.10753	108	40.26	0.04613	212.42	525.452	6.490893	0.202985
		5.048	0.06580	0.10751	1050	412.92	0.07524	320.51	523.752	9.793786	1.974065
σ = 0.40 MPa	A_4	1.430	0.17730	0.26624	108	16.26	0.06059	139.68	594.250	5.592048	0.021341
	B_4	2.253	0.29392	0.20039	108	21.63	0.02314	62.01	542.851	0.950479	0.020282
	C_4	4.348	0.09583	0.12181	108	35.51	0.03675	189.76	568.005	4.622856	0.120061
		4.348	0.09583	0.12184	901	296.47	0.06574	212.89	559.055	5.186340	1.001072
σ = 0.20 MPa	A_5	1.655	0.25450	0.24613	108	17.56	0.03642	101.56	582.458	2.447434	0.017207
	B_5	2.253	0.29392	0.20039	108	21.63	0.02314	62.01	542.851	0.950479	0.020282
	C_5	3.150	0.17054	0.15708	108	27.60	0.02851	128.01	595.425	2.418667	0.048873
		3.150	0.17054	0.15591	500	128.74	0.03561	219.12	499.524	4.140132	0.226273
σ = 0.15 MPa	A_6	1.430	0.06938	0.27054	108	16.03	0.03305	81.34	555.321	8.322220	0.054541
	B_6	2.253	0.29392	0.20039	108	21.63	0.02314	62.01	542.851	0.950479	0.020282
	C_6	2.749	0.21164	0.19954	108	21.69	0.02825	95.82	578.852	1.671729	0.034370
		2.749	0.21164	0.17384	220	50.80	0.03024	101.51	585.165	1.771000	0.070079

Tab. 14. Summarization of the calculated data in the Fig. 45 for the die radius effect analysis ($Q = 15.09168 \cdot 10^{-7}\ m^3 \cdot s^{-1}$).

	Point	BUR (-)	H_1/H_0 (-)	L (m)	Δp (Pa)	p (Pa.m)	v_F ($m \cdot s^{-1}$)	F (N)	η (kPa·s)	σ_{11} (MPa)	σ_{33} (MPa)
$R_o = 0.035$ m	A_1	0.274	0.29500	0.28081	108	15.44	0.10433	246.26	587.077	30.923979	0.002458
	B_1	1.494	0.54501	0.14639	108	29.61	0.01053	29.01	396.997	0.361635	0.007253
	C_1	3.500	0.06152	0.08112	108	53.44	0.03987	299.32	518.825	14.109261	0.150529
		3.500	0.06152	0.08123	2401	982.37	0.05555	388.21	654.064	18.299332	3.345815
$R_o = 0.030$ m	A_2	0.500	0.18250	0.28393	108	15.27	0.10676	228.32	569.842	25.397160	0.007249
	B_2	1.653	0.46798	0.16052	108	27.01	0.01294	37.51	439.746	0.492172	0.009346
	C_2	4.000	0.05781	0.08518	108	50.89	0.04330	272.89	511.848	11.977983	0.183076
		4.000	0.05781	0.08551	2210	1020.56	0.04756	300.58	576.860	13.193383	3.746366
$R_o = 0.025$ m	A_3	0.840	0.12600	0.27564	108	15.86	0.11234	204.54	547.521	19.615485	0.017640
	B_3	1.881	0.38536	0.17738	108	24.44	0.01656	48.01	487.652	0.672284	0.012916
	C_3	4.600	0.05391	0.09126	108	47.50	0.04847	248.63	501.970	10.177302	0.225793
		4.600	0.05391	0.09052	2601	1010.52	0.04805	269.56	560.984	11.034041	5.437577
$R_o = 0.020$ m	A_4	1.400	0.09238	0.27162	108	15.96	0.11836	175.26	566.912	13.754395	0.040099
	B_4	2.253	0.29393	0.20039	108	21.63	0.02314	62.01	542.850	0.950450	0.020282
	C_4	5.400	0.04961	0.10185	108	42.56	0.05721	222.26	487.619	8.421339	0.288020
		5.400	0.04961	0.10233	1550	632.29	0.06952	272.35	515.256	10.319228	4.134825
$R_o = 0.015$ m	A_5	2.200	0.07688	0.26618	108	16.28	0.11832	148.89	516.969	8.935766	0.075723
	B_5	2.869	0.20422	0.22018	108	19.69	0.03419	80.01	587.483	1.386097	0.037173
	C_5	5.800	0.05078	0.22035	108	37.56	0.03419	203.64	525.374	7.017912	0.302215
		5.800	0.05078	0.14230	590	175.66	0.04985	172.35	546.876	5.939585	1.651131

Tab. 15. Summarization of the calculated data in the Fig. 46 for the mass flow rate effect analysis.

	Point	*BUR* (-)	H_1/H_0 (-)	*L* (m)	Δp (Pa)	*p* (Pa.m)	v_F ($m \cdot s^{-1}$)	*F* (N)	η (kPa·s)	σ_{11} (MPa)	σ_{33} (MPa)
$m = 3.6\ kg \cdot h^{-1}$	A_1	1.400	0.09238	0.27162	108	15.96	0.11836	175.26	566.912	13.754395	0.040099
	B_1	2.253	0.29393	0.20039	108	21.63	0.02314	62.01	542.850	0.950450	0.020282
	C_1	5.400	0.04961	0.10185	108	42.56	0.05721	222.26	487.619	8.421339	0.288020
		5.400	0.04961	0.10233	1550	632.28	0.09652	272.35	515.256	10.319228	4.133625
$m = 5.4\ kg \cdot h^{-1}$	A_2	1.875	0.07930	0.29152	108	19.12	0.13246	187.51	515.739	12.800899	0.062565
	B_2	2.594	0.23500	0.23322	108	23.90	0.03231	88.01	575.266	1.465441	0.029207
	C_2	5.900	0.04766	0.12147	108	45.88	0.07003	237.51	480.745	8.574057	0.327585
		5.900	0.04766	0.12356	1151	890.56	0.09017	248.65	510.499	8.976209	3.490147
$m = 7.2\ kg \cdot h^{-1}$	A_3	2.550	0.06754	0.31479	108	23.61	0.15497	205.63	498.947	12.118612	0.099899
	B_3	3.093	0.17625	0.27298	108	27.23	0.04812	125.51	594.760	2.336917	0.046434
	C_3	6.100	0.04675	0.15664	108	55.65	0.09292	275.69	458.965	9.812170	0.345239
		6.100	0.04675	0.15594	981	634.56	0.11052	350.21	515.448	12.464435	3.134799
$m = 9\ kg \cdot h^{-1}$	A_4	3.180	0.06100	0.33458	108	27.77	0.15832	219.14	502.611	11.466709	0.137939
	B_4	3.593	0.13802	0.30408	108	30.55	0.06614	159.51	592.714	3.264823	0.068881
	C_4	6.400	0.04605	0.18564	108	56.49	0.10585	305.65	495.654	10.526618	0.367739
		6.400	0.04605	0.18456	580	298.63	0.12577	310.56	500.156	10.695719	1.975067
$m = 10.8\ kg \cdot h^{-1}$	A_5	3.800	0.05703	0.34922	108	31.92	0.20123	238.95	468.938	11.191454	0.176304
	B_5	4.163	0.11500	0.32470	108	34.33	0.08234	185.14	582.274	3.925275	0.095785
	C_5	6.700	0.45300	0.21546	108	80.56	0.09556	326.48	434.564	1.091837	0.039135
		6.700	0.45300	0.21464	331	105.57	0.09856	220.54	561.564	0.737545	0.119779

Tab. 16. Summarization of the calculated data in the Fig. 47 for the die /melt temperature effect analysis ($Q = 15.09168 \cdot 10^{-7}\ m^3 \cdot s^{-1}$).

	Point	*BUR* (-)	H_1/H_0 (-)	*L* (m)	Δp (Pa)	*p* (Pa.m)	v_F ($m \cdot s^{-1}$)	*F* (N)	η (kPa·s)	σ_{11} (MPa)	σ_{33} (MPa)
T_{die} = 175 °C	A_1	1.400	0.09238	0.27162	108	15.96	0.11836	175.26	566.912	13.754395	0.040099
	B_1	2.253	0.29393	0.20039	108	21.63	0.02314	62.01	542.850	0.950450	0.020282
	C_1	5.400	0.04961	0.10185	108	42.56	0.05721	222.26	487.619	8.421339	0.288020
		5.400	0.04961	0.10233	1550	632.29	0.06652	272.35	515.256	10.319228	4.133625
T_{die} = 195 °C	A_2	1.850	0.06700	0.26937	108	18.79	0.12695	90.52	482.701	7.412626	0.073061
	B_2	2.568	0.23781	0.21323	108	23.73	0.02544	34.51	559.673	0.573573	0.028573
	C_2	5.300	0.04370	0.12145	108	42.24	0.06705	111.45	472.365	4.884238	0.320911
		5.300	0.04370	0.12254	701	680.53	0.06957	280.46	515.654	12.291014	2.083097
T_{die} = 215 °C	A_3	2.230	0.05000	0.23505	108	21.44	0.13739	45.18	492.564	4.112710	0.118007
	B_3	2.850	0.20035	0.22283	108	25.60	0.02758	19.89	571.048	0.353566	0.037639
	C_3	5.200	0.03984	0.13837	108	41.23	0.07604	58.68	460.106	2.874736	0.345327
		5.200	0.03984	0.13646	651	690.56	0.07806	295.66	555.631	14.484395	2.080146
T_{die} = 235 °C	A_4	2.550	0.04605	0.27323	108	23.11	0.13045	25.12	552.628	2.171320	0.146521
	B_4	3.050	0.17154	0.23336	108	26.93	0.03055	12.79	582.020	0.248136	0.047047
	C_4	4.950	0.03816	0.16051	108	41.57	0.08106	35.56	450.105	1.910631	0.343195
		4.950	0.03816	0.16245	426	125.99	0.08212	150.64	525.325	8.093853	1.352602
T_{die} = 255 °C	A_5	2.865	0.04100	0.27092	108	25.14	0.13041	13.87	564.261	1.198511	0.184897
	B_5	3.231	0.14901	0.24211	108	28.15	0.03364	8.64	589.516	0.182153	0.057374
	C_5	4.640	0.03598	0.15154	108	44.95	0.09175	20.67	447.544	1.256571	0.341192
		4.640	0.03598	0.16546	261	98.54	0.08505	19.85	550.681	1.206722	0.822967

Tab. 17. Summarization of the calculated data in the Fig. 48 for the cooling air temperature effect analysis ($Q = 15.09168 \cdot 10^{-7}\ m^3 \cdot s^{-1}$).

	Point	*BUR* (-)	H_1/H_0 (-)	*L* (m)	*Δp* (Pa)	*p* (Pa.m)	v_F ($m \cdot s^{-1}$)	*F* (N)	*η* (kPa·s)	σ_{11} (MPa)	σ_{33} (MPa)
T_{air} = 10 °C	A_1	1.100	0.12156	0.27043	108	13.97	0.11456	178.89	545.077	13.578945	0.023943
	B_1	1.994	0.35240	0.18969	108	19.91	0.02182	53.01	522.537	0.765730	0.014972
	C_1	5.000	0.05703	0.09465	108	39.90	0.05371	231.26	493.280	8.231777	0.231979
		5.000	0.05703	0.09564	1651	480.65	0.05951	280.56	523.560	9.986627	3.545414
T_{air} = 25 °C	A_2	1.400	0.09238	0.27162	108	15.96	0.11836	175.26	566.912	13.754395	0.040099
	B_2	2.253	0.29393	0.20039	108	21.63	0.02314	62.01	542.850	0.950450	0.020282
	C_2	5.400	0.04961	0.10185	108	42.56	0.05721	222.26	487.619	8.421339	0.288020
		5.400	0.04961	0.10233	1550	632.28	0.07652	272.35	515.256	10.319228	4.133625
T_{air} = 40 °C	A_3	1.850	0.06853	0.26545	108	19.52	0.11259	172.56	509.632	13.815144	0.071429
	B_3	2.594	0.23432	0.21340	108	23.90	0.02519	74.51	564.407	1.244239	0.029292
	C_3	5.900	0.04219	0.11114	108	45.88	0.06154	212.51	481.278	8.665877	0.370044
		5.900	0.04219	0.11235	1290	458.96	0.04953	198.45	512.354	8.092528	4.418698
T_{air} = 55 °C	A_4	2.512	0.05055	0.25464	108	23.56	0.12565	170.56	478.062	13.634137	0.131494
	B_4	3.153	0.17525	0.22536	108	27.62	0.02772	88.51	583.048	1.625865	0.047605
	C_4	6.600	0.03458	0.12154	108	50.46	0.07055	203.54	470.812	9.052740	0.505049
		6.600	0.03458	0.12589	854	367.65	0.05966	275.65	525.459	12.259938	3.995783
T_{air} = 70 °C	A_5	3.640	0.03271	0.26054	108	30.90	0.12868	170.5	497.883	14.537272	0.294494
	B_5	4.093	0.11701	0.23883	108	33.88	0.03197	107.51	595.224	2.278646	0.092561
	C_5	7.200	0.02500	0.15546	108	55.23	0.08510	198.53	459.564	11.194645	0.762018
		7.200	0.02500	0.14567	497	238.24	0.05642	212.56	545.489	11.985764	3.503587

Tab. 18. Summarization of the calculated data in the Fig. 49 for power law index effect analysis ($Q = 15.09168 \cdot 10^{-7}\ m^3 \cdot s^{-1}$).

	Point	*BUR* (-)	H_1/H_0 (-)	*L* (m)	Δp (Pa)	*p* (Pa.m)	v_F ($m \cdot s^{-1}$)	*F* (N)	η (kPa·s)	σ_{11} (MPa)	σ_{33} (MPa)
n = 0.7	A_1	0.990	0.19000	0.32545	108	13.22	0.08117	235.51	985.454	12.708443	0.013787
	B_1	2.156	0.31429	0.20653	108	20.99	0.02262	67.51	648.929	1.011250	0.018151
	C_1	4.351	0.09479	0.10448	108	35.16	0.03746	405.15	1150.564	9.970991	0.121455
		4.351	0.09479	0.11564	1481	380.65	0.03315	450.56	954.564	11.088559	1.665107
n = 0.6	A_2	1.060	0.16700	0.31644	108	13.76	0.08714	220.51	883.231	12.643870	0.016795
	B_2	2.150	0.31198	0.20694	108	20.95	0.02279	65.51	616.775	0.991313	0.018235
	C_2	4.650	0.08262	0.11545	108	37.56	0.03961	340.40	946.445	8.993759	0.148927
		4.650	0.08262	0.11509	1851	645.24	0.04094	388.26	950.974	10.258275	2.551836
n = 0.5	A_3	1.148	0.14100	0.30466	108	14.29	0.09447	207.50	764.812	13.011614	0.021543
	B_3	2.194	0.30557	0.20411	108	21.24	0.02283	63.51	587.776	0.961534	0.018998
	C_3	4.950	0.07073	0.10554	108	39.61	0.04376	299.39	769.361	8.680024	0.185187
		4.950	0.07073	0.10945	1860	680.45	0.04756	356.45	769.576	10.334328	3.188572
n = 0.4	A_4	1.281	0.11200	0.28564	108	15.13	0.10812	189.55	624.952	13.410060	0.030264
	B_4	2.275	0.28990	0.19905	108	21.78	0.02322	64.01	562.774	0.985141	0.020765
	C_4	5.318	0.05750	0.10347	108	41.90	0.05029	252.14	592.464	8.369503	0.244720
		5.318	0.05750	0.10246	1655	553.99	0.05506	295.35	605.654	9.803810	3.749118
n = 0.3	A_5	1.480	0.07964	0.26075	108	16.62	0.13025	162.79	453.815	14.019087	0.049174
	B_5	2.294	0.28610	0.19792	108	21.90	0.02332	62.51	531.969	0.966763	0.021216
	C_5	5.700	0.04349	0.09956	108	49.57	0.03657	198.62	417.710	8.133037	0.346813
		5.700	0.04349	0.09856	1701	620.47	0.05642	320.56	505.131	13.126203	5.460890

Tab. 19. Summarization of the calculated data in the Fig. 50 for the flow activation effect analysis ($Q = 15.09168 \cdot 10^{-7}\ m^3 \cdot s^{-1}$).

	Point	BUR (-)	H_1/H_0 (-)	L (m)	Δp (Pa)	p (Pa.m)	v_F ($m \cdot s^{-1}$)	F (N)	η (kPa·s)	σ_{11} (MPa)	σ_{33} (MPa)
$E_A = 75\ kJ mol^{-1}$	A_1	1.410	0.08900	0.27162	108	15.96	0.12180	208.76	509.964	16.885435	0.041920
	B_1	2.269	0.29110	0.19943	108	21.73	0.02320	66.01	540.202	1.014395	0.020624
	C_1	5.600	0.04843	0.09877	108	43.88	0.05648	252.26	481.130	9.441043	0.305959
		5.600	0.04843	0.10054	1225	582.32	0.04532	286.54	512.235	10.724001	3.470370
$E_A = 60\ kJ mol^{-1}$	A_2	1.382	0.09316	0.27162	108	15.96	0.11620	154.82	538.060	12.205726	0.039253
	B_2	2.289	0.28685	0.19819	108	21.87	0.02331	61.51	549.172	0.950866	0.021114
	C_2	5.400	0.05039	0.10186	108	42.56	0.05627	201.14	495.848	7.502991	0.283556
		5.400	0.05039	0.10345	1450	523.56	0.04694	228.45	512.566	8.521717	3.807005
$E_A = 45\ kJ mol^{-1}$	A_3	1.347	0.09936	0.27564	108	15.75	0.12066	110.56	563.463	8.384804	0.035871
	B_3	2.241	0.29505	0.20116	108	21.55	0.02319	48.89	547.028	0.750510	0.020097
	C_3	5.100	0.05310	0.10686	108	40.56	0.05655	155.19	520.022	5.816652	0.254136
		5.100	0.05310	0.10584	1520	562.54	0.00534	192.15	532.045	7.201944	3.576723
$E_A = 30\ kJ mol^{-1}$	A_4	1.332	0.10300	0.28343	108	15.29	0.11253	72.32	583.941	5.350459	0.034218
	B_4	2.253	0.29203	0.20038	108	21.63	0.02327	33.32	535.878	0.514032	0.020414
	C_4	4.700	0.05703	0.11436	108	37.90	0.05712	114.89	547.310	4.350659	0.218064
		4.700	0.05703	0.11354	1220	418.56	0.04846	131.56	565.256	4.981920	2.463318
$E_A = 15\ kJ mol^{-1}$	A_5	1.325	0.10500	0.28343	108	15.29	0.11090	45.51	593.072	3.320288	0.033390
	B_5	2.281	0.28622	0.19897	108	21.82	0.02345	21.66	522.162	0.336750	0.021087
	C_5	4.544	0.60004	0.11853	108	36.57	0.05699	80.45	570.733	0.299489	0.020038
		4.544	0.60004	0.11759	1220	416.47	0.05522	98.29	579.312	0.365902	0.226352

Tab. 20. Zatloukal-Vlcek film blowing model parameters including Newtonian viscosity, η_0, for generalized Newtonian constitutive equation.

	η_0 (kPa·s)	L (m)	Q ($m^3 \cdot s^{-1}$)	p (Pa·m)	σ (MPa)	H_0 (m)	R_0 (m)
Fig. 57-58	100	0.18	$43.40 \cdot 10^{-7}$	50	0.3 1.9 2.5	$1.34 \cdot 10^{-3}$	0.037
Fig. 53-56	100	0.18	$43.40 \cdot 10^{-7}$	111.163	1	$1.34 \cdot 10^{-3}$	0.037
Fig. 51-52	2449103 244910.3 24491.03	0.18	$43.40 \cdot 10^{-7}$	111.163	1	$1.34 \cdot 10^{-3}$	0.037

Tab. 21. Parameters of the generalized Newtonian constitutive equation.

	β (-)	λ (s)	ξ (-)	a (-)	n (-)	α (s)
Fig. 57-58	1	0.23591	0.565997	0.76966	0.28329	0 0.2 1
Fig. 53-54	1	0.23591	0.0 0.2 0.4 0.6 0.8	0.76966	0.28329	0.5
Fig. 55-56	1	0.23591	0.565997	0.76966	0.28329	0 0.1 0.5 1 1.5
Fig. 51-52	**1**	77.4 2.58 0.086	0	0.41	0.28329	0

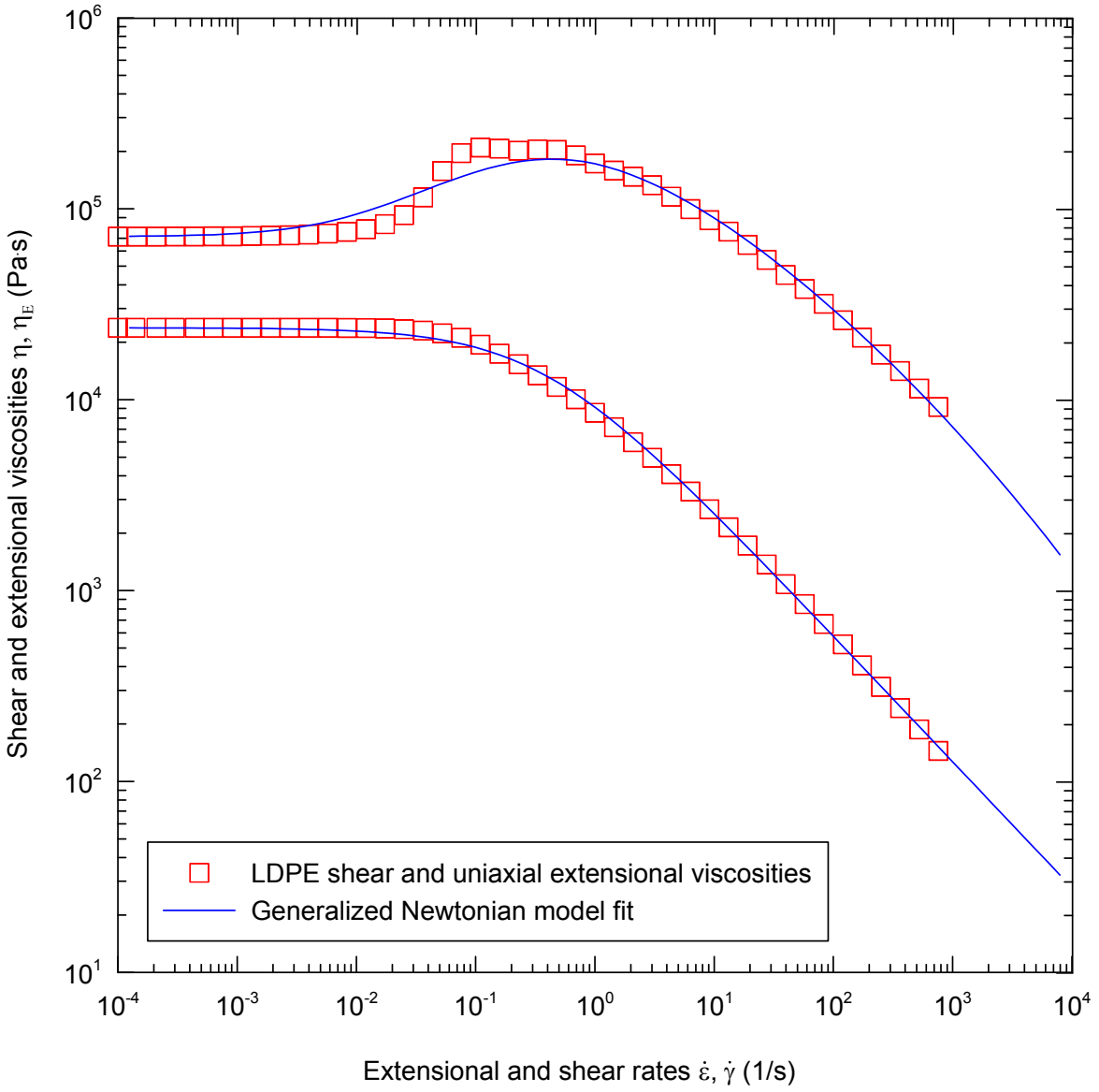

Fig. 36. Comparison between generalized Newtonian model fitting lines and experimental data for LDPE material taken from Tas's Ph.D. thesis [1].

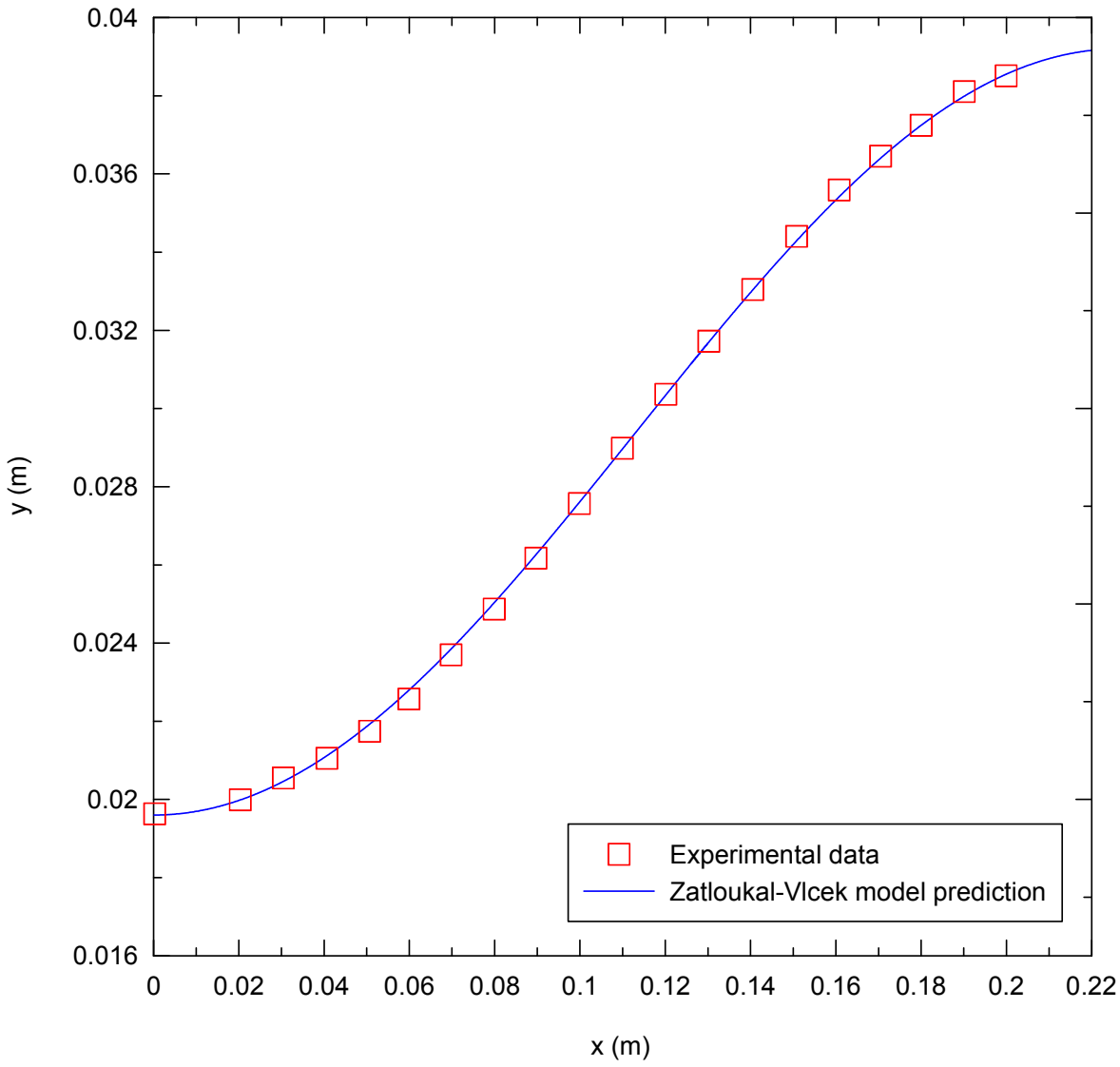

Fig. 37. Comparison between Zatloukal-Vlcek model predictions and experimental data for the LDPE bubble shape taken from Tas's Ph.D. thesis [1].

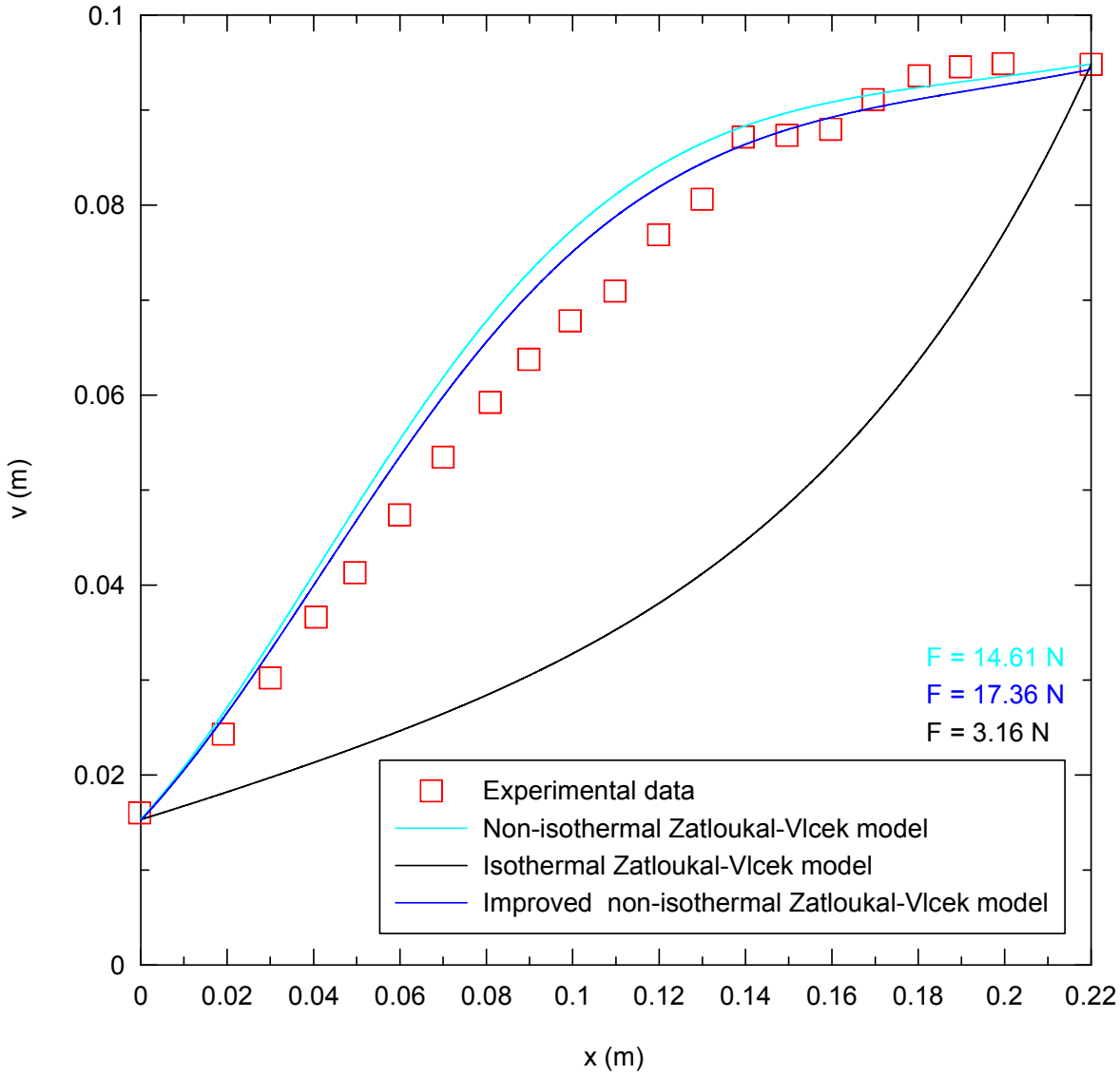

Fig. 38. Comparison between non-Newtonian Zatloukal-Vlcek model predictions and experimental data for the LDPE bubble velocity taken from Tas's Ph.D. thesis [1].

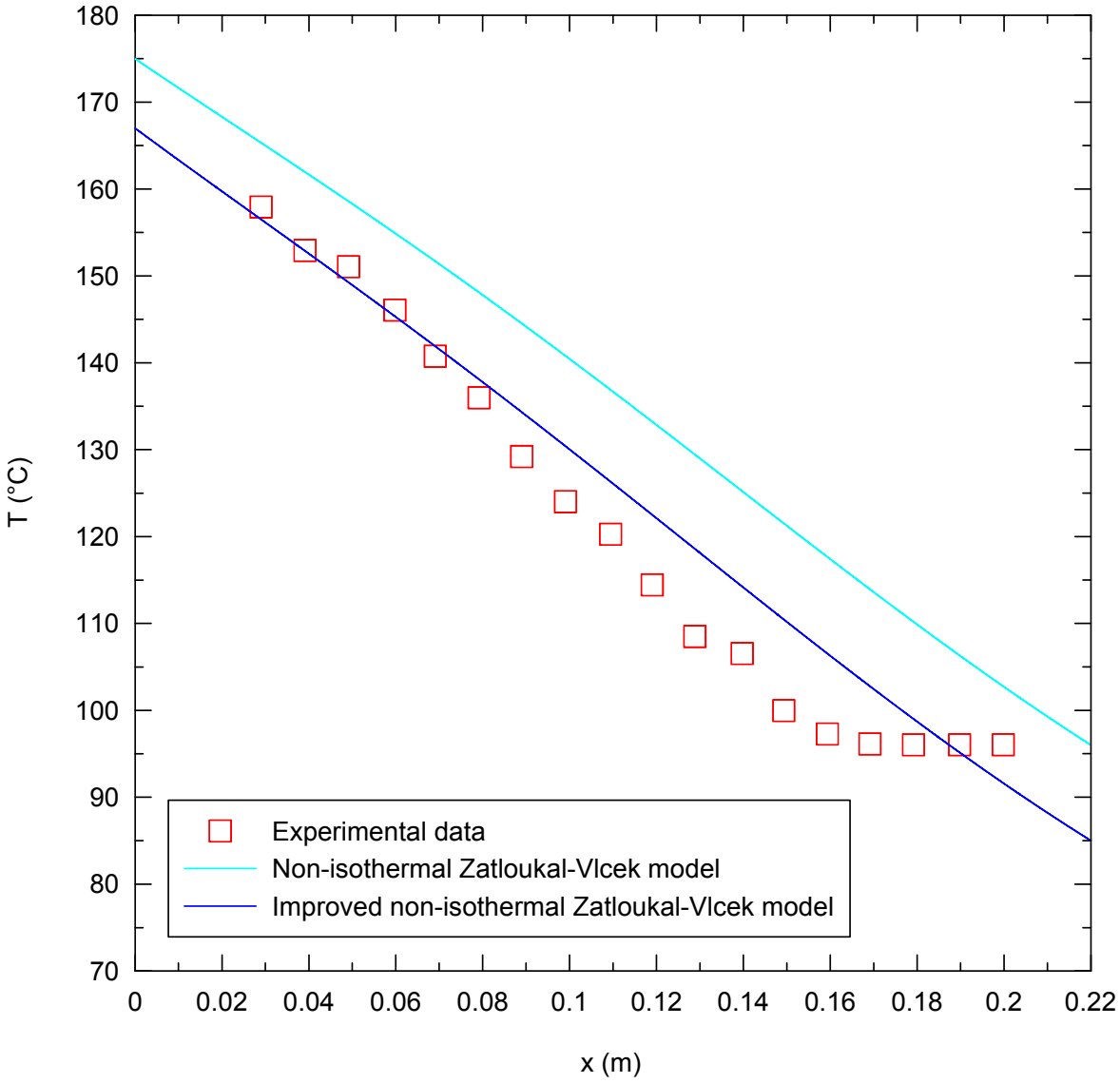

Fig. 39. Comparison between non-Newtonian Zatloukal-Vlcek model predictions and experimental data for the LDPE bubble temperature taken from Tas's Ph.D. thesis [1].

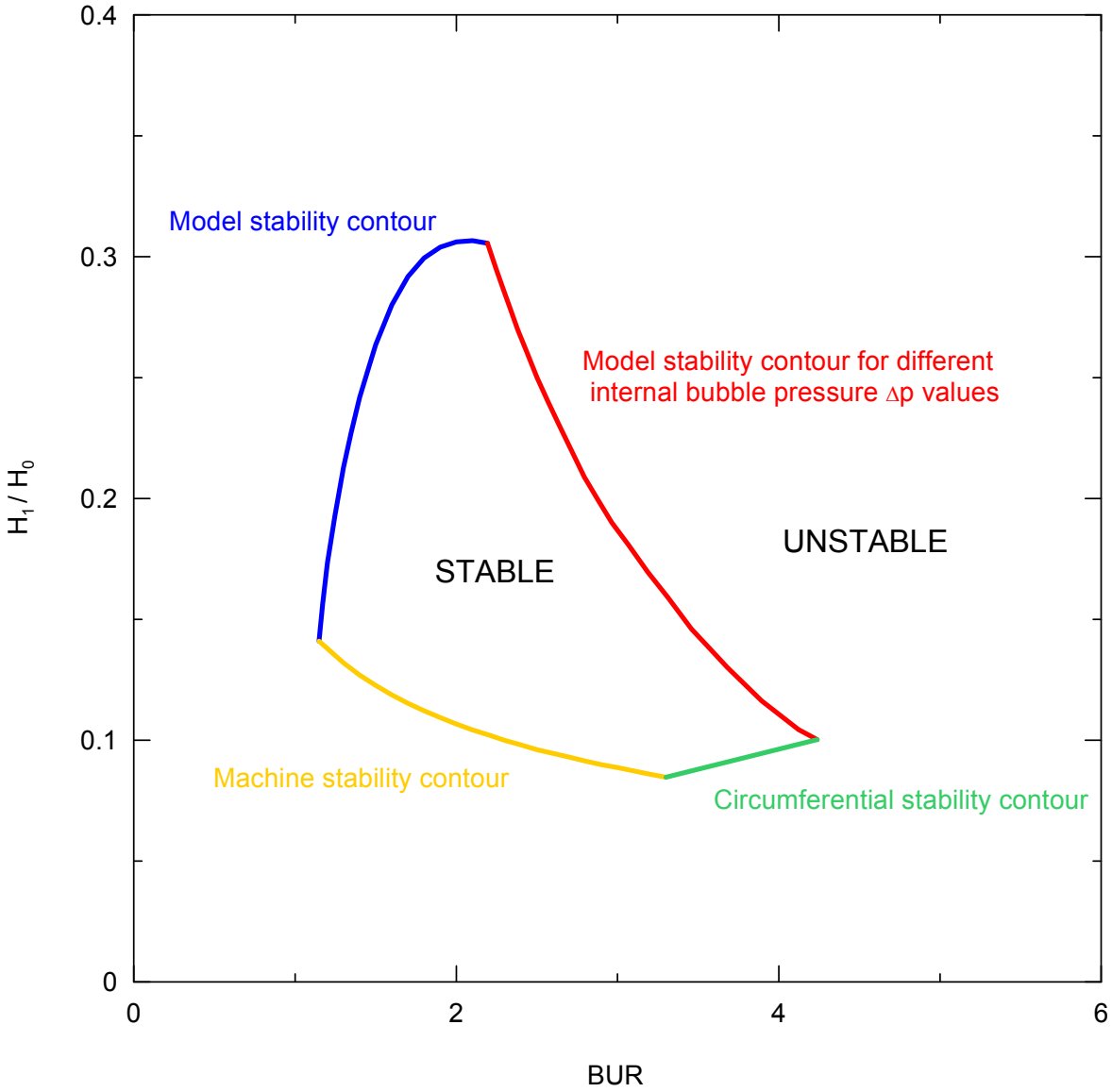

Fig. 40. Typical processing window predicted by the Zatloukal-Vlcek model for non-isothermal processing conditions and non-Newtonian polymer melt.

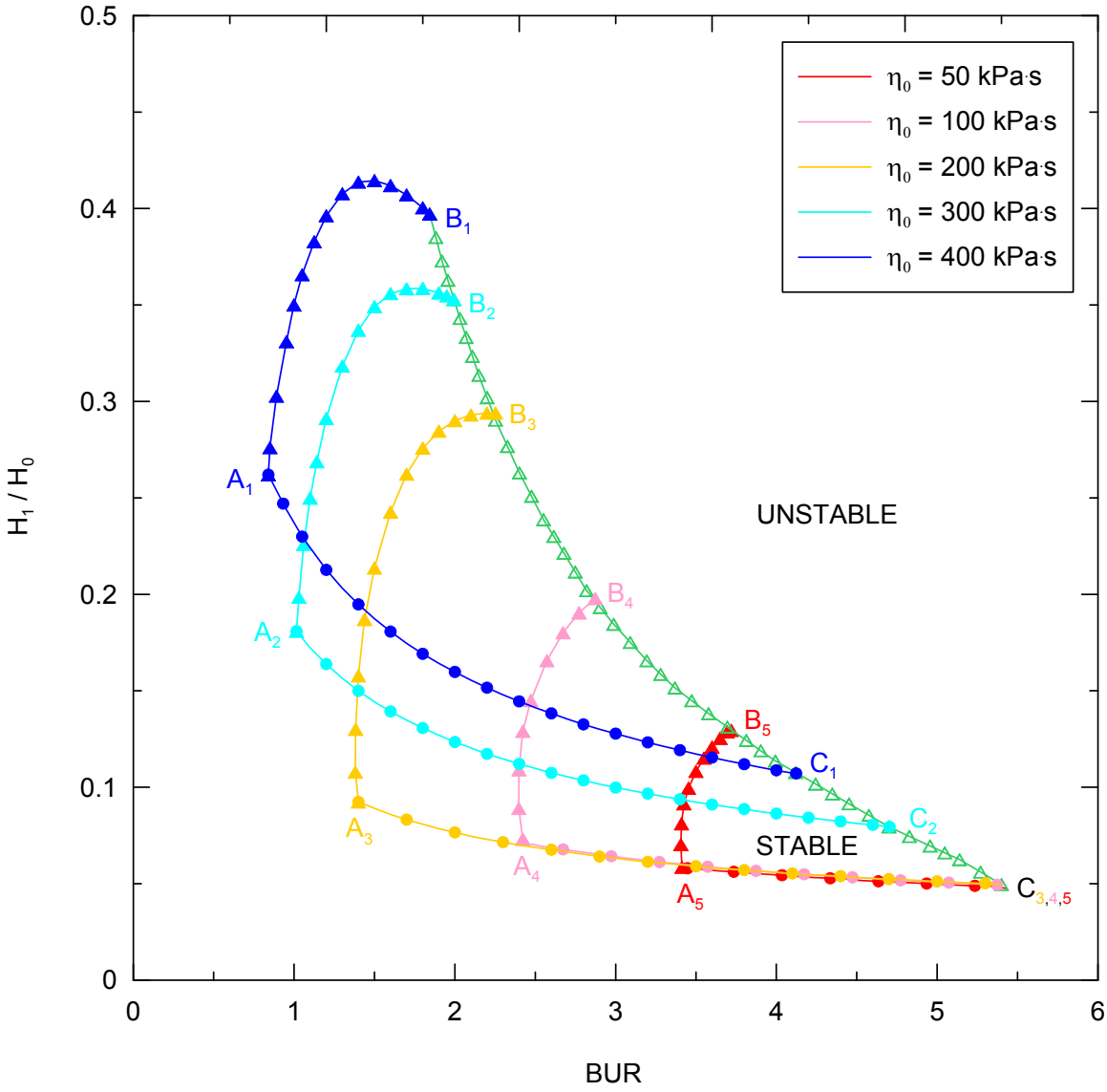

Fig. 41. Stability contours for different level of the Newtonian viscosity predicted by the Zatloukal-Vlcek model for non-isothermal processing conditions and non-Newtonian polymer melt. Model and machine stability contours are represented by triangles and circles, respectively.

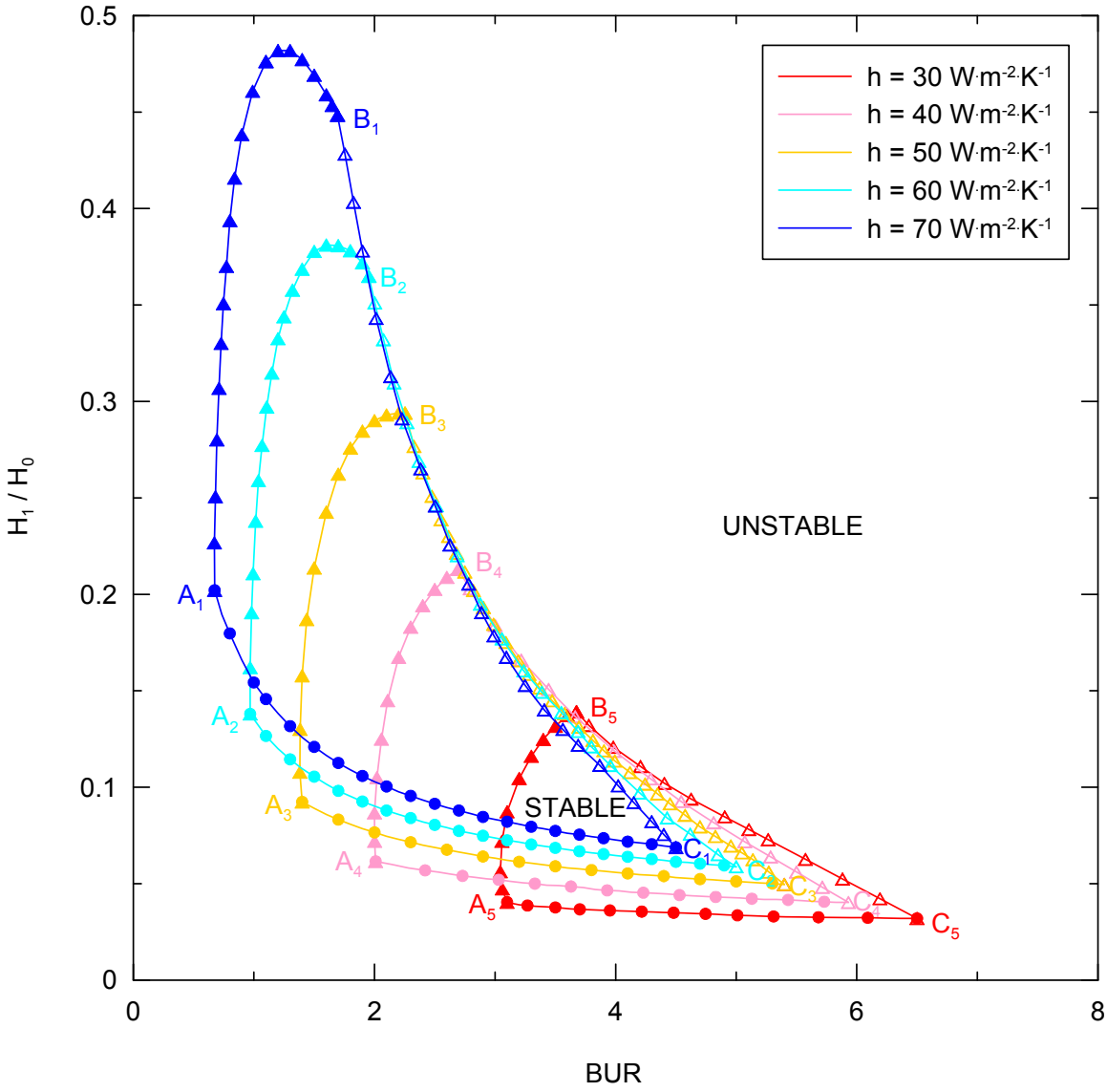

Fig. 42. Stability contours for different level of the heat transfer coefficient predicted by the Zatloukal-Vlcek model for non-isothermal processing conditions and non-Newtonian polymer melt. Model and machine stability contours are represented by triangles and circles, respectively.

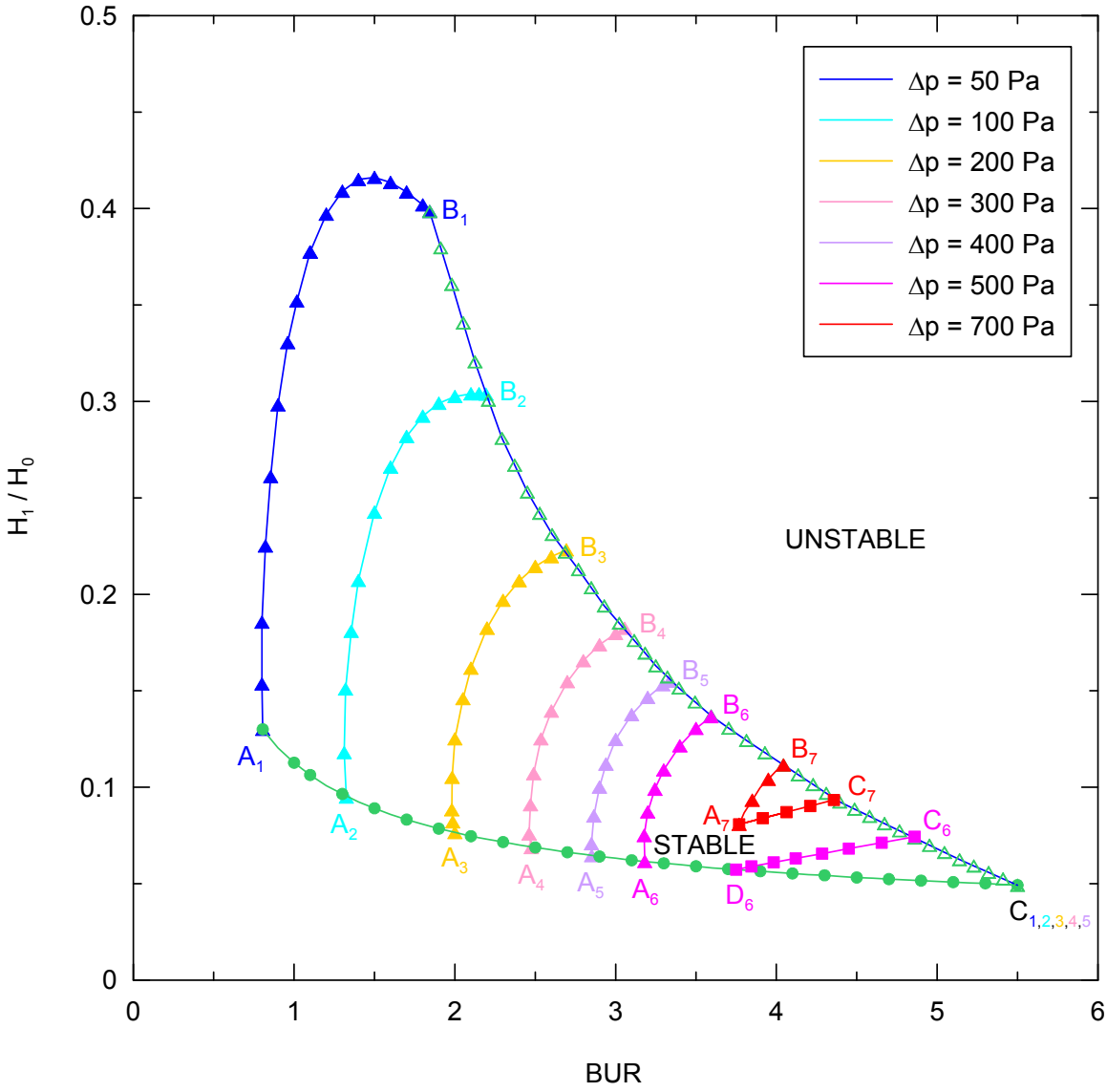

Fig. 43. Stability contours for different level of the internal bubble pressure predicted by the Zatloukal-Vlcek model for non-isothermal processing conditions and non-Newtonian polymer melt. Model, machine and circumference stability contours are represented by triangles, circles and squares, respectively.

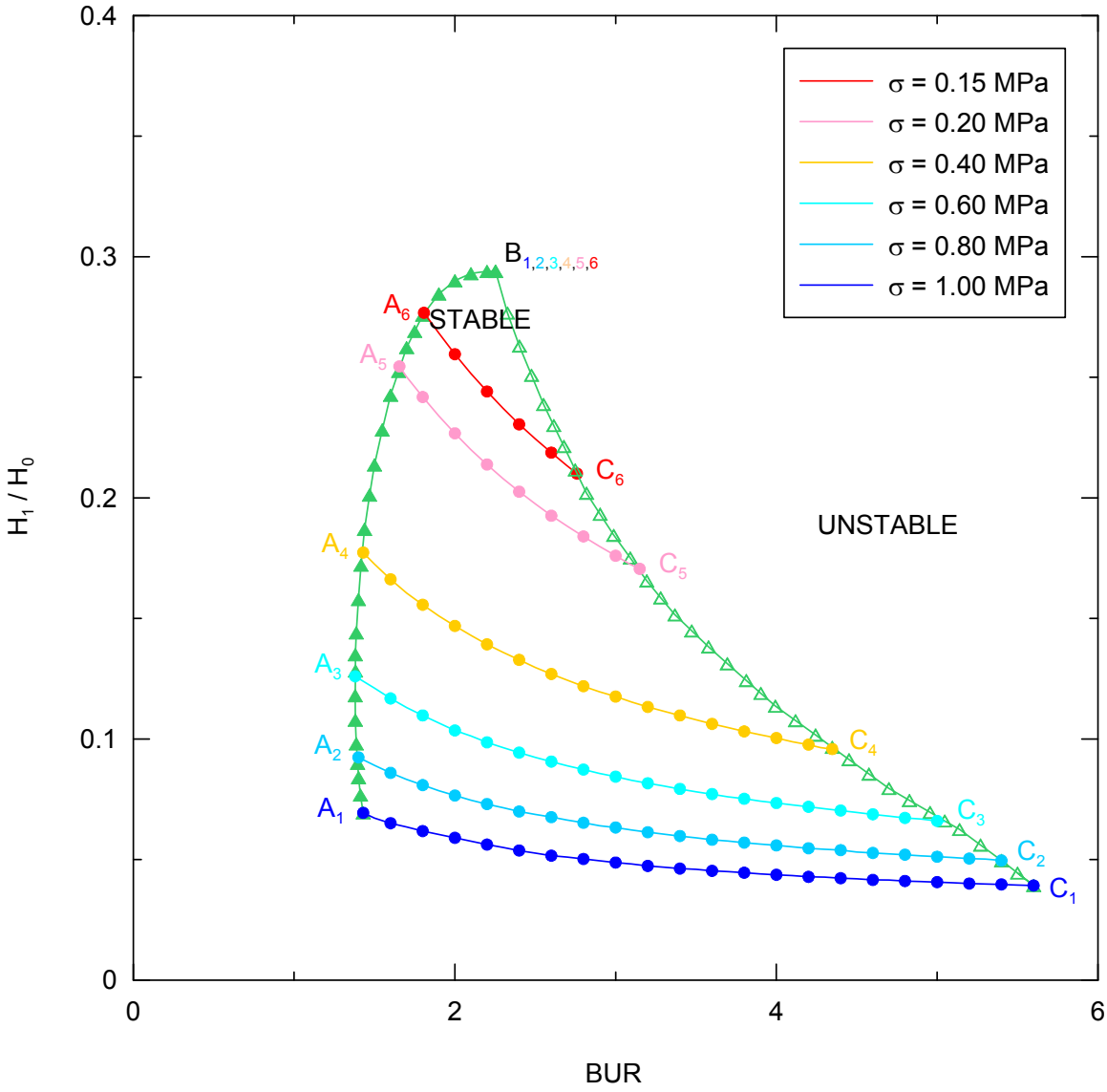

Fig. 44. *Stability contours for different level of the rupture stress predicted by the Zatloukal-Vlcek model for non-isothermal processing conditions and non-Newtonian polymer melt. Model and machine stability contours are represented by triangles and circles, respectively.*

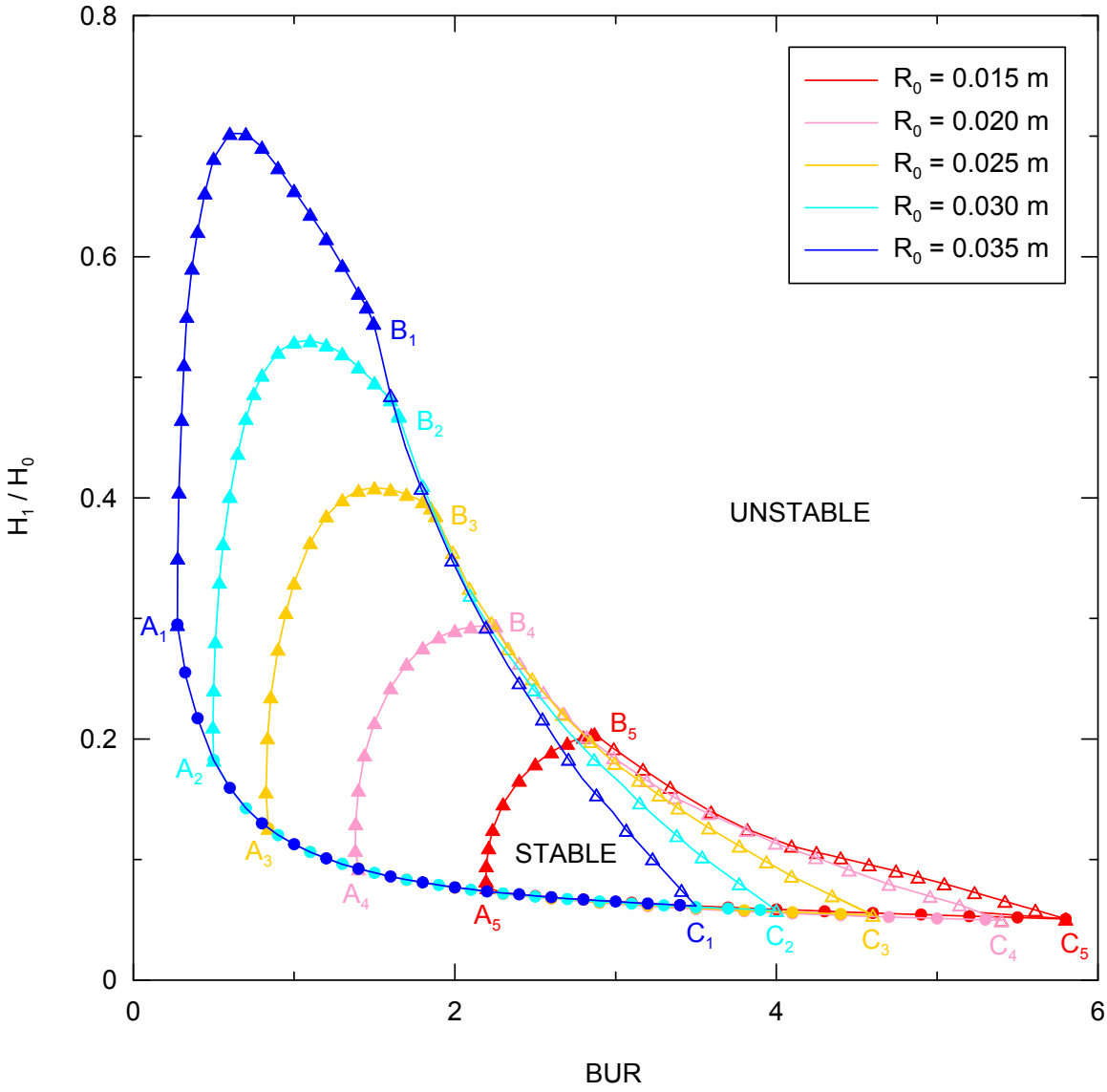

Fig. 45. *Stability contours for different level of the die radius predicted by the Zatloukal-Vlcek model for non-isothermal processing conditions and non-Newtonian polymer melt. Model and machine stability contours are represented by triangles and circles, respectively.*

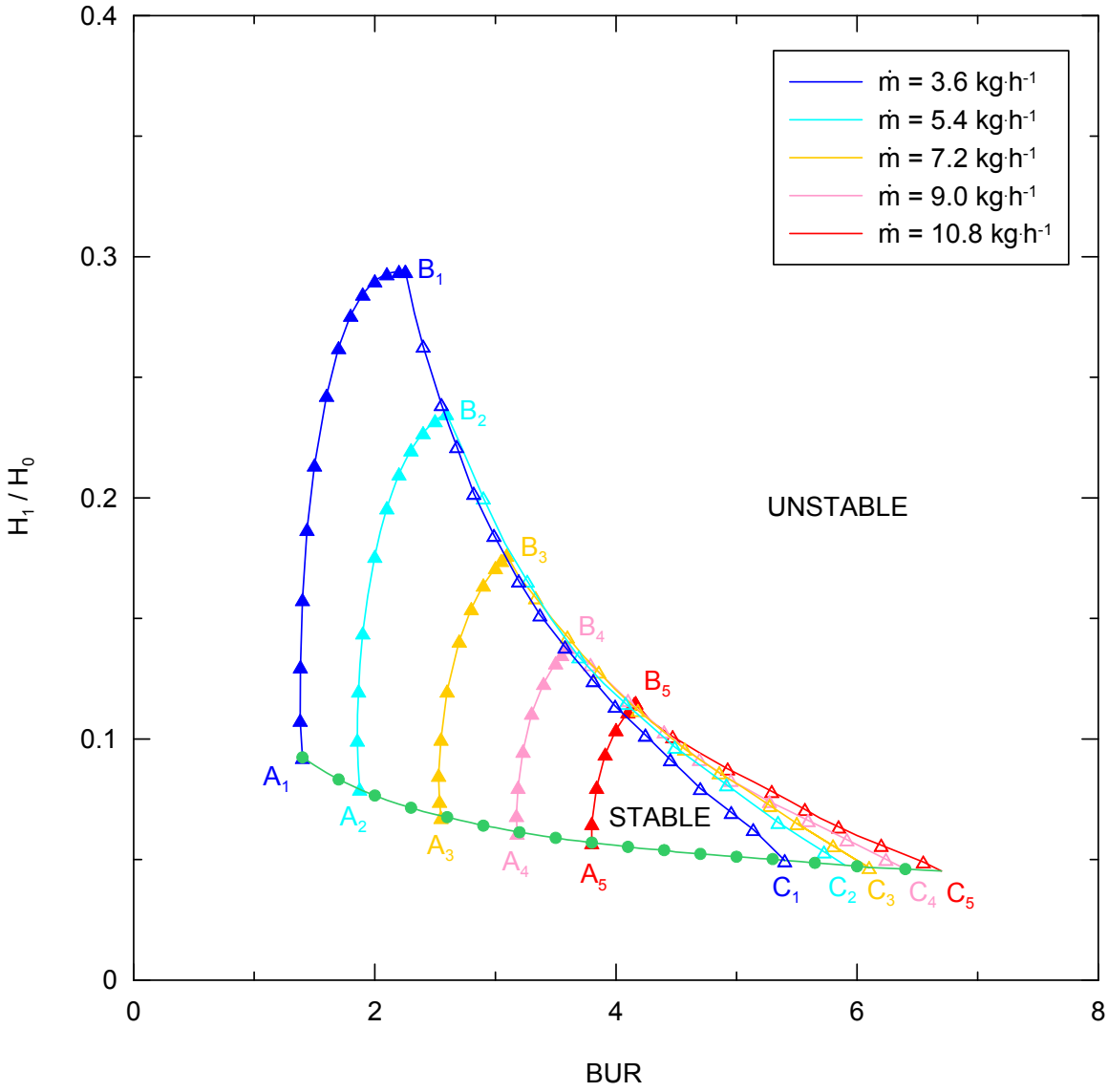

Fig. 46. Stability contours for different level of the mass flow rate predicted by the Zatloukal-Vlcek model for non-isothermal processing conditions and non-Newtonian polymer melt. Model and machine stability contours are represented by triangles and circles, respectively.

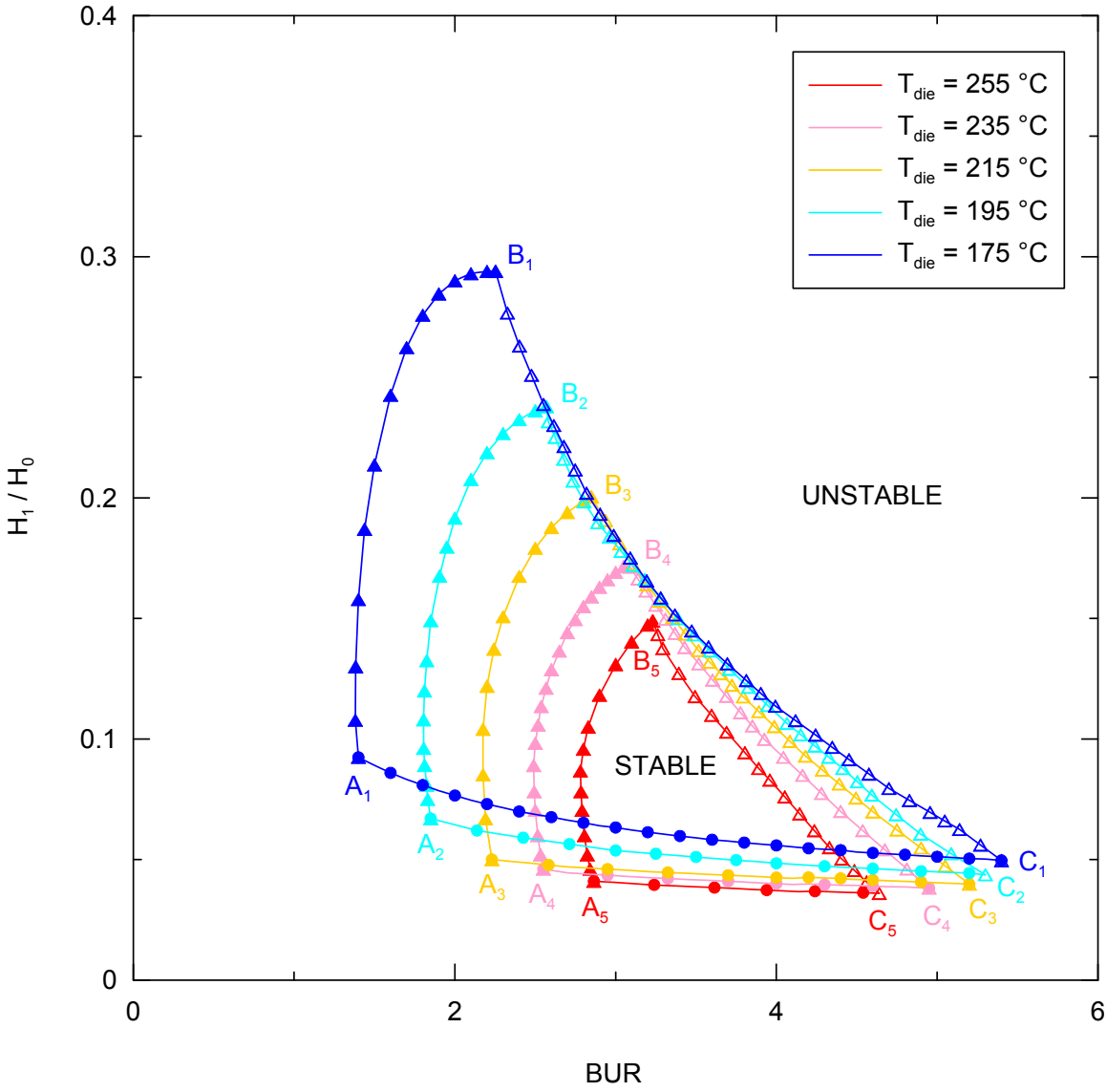

Fig. 47. Stability contours for different level of the melt/die temperature predicted by the Zatloukal-Vlcek model for non-isothermal processing conditions and non-Newtonian polymer melt. Model and machine stability contours are represented by triangles and circles, respectively.

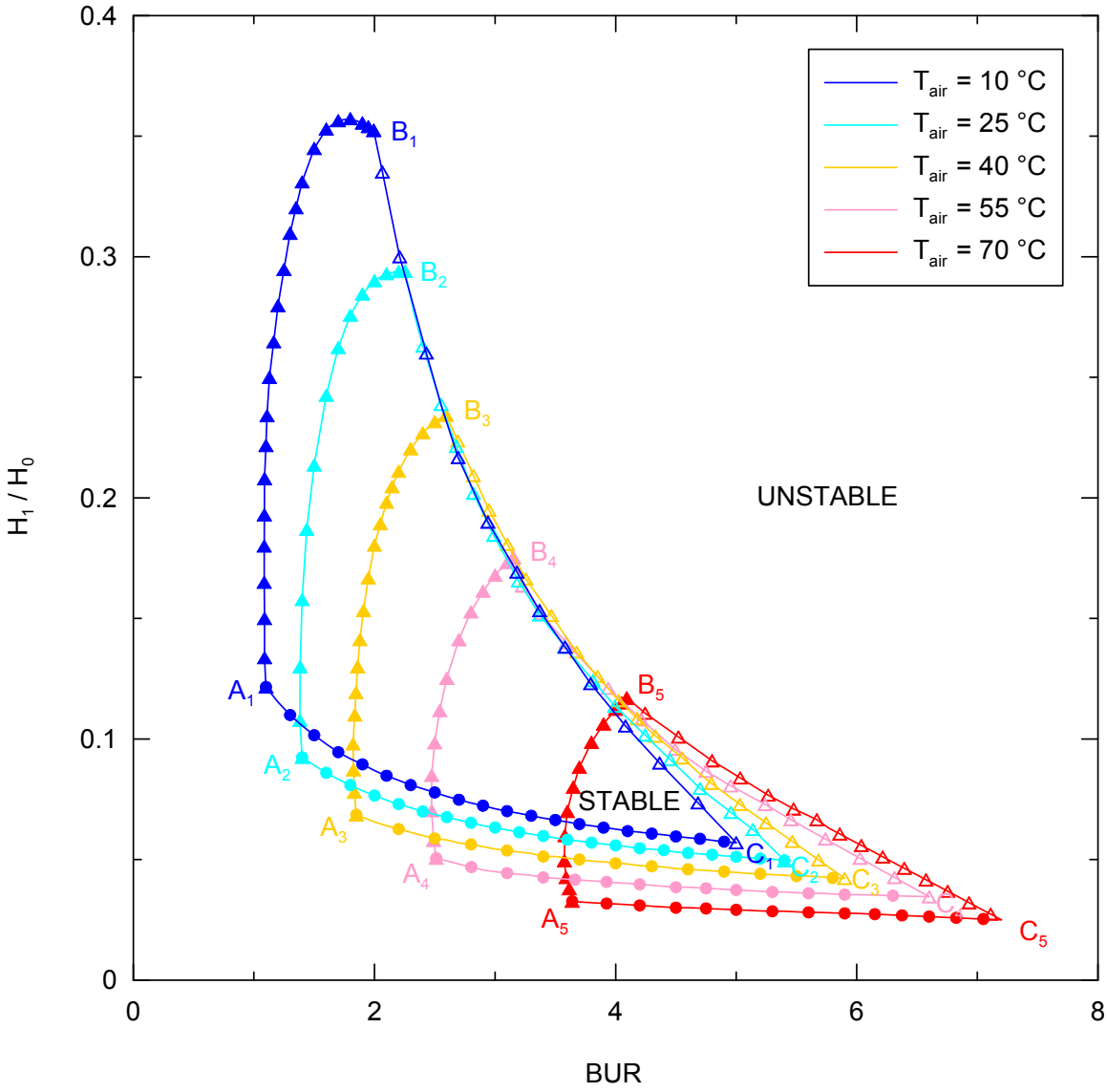

Fig. 48. Stability contours for different level of the cooling air temperature predicted by the Zatloukal-Vlcek model for non-isothermal processing conditions and non-Newtonian polymer melt. Model and machine stability contours are represented by triangles and circles, respectively.

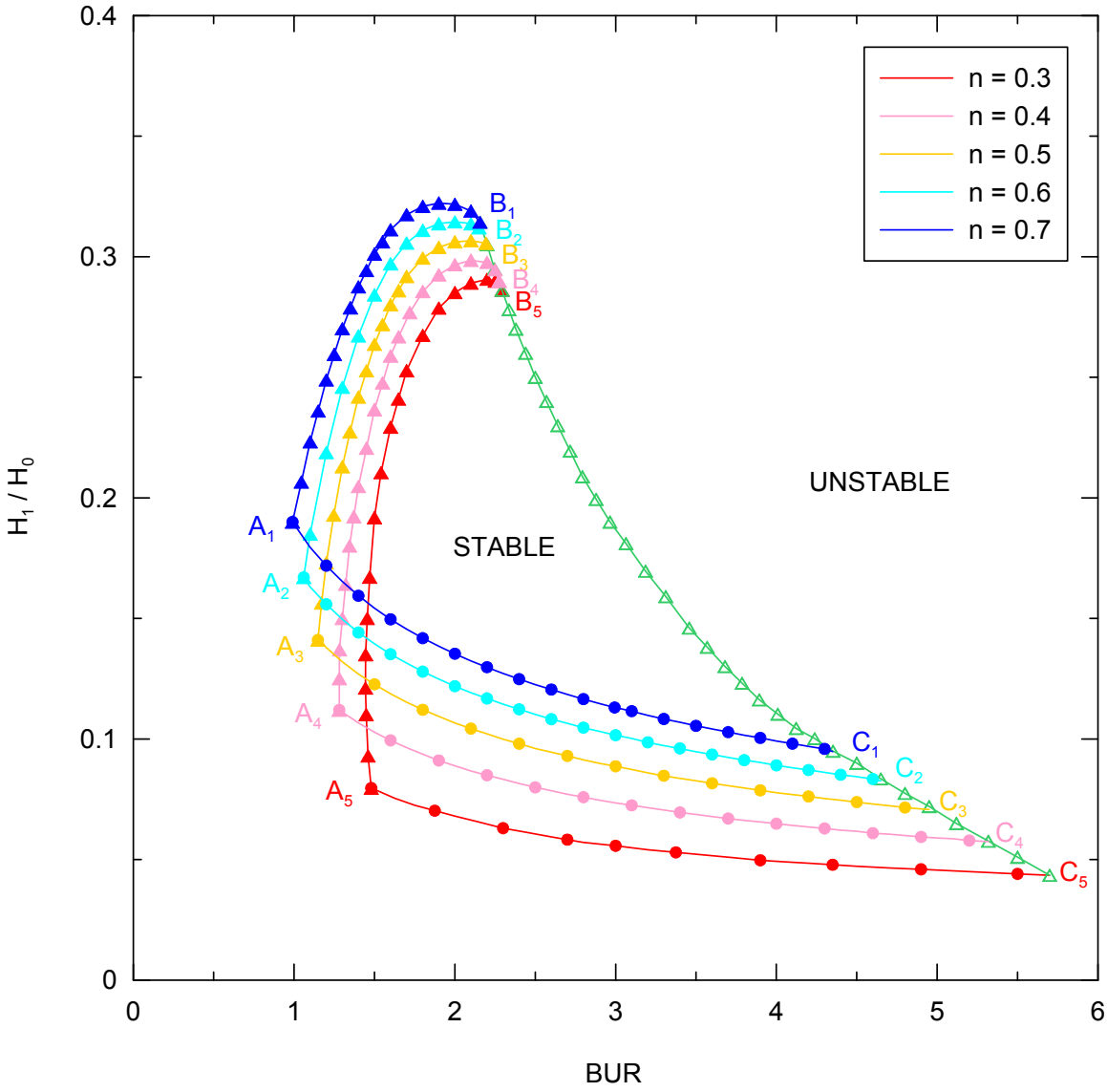

Fig. 49. Stability contours for different level of the power law index (index of non-Newtonian behavior) predicted by the Zatloukal-Vlcek model for non-isothermal processing conditions and non-Newtonian polymer melt. Model and machine stability contours are represented by triangles and circles, respectively.

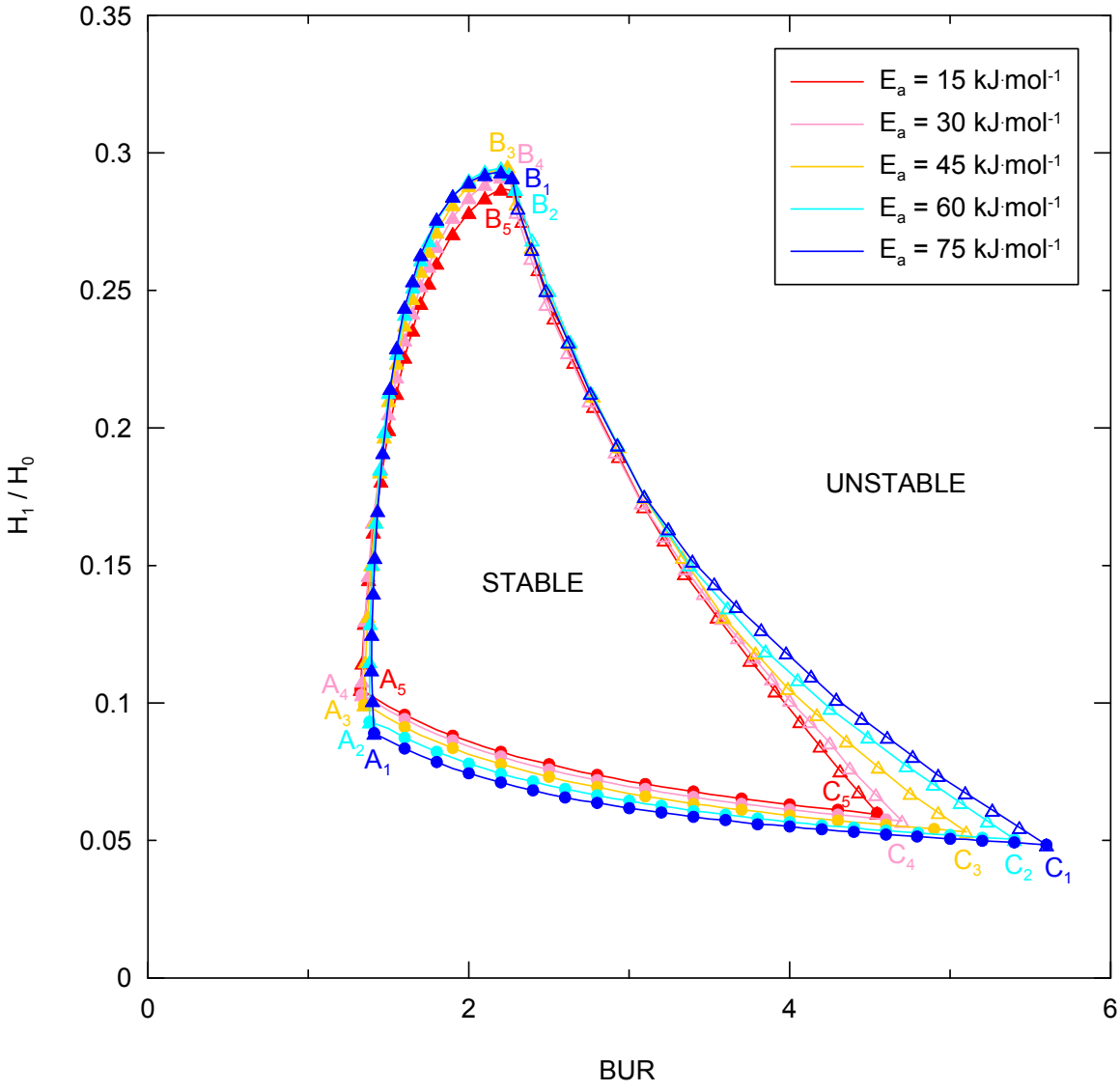

Fig. 50. Stability contours for different level of the flow activation energy predicted by the Zatloukal-Vlcek model for non-isothermal processing conditions and non-Newtonian polymer melt. Model and machine stability contours are represented by triangles and circles, respectively.

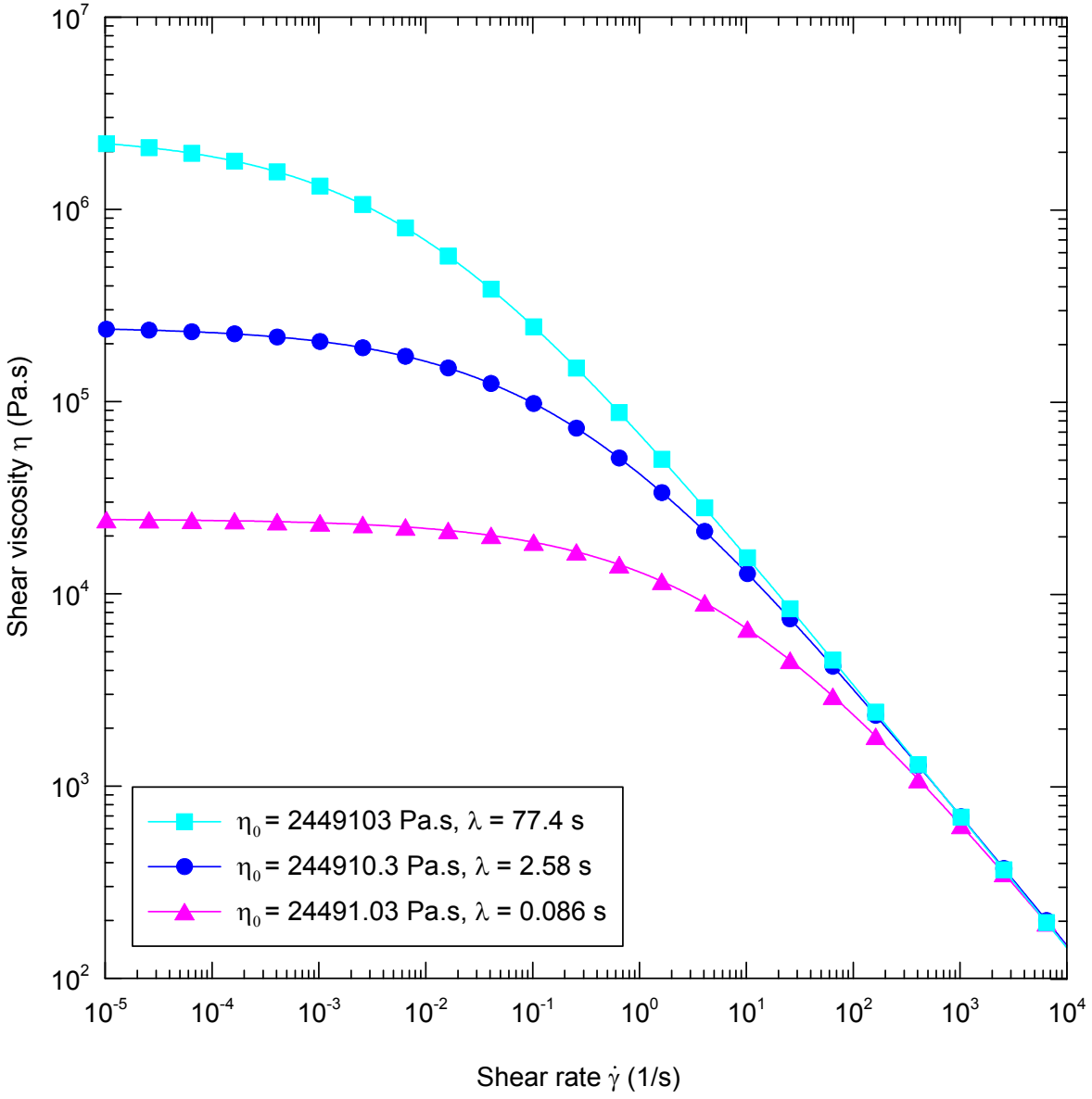

Fig. 51. Shear viscosity prediction of the generalized Newtonian model for different values of η_0 and λ (effect of Mw).

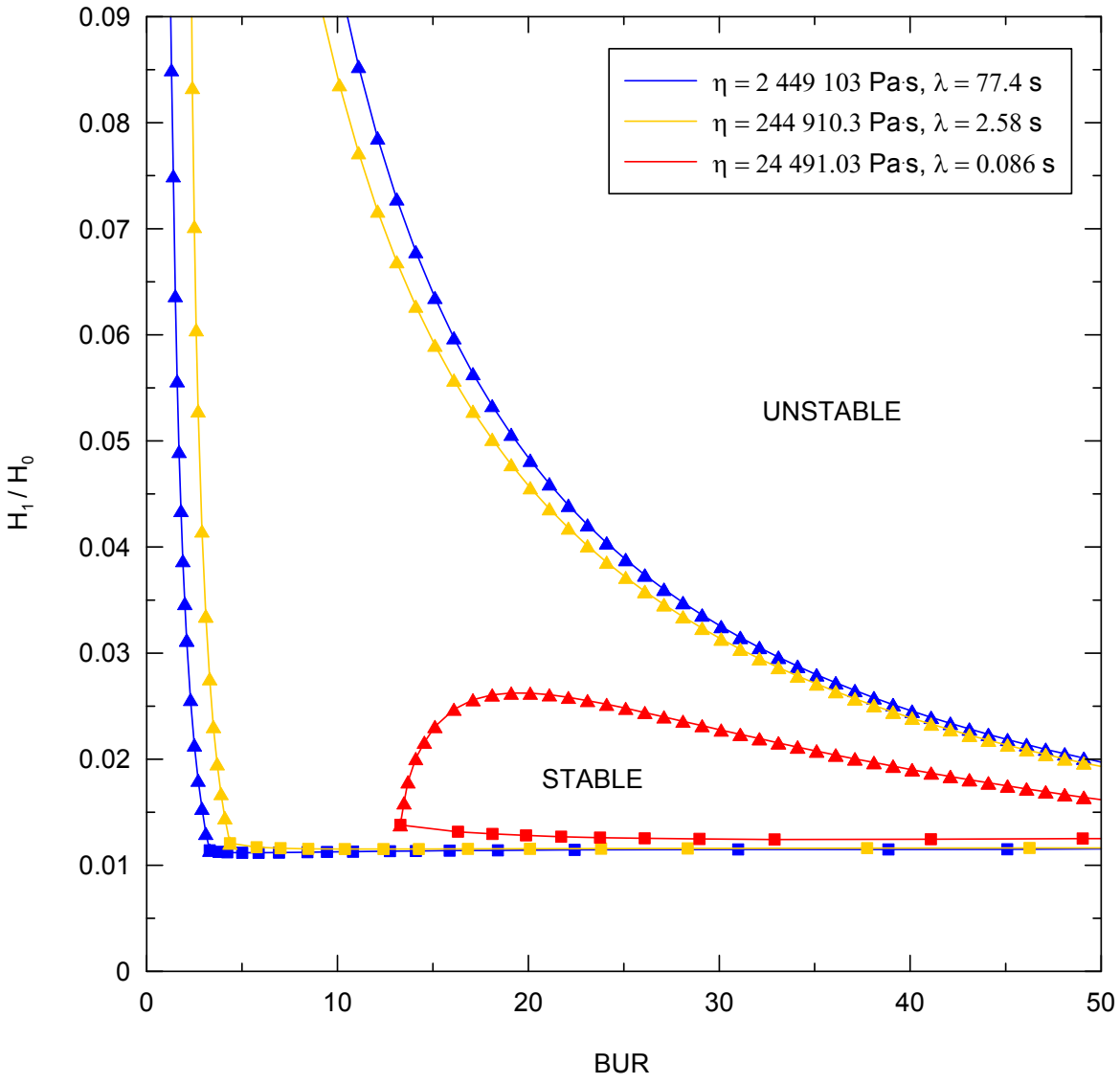

Fig. 52. Predicted film blowing stability contours for three virtual materials (Fig. 51) by using Zatloukal-Vlcek film blowing model (effect of Mw). Processing conditions are provided in Tab. 20.

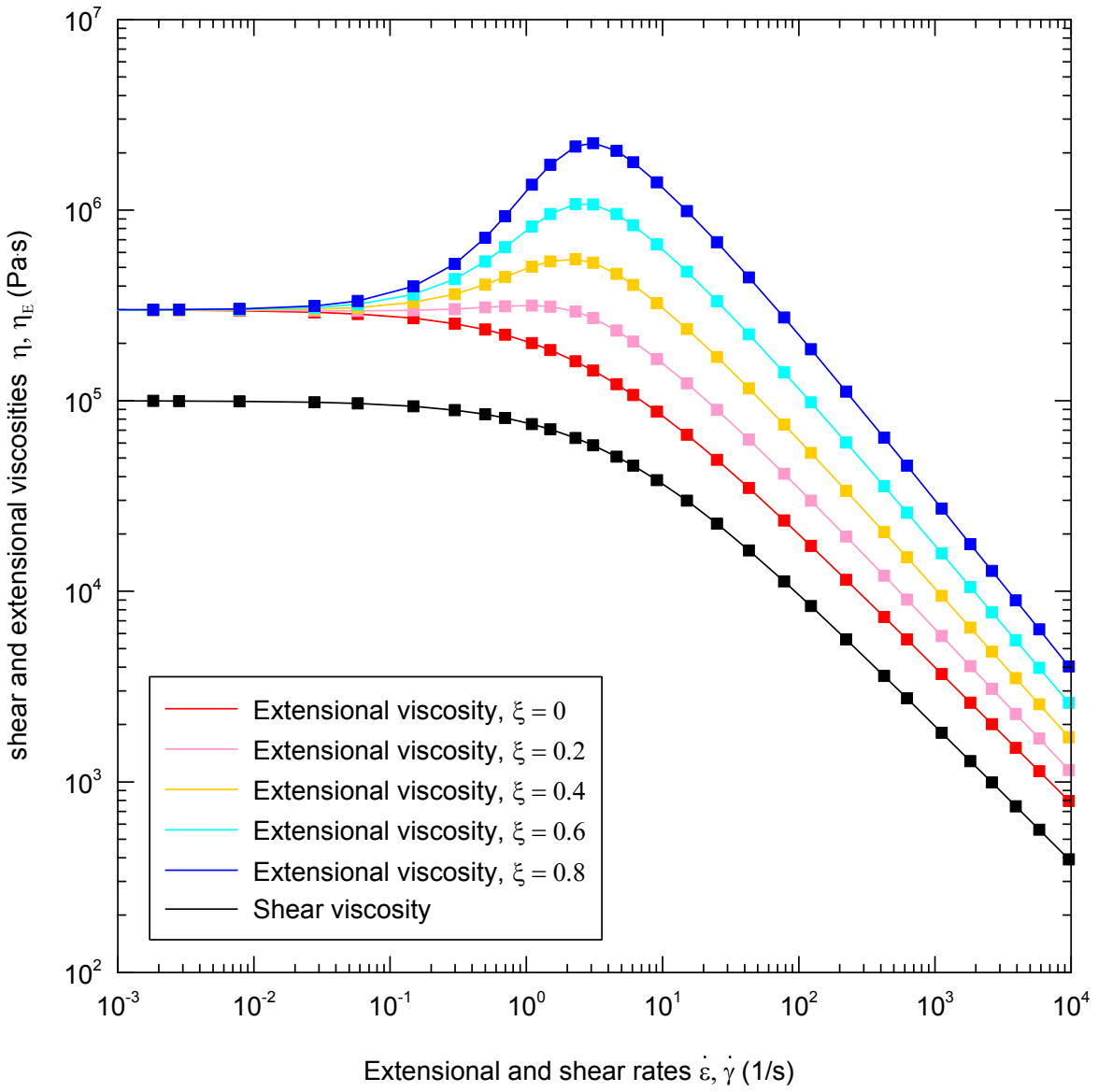

Fig. 53. Shear and extensional viscosity prediction of the generalized Newtonian model for different values of ξ (different level long chain branching).

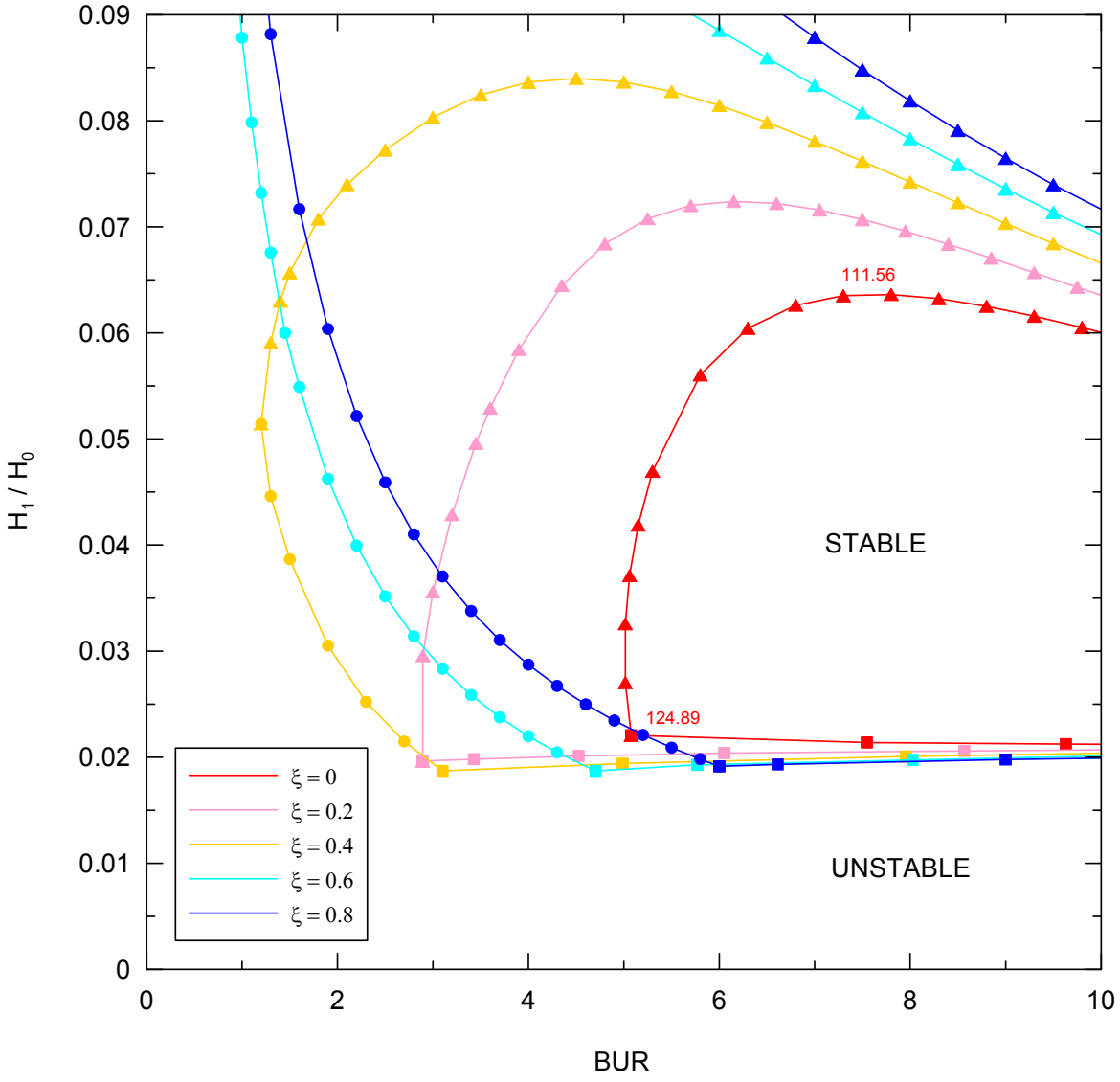

Fig. 54. Predicted film blowing stability contours for five virtual materials (Fig. 53) by using Zatloukal-Vlcek film blowing model (effect of long chain branching). Processing conditions are provided in Tab. 20.

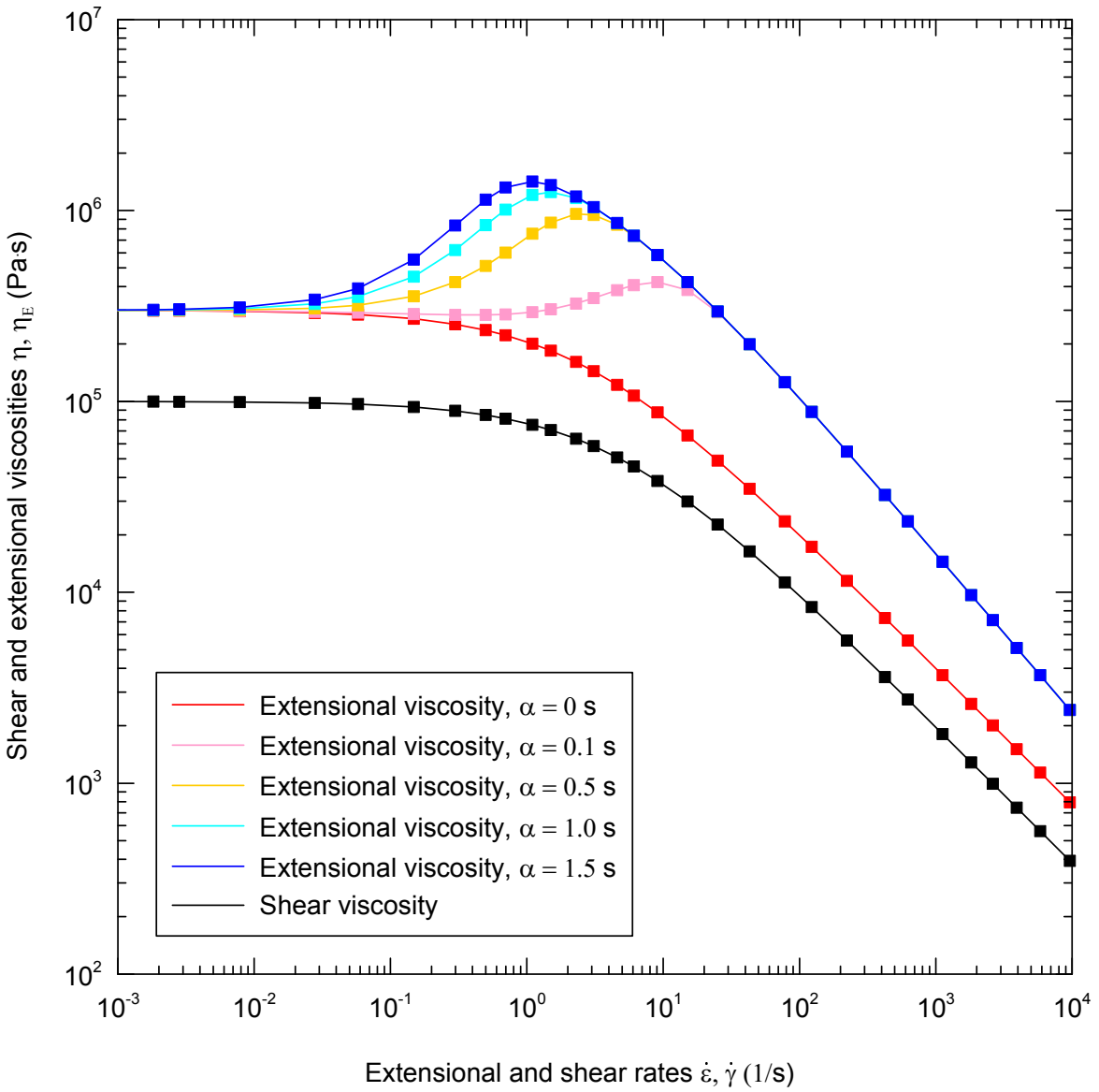

Fig. 55. Shear and extensional viscosity prediction of the generalized Newtonian model for different values of α (different level long chain branching).

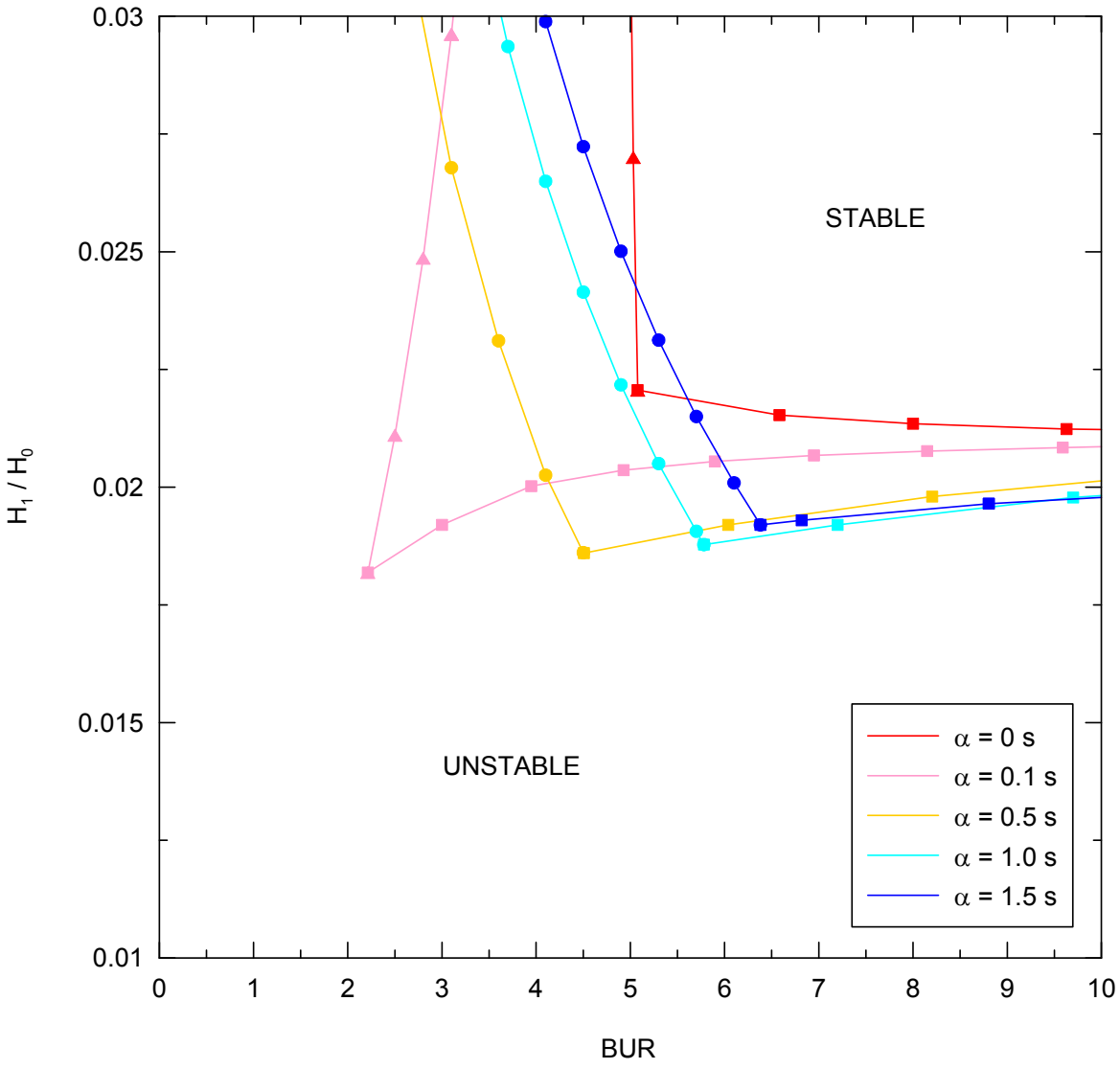

Fig. 56. Predicted film blowing stability contours for five virtual materials (Fig. 55) by using Zatloukal-Vlcek film blowing model (effect of long chain branching). Processing conditions are provided in Tab. 20.

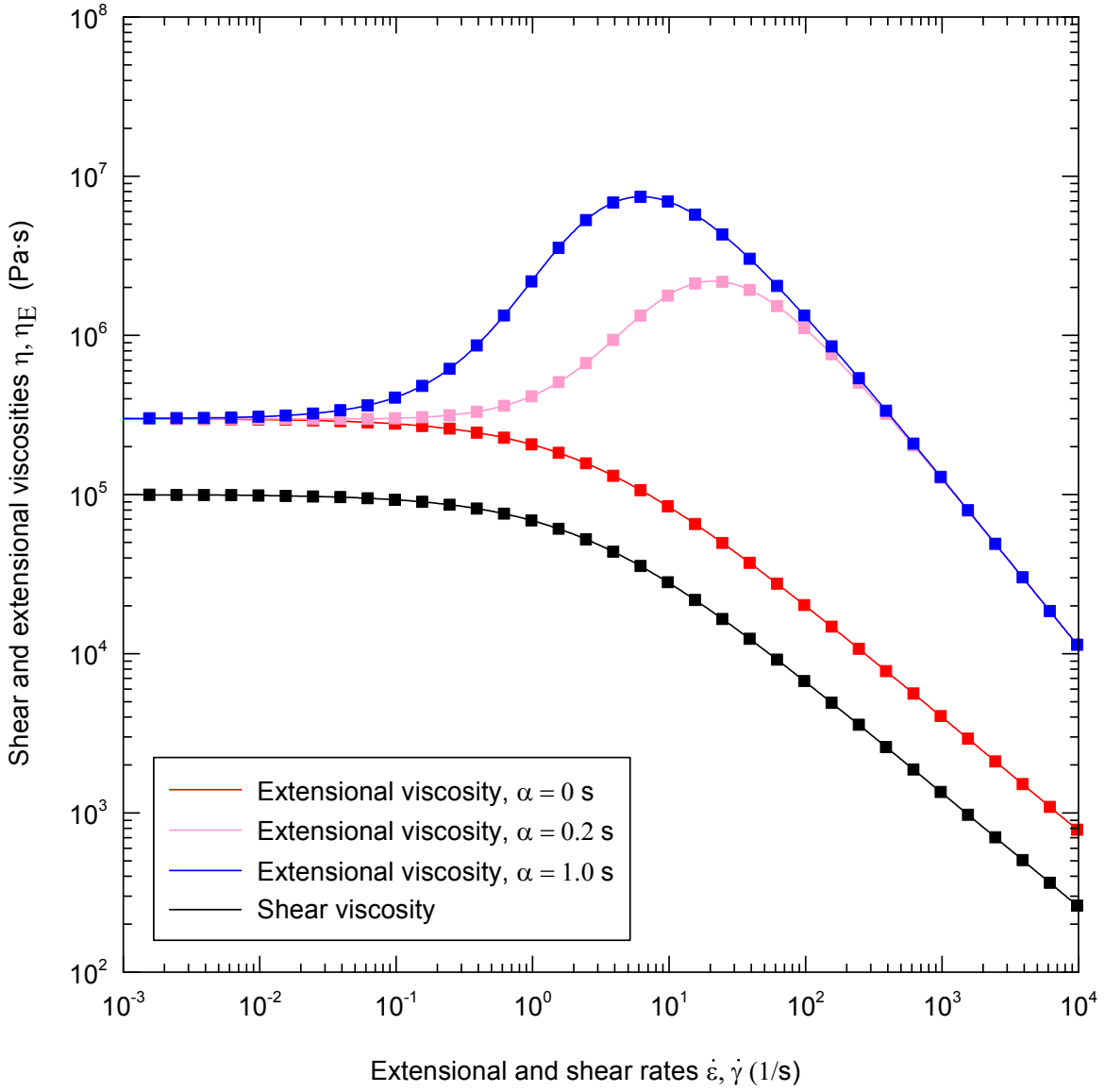

Fig. 57. Shear and extensional viscosity prediction of the generalized Newtonian model for different (linear and branched) mLLDPE polymers (different level long chain branching is introduced by varying of α parameter).

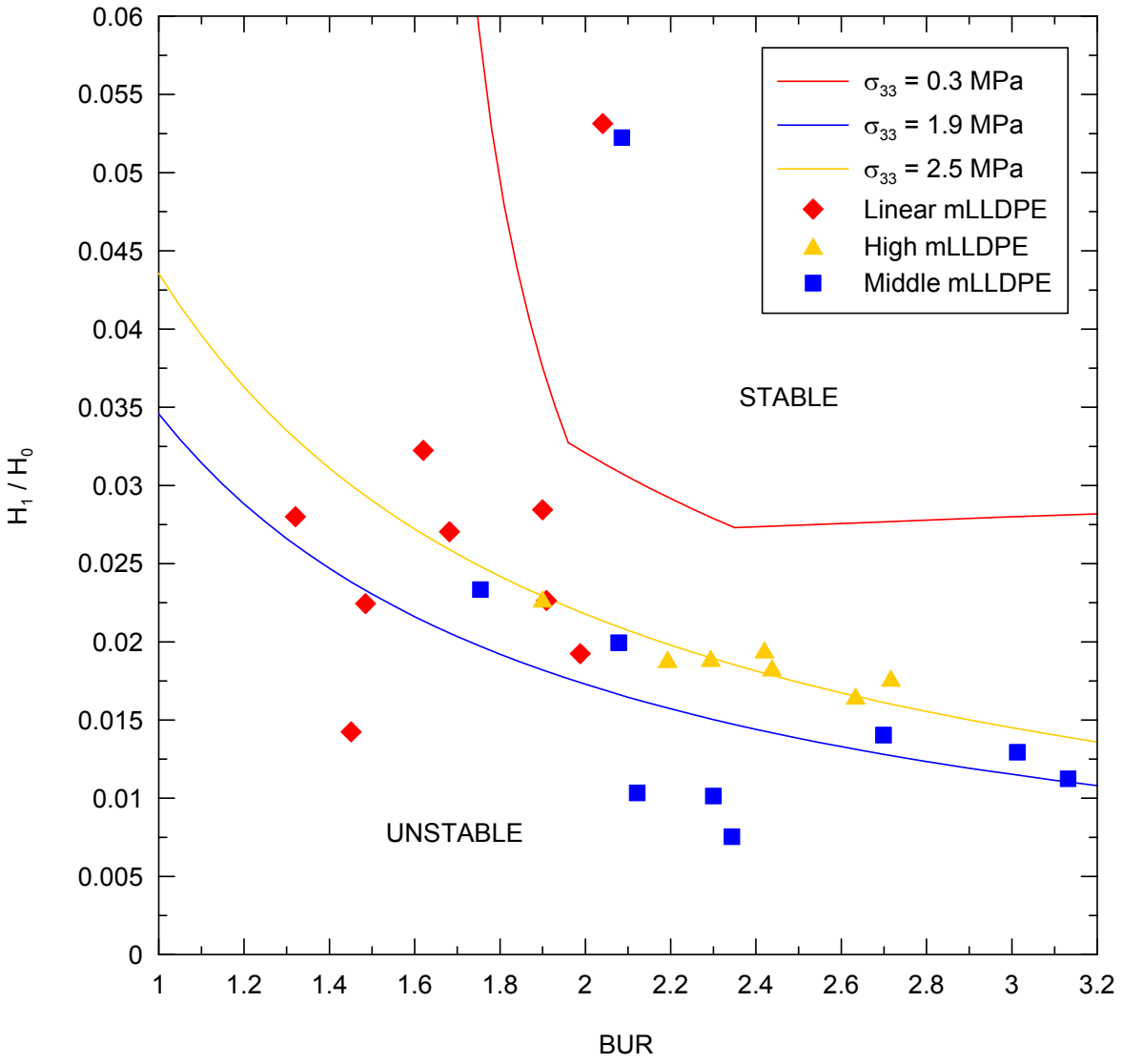

Fig. 58. Comparison between experimental data taken from [54] and predicted film blowing stability contours (lines) for linear and branched mLLDPE polymers (Fig. 57) by using Zatloukal-Vlcek film blowing model. Model parameters are provided in Tabs. 20-21.

BIBLIOGRAPHY

[1] TAS, P.P. *Film blowing from polymer to product.* Ph.D. Thesis, Technische Universitat Eindhoven, 1994.

[2] KOLARIK, R. *Modeling of the film blowing process by using variational principles*. Bc. Thesis, Tomas Bata University in Zlín, Czech Republic, 2006.

[3] CANTOR, K. *Blown Film Extrusion*. Munich : Cark Hanser Verlag, 2006. 165 s. ISBN 1-56990-396-4.

[4] LUO, X. L., TANNER, R. I. *A computer study of film blowing*. Polym. Eng. Sci. 25, p. 620, 1985.

[5] ASHOK, B. K., CAMPBELL, G. A. *Two-phase simulation of tubular film blowing of crystalline polymers*. Int. Polym. Process. 7, 240, 1992.

[6] ZATLOUKAL, M., VLCEK, J. *Application of variational principles in modeling of the film blowing process for high stalk bubbles*. J. Non-Newtonian Fluid Mech. 133, p. 63-72, 2006.

[7] ZATLOUKAL, M., VLCEK, J. *Modeling of the film blowing process by using variational principles.* J. Non-Newtonian Fluid Mech. 123, p. 201-213, 2004.

[8] ZATLOUKAL, M., MAVRIDIS, H., VLCEK, J., SAHA, P. *Modeling of Non-isothermal Film Blowing Process by Using Variational Principles*. SPE ANTEC, p. 825-829, Charlotte, USA, 2006.

[9] ZATLOUKAL, M., SAHA, P. *Modeling of the film blowing process by using variational principles for high stalk bubbles*. PPS-21, Leipzig, Germany, 2005 (CD-ROM).

[10] KANAI, T., CAMPBELL, G. A. *Film Processing: Progress in Polymer Processing*. Hanser Gardner Publications, Munich, Germany, 1999.

[11] MAYAVARAM, R. S. *Modeling and simulation of film blowing process.* Ph.D. Thesis, A&M University Texas, 2005.

[12] HAN, Ch. D. *Rheology in Polymer Processing*. New York : Academic Press, 1976. 366 s. ISBN 0-12-322450-0.

[13] BUTLER, T. I. *Film extrusion Manual : Process, materials, properties*. Atlanta : Tappi press, 2005. 616 s. ISBN 1-59510-075-X.

[14] HAN, Ch. D. *Rheology and Processing of Polymeric Materials : Volume 2 Polymer Processing*. New York : Oxford University Press, 2007. 579 s. ISBN 978-0-19-518783-0.

[15] BAIRD, D. G., COLLIAS, D. I. *Polymer Processing : Principles and Design*. Canada : John Wiley & Sons, 1998. 346 s. ISBN 0-471-25453-3.

[16] PEARSON, J. R., PETRIE, C. J. S. *The flow of a tubular film. Part 2. Interpretation of the model and discussion of solutions*. J. Fluid Mech. 42, p. 60, 1970.

[17] AGASSANT, J. F., AVENAS, P., SERGENT, J. Ph., CARREAU, P. J. *Polymer processing: Principles and modeling*, Carl Hanser, Munich, Gremany, 1991.

[18] BUTLER, T. I. *Blown film bubble instability induced by fabrication conditions*. SPE ANTEC Tech. Papers 1, p. 1120, 2000.

[19] HAN, C. D., PARK, J. Y. *Studies on blown film extrusion: Part 3. Bubble instability*. J. Appl. Polymer Sci. 19, p. 3291, 1975.

[20] HAN, C. D., SHETTY, R. *Flow instability in tubular film blowing: Part 1. Experimental study*. Ind. Eng. Chem. Fund., 16, p. 49, 1977.

[21] OBIJESKI, T. J., PURITT, K. R. *Improving the output and bubble stability of thick gauge blown film*. SPE ANTEC Tech. Papers 1, p. 150, 1992.

[22] KANAI, T., WHITE, J. L. *Kinematics, dynamics and stability of the tubular film extrusion of various polyethylenes*. J. Non-Newtonian Fluid Mech. 19, p. 275, 1986.

[23] SWEENEY, P. A., CAMPBELL, G. A. *Blown film stability*. ANTEC 461, p. 461, 1993.

[24] LAFUENTE-CANAS, P., FERNÁNDEZ AMO, B., SMITH, G. D., SPARES, R., MARTYN, M. T., COATES, P. D. *Blown Film: processing stability for metallocenes*. in: Polymer Process Engineering 03: Enhanced Polymer Processing, p. 192-213. Edited by PD Coates, University Press, Bradford, UK, 2003.

[25] WALLER, P. *What to do when the bubble won´t behave*. Plastic Technology, (December 2002), p.36

[26] ZATLOUKAL, M. *Differential viscoelastic constitutive equations for polymer melts in steady shear and elongational flows*. J. Non-Newtonian Fluid Mech. 113, 209, 2003.

[27] KIM, S., FANG, Y., LAFLEUR, P. G., CARREAU, P. J. *Dynamics and criteria for bubble instabilities in a single layer film blowing extrusion.* Polymer Engineering and Science, 4, 2, 2004.

[28] DEBBAUT, B. et. al. Intern. Polym. Process., 13, 3, p. 262, 1999.

[29] WANG, S.Q. Advances in Polymer Science, 138, p. 229, 1999.

[30] SIDIROPOULOS, V., VLACHOPOULOS, J. *Numerical study of internal bubble cooling (IBC) in film blowing.* Polymer Processing, 16, 1, 2001.

[31] SIDIROPOULOS, V., VLACHOPOULOS, J. *An investigation of Venturi and Coanda effects in blown film cooling.* Polymer Processing, 15, 1, 2000.

[32] ZHANG, Z., LAFLEUR, P. G., BERTRAND, F. *Effect of aerodynamics on film blowing process.* Polymer Processing, 21, 5, 2006.

[33] SIDIROPOULOS, V., VLACHOPOULOS, J. *The aerodynamics of blown film bubble cooling.* Journal of Reinforced Plastics and Composites, 18, 6, p. 529-538, 1999.

[34] MUKE, S., CONNELL, H., SBARSKI, I., BHATTACHARYA, S. N. *Numerical modeling and experimental verification of blown film processing*. J. Non-Newtonian Fluid Mech. 116, p. 113-138, 2003.

[35] PEARSON, J. R. A., PETRIE, C. J. S. *The flow of a tubular film. Part 1. Formal mathematical representation*. J. Fluid Mech. 40, p. 1, 1970.

[36] PETRIE, C. J. S. *A comparison of theoretical predictions with published experimental measurements on the blown film process*. Am. Inst. Chem. Eng. J. 21, p. 275, 1975.

[37] HAN, C. D., PARK, J. Y. *Studies on blown film extrusion. 2. Analysis of the deformation and heat transfer process*. J. Appl. Polym. Sci. 19, p. 3277-3290, 1975.

[38] WAGNER, M. H. *Das folienblasverfahren als rheologish-thermodynamischer PozeB*. Rheol. Acta 15, p. 40-51, 1976.

[39] PEARSON, J. R., GUTTERIDGE, P. A. *Stretching flow for thin film production. Part 1. Bubble blowing in the solid phase*. J. Non-Newtonian Fluid Mech. 4, p. 57-72, 1978.

[40] GUPTA, R. K., METZNER, A. B., WISSBRUN, K. F. *Modeling of polymeric film-blowing processes*. Polym. Eng. Sci. 22, 172, 1982.

[41] KANAI, T., WHITE, J. L. *Dynamics, heat transfer and structure development in tubular film extrusion of polymer melts: a mathematical model and predictions*. J. Polym. Eng. 5, p. 135, 1985.

[42] CAIN, J. J., DENN, M. M. *Multiplicities and instabilities in film blowing*. Polym. Eng. Sci. 28, p. 1527, 1988.

[43] SEO, Y., WISSLER, E. H. *The effect of extrude swell on modeling the film blowing process*. Polym. Eng. Sci. 29, 722, 1989.

[44] CAMPBELL, G. A., CAO, B. *Blown film simulation, A severe test for rheological models*. in: Collyer, A.A.a.U.L.A. (Ed.), Polymer Rheology and Processing, Elsevier, Amsterdam, 1990.

[45] CAO, B., CAMPBELL, G. A. *Viscoplastic-elastic modeling of tubular blown film processing*. Am. Inst. Chem. Eng. J. 36, p. 420, 1990.

[46] ALAIE, S. M., PAPANASTASIOU, T. C. *Modeling of non-isothermal film blowing with integral constitutive equations*. Int. Polym. Process. 8, p. 51-65, 1993.

[47] LIU, C. C., BOQUE, D. C., SPRUIELL J. E. *Tubular film blowing. Part 2. Theoretical modeling*. Int. Polym. Process. 10, p. 230, 1995.

[48] SIDIROPOULOS, V., VLACHOPOULOS, J. *Computer simulation of film blowing*. in: Proceeding of the ANTEC, p. 31-39, 1996.

[49] SIDIROPOULOS, V., TIAN, J. J., VLACHOPOULOS, J. *Computer simulation of film blowing*. TAPPI J. 79, p. 113-118, 1996.

[50] KUIJK, E. W., TAS, P. P., NEUTEBOOM, P. *A rheological model for the prediction of polyethylene blown film properties*. SPE ANTEC 98, 3001, 1998.

[51] SPENCER, R. S., GILMORE, R. D. J. Appl. Phys., p. 21-523, 1950.

[52] HELLWEGE, K. H., KNAPPE, W., LEHMANN, P., KOLLOID, Z. *Polymere*. 183, p. 110-120, 1962.

[53] Xpansion Intruments, *www.xinst.com* [online]. c2005 [cit. 2008-05-22]. Available at WWW: <http://www.xinst.com/products_modes.htm>.

[54] ZATLOUKAL, M., KOLARIK, R., MUSIL, J., MARTYN, M., COATES, P. *Investigation of film blowing process stability for metallocene based LLDPE with different level of long chain branching*. SPE ANTEC, p. 1573-1578, 2007.

[55] DOUFAS, A. K., McHUGH, A. J. *Simulation of film blowing including flow-induced crystallization.* J. Rheology. 45 (5), 1085, 2001.

[56] ZATLOUKAL, M., MAVRIDIS, H., VLCEK, J., SAHA, P. *Modeling of Non-Isothermal high stalk film blowing process by using variational principles for Non-Newtonian fluids*. SPE ANTEC, p. 1579-1583, 2007.

[57] MUSIL, J. *The effect of long chain branching on processibility of polymer melts.* Bc. Thesis, Tomas Bata University in Zlín, Czech Republic, 2006.

[58] MUNSTEDT, H., STEFFL, T., MALMBERG, A. *Correlation between rheological behaviour in uniaxial elongation and film blowing properties of various polyethylenes.* Rheol Acta 45, 14, 2005.

LIST OF SYMBOLS

BUR	Blow-up ratio	1
D_f	Bubble diameter at the freeze line height	m
D_d	Bubble diameter at the die exit	m
π	Ludolf´s number	1
TUR	Take-up ratio	1
v_f	Film velocity at the freeze line height	$m \cdot s^{-1}$
v_d	Film velocity at the die exit	$m \cdot s^{-1}$
ρ_m	Polymer melt density	$kg \cdot m^{-3}$
ρ_s	Solid polymer density	$kg \cdot m^{-3}$
A_f	Bubble cross-sectional area	m^2
A_d	Die gap area	m^2
DDR	Draw down ratio	1
t_d	Die gap thickness	m
t_f	Final film thickness	m
FR	Forming ratio	1
F	Take-off force	N
L	Freeze line height	m
$\dot{m}$	Mass flow rate	$kg \cdot s^{-1}$
r	Bubble radius	m
h	Film thickness	m
H_1	Bubble thickness at the freeze line height	m
R_1	Bubble radius at the freeze line height	m
R_0	Bubble radius at the die exit	m
H_0	Die gap	m

x_1	Tangential direction	m
x_2	Thickness direction	m
x_3	Circumferential direction	m
v	Film velocity	$m \cdot s^{-1}$
ρ	Film density	$kg \cdot m^{-3}$
R_g	Universal gas constant	$J \cdot K^{-1} mol^{-1}$
T	Bubble temperature	K
P^*	Cohesion pressure	Pa
w	Molecular weight	$kg \cdot mol^{-1}$
b'	Specific volume	$m^3 \cdot kg^{-1}$
Δp	Internal bubble pressure	Pa
σ_{11}	Tangential component of the total stress tensor	Pa
R_m	Curvature radius	m
σ_{33}	Circumferential component of the total stress tensor	Pa
R_t	Curvature radius	m
Θ	Bubble angle	°
G	Gravity	N
H	Force created by the air flow	N
r_f	Bubble radius at the freeze line height	m
dx	Element length in x direction	m
dr	Element length in r direction	m
σ	Total stress tensor	Pa
p	Internal load	Pa·m
I	Unit tensor	1
τ	Extra stress	Pa
σ_{22}	Thickness directions of the stress	Pa

τ_{11}	Extra stress in the tangential directions	Pa
τ_{22}	Extra stress in the thickness directions	Pa
τ_{33}	Extra stress in the circumferential directions	Pa
J	Membrane compliance	Pa^{-1}
y	Equation for the bubble shape (radius) without the neck	m
λ_1	Lagrange multiplier	Pa
pJ	Film blowing model parameter	m
φ	Zatloukal-Vlcek model function	1
A	Zatloukal-Vlcek model function	1
α'	Zatloukal-Vlcek model function	1
φ''	Zatloukal-Vlcek model function	1
A''	Zatloukal-Vlcek model function	1
α''	Zatloukal-Vlcek model function	1
BUR_0	Blow-up ratio at the neck	1
y_1, y_2	Equations for the bubble shape (radius) having the neck height	m
L_1	Neck height	m
ξ	Zatloukal-Vlcek model function	m^2
F_I	Tensile force acting at the die exit (Zatloukal-Vlcek model)	N
F_{II}	Tensile force at the freeze line height (Zatloukal-Vlcek model)	N
pL	Force acting in the thickness direction	N
Q	Volumetric flow rate	$m^3 \cdot s^{-1}$
η_0	Newtonian viscosity	Pa·s
D	Deformation rate tensor	s^{-1}
$F_{II,N}$	Force acting at the freeze line height (Newton model)	N
A'	Zatloukal-Vlcek model function	1
$p'J'$	Film blowing model parameter	m

J_1	Membrane compliance in Region I	Pa^{-1}
J_2	Membrane compliance in Region II	Pa^{-1}
E_2	Young´s modulus of the membrane	Pa
C_p	Specific heat capacity	$J \cdot kg^{-1} \cdot K^{-1}$
h	Heat transfer coefficient	$W \cdot m^{-1} \cdot K^{-1}$
T_{air}	Air temperature	°C
σ_B	Stefan-Boltzmann constant	$W \cdot m^{-2} \cdot K^{-4}$
ΔH_f	Heat of crystallization per unit mass	cal/g
ϕ	Average absolute degree of crystallinity	1
ε	Emissivity	1
T_{die}	Temperature of the melt at the die exit	°C
T_{air}	Solidification temperature of the polymer	°C
T_{solid}	Freezeline temperature	°C
T_r	Reference temperature	°C
a_t	Arrhenius equation for temperature – dependent shift factor	1
II_D	Second invariant of deformation rate tensor	s^{-1}
III_D	Third invariants of deformation rate tensor	s^{-1}
n	Power-law index	1
a	Adjustable parameter in Carreau-Yasuda function	1
λ	Relaxation time	s
ξ	Adjustable parameter in Generalized Newtonian model	1
α	Extensional strain-hardening parameter in Generalized Newtonian model	s
β	Adjustable parameter	1
E_a	Activation energy	J
η	Shear viscosity	$Pa \cdot s$

η_E	Extensional viscosity	Pa·s
$\bar{\eta}$	Bubble viscosity	Pa·s
$\dot{\varepsilon}$	Extensional rate	s^{-1}
$\bar{v}$	velocity mean value along the bubble	$m \cdot s^{-1}$
$\bar{h}$	thickness mean value along the bubble	m

LIST OF FIGURES

LIST OF TABLES

LIST OF APPENDICES

APPENDIX P I: FILM BLOWING PROCESS